UC Santa Barbara

UC Santa Barbara Electronic Theses and Dissertations

Title

Diamond optomechanical crystals for hybrid mechanical systems

Permalink

https://escholarship.org/uc/item/8450n7kh

Author

Cady, Jeffrey

Publication Date

2021

Peer reviewed|Thesis/dissertation

eScholarship.org Powered by the California Digital Library
University of California

University of California
Santa Barbara

Diamond optomechanical crystals for hybrid mechanical systems

A dissertation submitted in partial satisfaction
of the requirements for the degree

Doctor of Philosophy
in
Physics

by

Jeffrey Vernon Cady

Committee in charge:

Professor Ania Bleszynski Jayich, Chair
Professor David Weld
Professor Mark Srednicki

December 2021

The Dissertation of Jeffrey Vernon Cady is approved.

Professor David Weld

Professor Mark Srednicki

Professor Ania Bleszynski Jayich, Committee Chair

September 2021

Diamond optomechanical crystals for hybrid mechanical systems

Copyright © 2021

by

Jeffrey Vernon Cady

For Suzannah, Pia Maria, and Thomas Damien

Acknowledgements

I would first like to thank Ania for letting me join her lab, for advising me, and for letting me take the spin-phonon project in a bit of a wild direction (a hopefully useful years-long detour into optomechanics) and for being so understanding and flexible during a rather unorthodox six years of graduate school: mudslides, a pandemic, and a premature baby were hurdles I didn't expect going in. She helped me to think big and be thorough and I am a better scientist because of the lessons she taught me. I would also like to thank the spin-phonon members who welcomed me into the lab. Preeti for helping me to transfer my cleanroom skills into diamond and for teaching me not to take graduate school *too* seriously. Donghun was a paragon of professionalism and kindness. He took all of my (probably silly) questions seriously and made lab a comfortable space. Kenny taught me almost everything I know about optics and NV centers and strain. Even after graduating he was always available on gchat to answer questions, to discuss new papers that we noticed on the arXiv, or to talk about basketball. I am so glad that the spin-phonon project will live on in the hands of Carl, Hyunseok, and Viraj. They are poised to do some really interesting science and I wish them all the best. I would also like to thank Claire for her kindness and for teaching me innumerable practical things about lab, answering any and every question I threw at her. Thank you also to her and every other student who ever helped me with a clean/anneal/growth etc. (Daipeng, Zhiran, Lillian, Simon). I would also like to acknowledge Dirk Bouwmeester and his students Fernando and Ian for helping me to push the boundaries of new diamond fabrication techniques. Importantly, I need to thank Professor Amir Safavi-Naeini and his students Rishi Patel and Chris Sarabilis for their helping getting our optomechanics experiment up and running and for allowing me to take initial measurements in their lab. This project would be years behind without them. Thanks to my parents for always supporting and

encouraging my interest in physics and my intellectual curiosity in general. Lastly, I thank my wife, Suzannah, and children, Pia and Damien, for supporting me through graduate school and for the countless sacrifices they have made for me. They were and are my inspiration and joy.

Curriculum Vitæ

Jeffrey Vernon Cady

Education

2021	Ph.D. in Physics, University of California, Santa Barbara.
2018	M.A. in Physics, University of California, Santa Barbara.
2015	A.B. in Physics, Princeton University

Publications

JV Cady, RN Patel, H Oh, R Ondo, C Padgett, AH Safavi-Naeini, ACB Jayich, "Low-temperature measurements of diamond optomechanical crystals," *In preparation* (2021)

JV Cady, O Michel, KW Lee, RN Patel, CJ Sarabilis, AH Safavi-Naeini, ACB Jayich, "Diamond optomechanical crystals with embedded nitrogen-vacancy centers," *Quantum Science and Technology* **4** 024009 (2019)

D Lee, KW Lee, **JV Cady**, P Ovartchaiyapong, ACB Jayich, "Topical Review: Spins and mechanics in diamond," *Journal of Optics* **19** (3) 033001 (2017)

X Mi, **JV Cady**, DM Zajac, PW Deelman, JR Petta, "Strong coupling of a single electron in silicon to a microwave photon," *Science* **355** 156-158 (2017)

X Mi, **JV Cady**, DM Zajac, J Stehlik, LF Edge, JR Petta, "Circuit quantum electrodynamics architecture for gate-defined quantum dots in silicon," *Applied Physics Letters* **110** 043501 (2017)

X Mi, TM Hazard, C Payette, K Want, DM Zajac, **JV Cady**, JR Petta, "Magnetotransport studies of mobility limiting mechanisms in undoped Si/SiGe heterostructures," *Physical Review B* **92** (3) 035304 (2015)

Abstract

Diamond optomechanical crystals for hybrid mechanical systems

by

Jeffrey Vernon Cady

Interest in hybrid mechanical systems, in which a mechanical oscillator is coupled to quantum elements such as spins, superconducting circuits, and optical photons, has increased in recent years due to the novel means of controlling and coupling disparate quantum systems that mechanical motion enables. In this dissertation we study the specific system of diamond optomechanical crytals (OMCs), which are capable of hosting and coupling to embedded defect qubits such as nitrogen-vacancy (NV) and silicon-vacancy (SiV) center spins. We calculate the expected spin-phonon coupling rate for SiV spins interacting with a diamond OMC mechanical mode and find expected zero-point couping rates of > 1 MHz. We design, fabricate, and measure diamond OMCs, demonstrating GHz-scale mechanical modes with quality factors $> 10^5$ at liquid helium temperatures. We also measure nitrogen-vacancy center spins embedded in diamond OMCs and find $T_2 = 72$ μs, comparable to the coherence times of NV spins in bulk diamond with natural ^{13}C abundance.

Contents

Curriculum Vitae **vii**

Abstract **viii**

1 Introduction **1**
1.1 Hybrid mechanical systems 1
1.2 Diamond mechanics 4
1.3 Silicon-vacancy centers 9

2 Optomechanics **12**
2.1 Optical resonators 12
2.2 Mechanical resonators 19
2.3 Optomechanics 29

3 Strain coupling to silicon vacancy centers in diamond **37**
3.1 Introduction 37
3.2 Spin-orbit coupling in the SiV 38
3.3 Orbital-strain coupling 38
3.4 SiV spin-strain coupling 42

4 Diamond optomechanical crystal design and fabrication **46**
4.1 Device geometry 46
4.2 Simulation 50
4.3 Fabrication 63

5 Diamond optomechanical crystals with embedded nitrogen vacancy centers **75**
5.1 Introduction 75
5.2 Initial OMC tests 76
5.3 Adjustments and optimizations 77
5.4 Basic OMC characterization 78
5.5 NV center spins in diamond OMCs 82

5.6 Summary and discussion 83

6 Low-temperature characterization and optical absorption heating of diamond OMCs 87
6.1 Introduction 87
6.2 Device design and fabrication 89
6.3 Room-temperature OMC characterization 91
6.4 Low temperature characterization 92
6.5 Low temperature characterization 95
6.6 Conclusions and future directions 100

7 Future directions 102
7.1 On-resonance thermometry 102
7.2 Dissipative mechanical squeezing 104

A Experimental setup details 107
A.1 Gain calibration 107
A.2 Fiber coupling efficiency 110

Bibliography 112

Chapter 1

Introduction

1.1 Hybrid mechanical systems

As quantum systems for information processing, communication, and sensing continue to grow in size and complexity, novel methods of controlling and connecting individual subsystems are needed. Hybrid mechanical systems, which use mechanical oscillators to control and connect quantum elements, fulfill just such a role and have grown in prominence in recent years due to their ability to couple to a wide variety of quantum systems (see figure 1.1) and the number of practical advantages mechanical systems have over their photonic analogues. For example, the reduced speed of sound at a given frequency relative to the speed of light enables more compact devices; the inability of sound to propagate in vacuum reduces crosstalk between adjacent devices on a chip; and mechanical devices have been shown to be highly coherent, with mechanical quality factors exceeding 10^9 [1]. Most importantly, for us, is the ability of mechanics to facilitate interactions between quantum elements that would be difficult otherwise. Specifically, it is notoriously difficult to engineer coherent interactions between vacancy-center spins in diamond. Direct coupling between spins generally requires a very short ($\approx$ 10 nm) interaction range [2] or relies on weak coupling to electromagnetic modes for longer-range coupling [3]. However, as we will see, these spins can couple quite strongly to mechanical

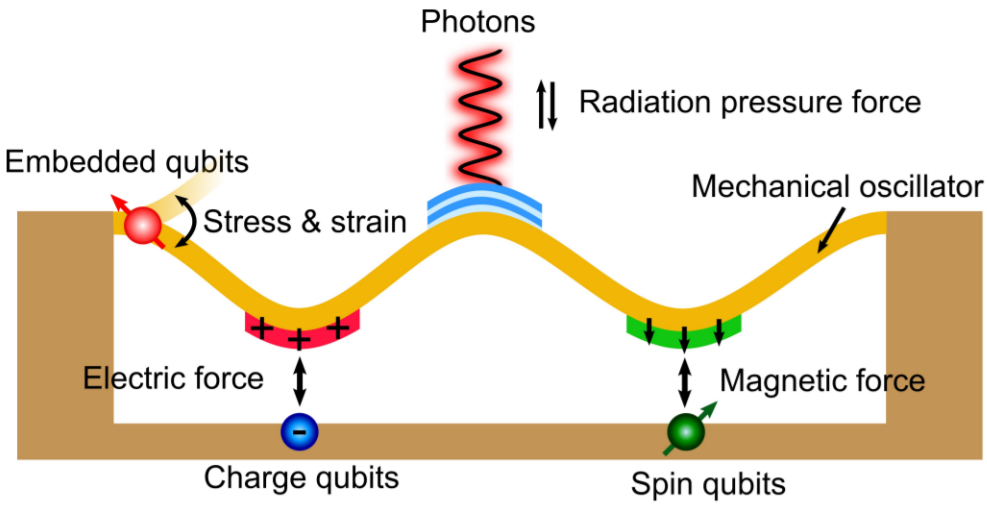

Figure 1.1: An archetypal hybrid mechanical system, in which various quantum elements interact with a common mechanical mode via a variety of different interaction forces. Figure from [5].

motion via crystal strain, enabling long-distance interactions between spins via a common mechanical mode [4].

The standard figure of merit for a qubit coupled to a mechanical resonator is the cooperativity

$$C = \frac{g^2}{\Gamma \gamma_{th}} \tag{1.1}$$

where g is the zero-point motion coupling rate between the qubit and the mechanical resonator, $\Gamma \propto T_2$ (with T_2 the coherence time of the qubit) is the decoherence rate of the qubit, and $\gamma_{th} \propto T/Q_m$ (with Q_m the mechanical resonator's quality factor and T the system bath temperature) is the thermalization rate of the mechanical resonator (see chapter 2). $C > 1$ is the rough boundary for a hybrid mechanical system existing in the quantum regime, so we see that large qubit-phonon coupling, long qubit coherence, low temperature, and large mechanical quality factor are all critical elements for creating a

high cooperativity hybrid mechanical system.

Prototypical hybrid mechanical systems included coupling between a magnetic-tipped cantilever and a single spin [6] and piezoelectric coupling between a superconducting qubit and a thin-film bulk acoustic resonator [7]. Since then, devices employing piezoelectric coupling between mechanical oscillators and superconducting qubits have pushed further into the quantum regime. Devices coupling transmon qubits to high-overtone bulk acoustic resonators (HBARs) have demonstrated very high cooperativity and creation and control of phonon Fock states [8]. Surface acoustic waves (SAWs) have also been coupled to superconducting qubits [9, 10, 11] with the added advantage that these devices are readily integrated into existing superconducting circuit architectures.

Outside of the quantum regime, many varieties of optically-active embedded defects have been coupled to mechanical motion via strain in the surrounding crystal lattice. Mechanical driving has been used to modulate the optical emission of defects in hexagonal boron nitride [12] and InAs quantum dots [13]. Mechanical driving has also been used to control defect spins in, for instance, silicon carbide [14] and diamond. It is the rich environment of diamond hybrid mechanical systems that we will concern ourselves with in the following section.

Lastly, and particularly germain to this dissertation, are devices that couple photons and mechanical motion, so-called optomechanical devices, which are most mature in silicon but have also been demonstrated in aluminum nitride [15], GaAs [16], and diamond [17, 18, 19] to name a few. Such devices have been used to demonstrate laser cooling to the mechanical ground state [20], remote entanglement of mechanical oscillators [21], and extraordinarily high mechanical quality factors exceeding 10^9 for GHz-scale modes [1]. Analogous electromechanical devices consisting of a superconducting LC oscillator with a capacitor formed by a vibrating aluminum drumhead have also been a scientifically productive platform, demonstrating, for instance, squeezing of the mechanical mode [22].

1.2 Diamond mechanics

The study of mechanics in diamond is primarily motivated by potential applications in coupling to defect centers in diamond such as the negatively charged nitrogen-vacancy (NV) and silicon-vacancy (SiV) centers, the orbital and spin degrees of freedom of which have been shown to couple to mechanical motion via crystal strain. However, diamond has a number of properties that make it a promising mechanical material. Firstly, it is a very stiff material, with a Young's modulus of 1050 GPa, nearly an order of magnitude higher than silicon. Secondly, and relatedly, it has a larger speed of sound (12,000 m/s) than silicon, such that the wavelength of a given frequency vibration is larger in diamond. This results in larger (and thus easier to fabricate) devices. The main drawback to diamond is the difficulty in fabricating monolithic mechanical structures that can take advantage of diamond's material properties. Thin films of diamond cannot be grown on other materials, so a direct analogue to silicon-on-insulator membranes is not possible. This obstacle is navigated via several fabrication protocols, including diamond-on-insulator techniques that employ wafer bonding to adhere a diamond membrane onto a removable dielectric layer [23, 24, 18], angled etching techniques [17], or quasi-isotropic diamond etches [25]. This difficulty is circumvented by employing mechanics in bulk diamond such as SAWs [26, 27] and HBARs [28], however these devices require deposition of a piezoelectric material in order to drive the mechanics.

Below, we will give an overview of different types of diamond mechanical oscillator and how they are applied in hybrid mechanical systems.

1.2.1 Diamond hybrid mechanical devices

Coupling diamond mechanical resonators to defect-centers in diamond (particularly nitrogen-vacancy (NV) and silicon-vacancy (SiV) centers) [5] has shown promise for

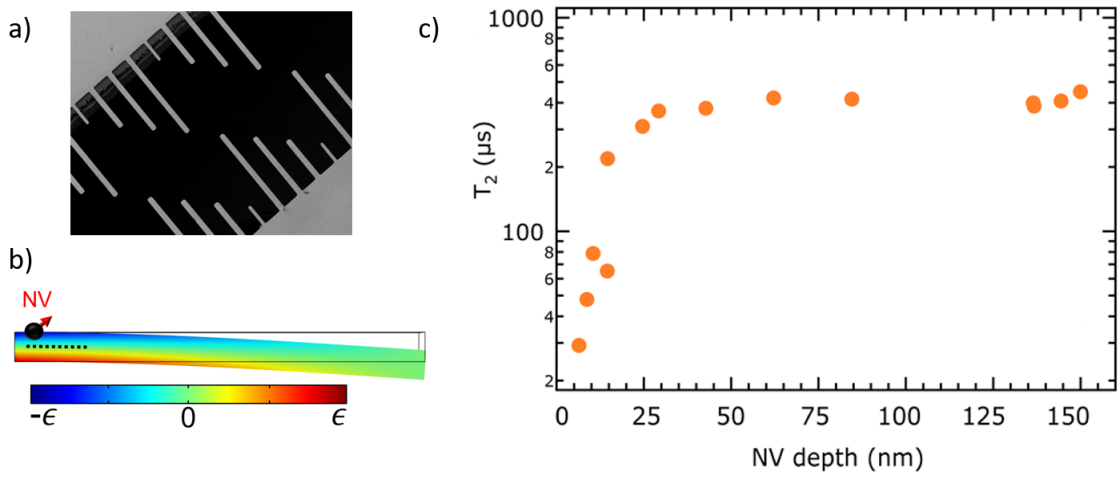

Figure 1.2: a) A scanning electron micrograph of diamond cantilevers. b) The strain profile of a singly-clamped cantilever, showing high-strain regions near the surfaces and clamping points. c) Plot of NV center spin coherence time T_2 versus depth from the diamond surface, from [38], showing reduced coherence for near-surface NVs.

many interesting quantum applications, such as coherence extension of defect spins via mechanically-driven continous dynamical decoupling [29, 30], entanglement of spatially-separated defect spins [4], and cooling of mechanical motion via phonon-assisted optical transitions [31] and spin-strain coupling in the NV center excited orbital state [32].

Cantilevers

Diamond cantilevers, consisting of singly-clamped springboards (or analogously double-clamped beams [33]) were very successful for initial implementations of devices coupling mechanical motion to nitrogen-vacancy centers in diamond due to their relative ease of fabrication, simple theoretical behavior, and ability to be driven to large amplitudes with off-the-shelf piezoelectric actuators clamped to the sample mount (due to their relatively low frequency range ($\approx$ 1 MHz)). Such devices have been used to control both the spin [34, 24] and orbital [35] states of NV centers, for measurement of the strain coupling constants [34, 36, 35], and have shown very high mechanical quality factors [23, 37].

However, cantilevers present significant obstacles to reaching the quantum regime. Their typically low frequencies make it more difficult to passively cool them into their ground state with cryogenics. Meanwhile, their strain profile (shown in figure 1.2b) is such that there is high strain near the clamping point and near the surface. This strain profile leads to large mechanical clamping losses (see chapter 2) and requires defects to be near the surface to experience high strain coupling, leading to increased decoherence as shown in figure 1.2c. These issues are only exacerbated by attempting to make smaller, higher frequency and higher strain devices, in addition to being more difficult to drive and detect the mechanical motion.

HBARs

High-overtone bulk acoustic resonators (HBARs) are formed by reflections between the top and bottom surfaces of a bulk material topped with a piezoelectric material. The large mode-volume of these devices enables interaction with a large number of defects that are deep within the bulk. Experiments with these devices have shown control of NV center spin [28, 39, 40] and orbital [41] states, and spin coherence extension with mechanically-dressed states [29]. However, these devices typically have low mechanical quality factors due to poor lateral confinement of the mechanical modes (which can be partially alleviated through focusing structures on the device surface [42]) and the large spatial extent of the mode makes it difficult to engineer single spin-single phonon interactions.

Surface Acoustic Waves

Surface acoustic waves (SAWs) consist of propagating or standing Rayleigh waves on the surface of a bulk material. Typically they are formed in piezoelectric substrates and are commonly used as filters and delay lines in communication devices. While a proper

SAW *cavity* has yet to be demonstrated in diamond, SAW devices formed by interdigital transducers (IDTs) on top of a piezoelectric layer on diamond have been employed as a way of interfacing defect centers with high frequency (GHz-scale) phonons. In particular, SAWs in diamond have been used to control the spin [43] and orbital [27] states of NV centers and the spin state of SiV centers [26].

Using SAW cavities as a means of generating quantum interactions with embedded qubits is a promising direction [44] due to their ability to be fabricated on bulk material, the high mechanical quality factors seen in SAW cavities in other materials, their ability to interact with spin ensembles and be integrated into larger microwave architectures, and a favorable strain profile that extends $\approx$ one wavelength (≈ 1 μm at 10 GHz) into the material, allowing for spins to be far from noisy surfaces.

However, high mechanical quality factors have yet to be demonstrated in diamond SAW cavities and there are open questions regarding the best way to detect the mechanical motion in diamond SAW cavities. Furthermore, the zero-point motion strain generated in these cavities is somewhat smaller than in other forms of mechanical resonator.

Disk resonators

Disk resonators [25, 45, 46] consist of circular disks tethered to the bulk by a thin interconnect and host coupled GHz-scale mechanical and telecom optical modes (making them optomechanical devices, which we discuss further below). Mechanical driving of NV center spins has been shown in these devices [19] but low mechanical quality factors and strain in these devices make it unlikely that they will reach the high-cooperativity regime.

Optomechanical crystals

Optomechanical crystals (OMCs) [47, 48, 49, 50] are nanobeams or membranes with holes etched in them with sizes, shapes, and periodicity to give bandgaps at optical and mechanical frequencies of interest, creating colocalized and coupled optical (typically 1550 nm) and mechanical (typically a few GHz). Diamond OMCs have been measured at room temperature [17, 18] and at low temperature (chapter 6 of this work) but so far no interactions between defect centers and the mechanical motion of diamond OMCs have been demonstrated. However, [18] (chapter 5 of this work) did shown an NV center with good coherence embedded in a diamond OMC, a promising result that significant nanofabrication-induced decoherence can be avoided in these structures.

Diamond OMCs have the advantage of generating high zero-point strain, having high mechanical quality factors at low temperature (chapter 6), and are able to have their mechanical motion driven, detected, and cooled optically via the optomechanical interaction. However, their small mode volume does make studies of ensemble phonon coupling difficult and there may be some difficulty linking them together in a larger quantum network, although this may be solved by the development of diamond phononic wires [51, 52].

Choosing our mechanical resonator

As shown in figure 1.3, we initially considered doubly clamped beams, SAW cavities, and optomechanical crystals for the mechanical resonator we would use to push toward the quantum regime with defect spin qubits. We simulated each architecture to determine the zero-point strain generated by their mechanical modes and found that, for a given mechanical frequency, doubly clamped beams generated the highest strain. However, concerns about clamping loss and defect qubit quality inside such small structures

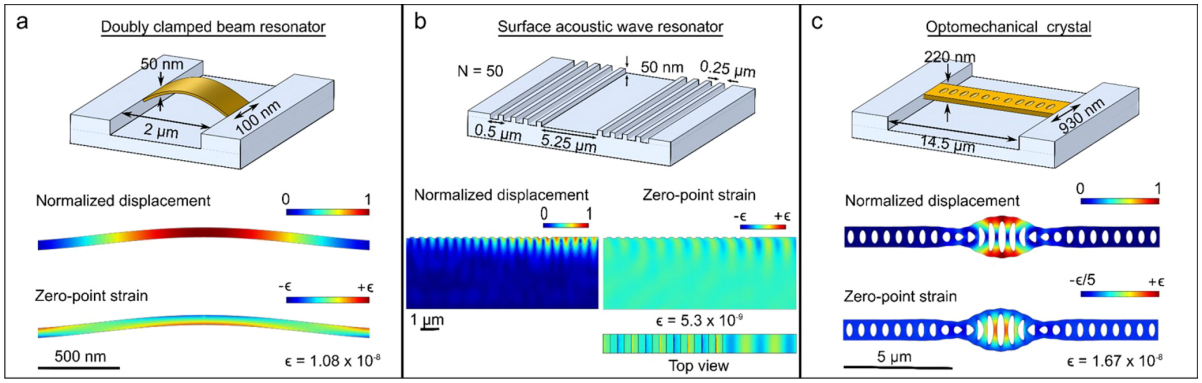

Figure 1.3: Displacement and strain profiles for the three types of mechanical resonators considered for our push into the quantum regime: a) doubly clamped beams, b) SAW cavities, and c) optomechanical crystals.

led us to decline this option. SAW cavities generated the least strain of the options considered but had the advantage of being fabricated on bulk diamond, having a strain profile that extends deep into the diamond, having the potential for high mechanical quality factors, and the ability to couple to large ensembles of spins. Concerns about driving and detecting the mechanical motion of these devices and the somewhat lower strain made us decline them for the time being, but they could be employed in future experiments that require larger numbers of spins than could reasonably fit in a much smaller optomechanical crystal (see 7). We ultimately settled on optomechanical crystals due to their large strain, z-symmetric strain profile, and proven ability to host high quality factor mechanical modes. These aspects are discussed further in chapter 4.

1.3 Silicon-vacancy centers

Negatively charged nitrogen-vacancy (NV) centers, consisting of a substitutional nitrogen atom adjacent to a vacancy in the diamond lattice, [53, 54, 55] were the focus of our lab's initial experiments with hybrid mechanical devices [34, 35] due to their ease of measurement and control, and their good quantum coherence even in ambient condi-

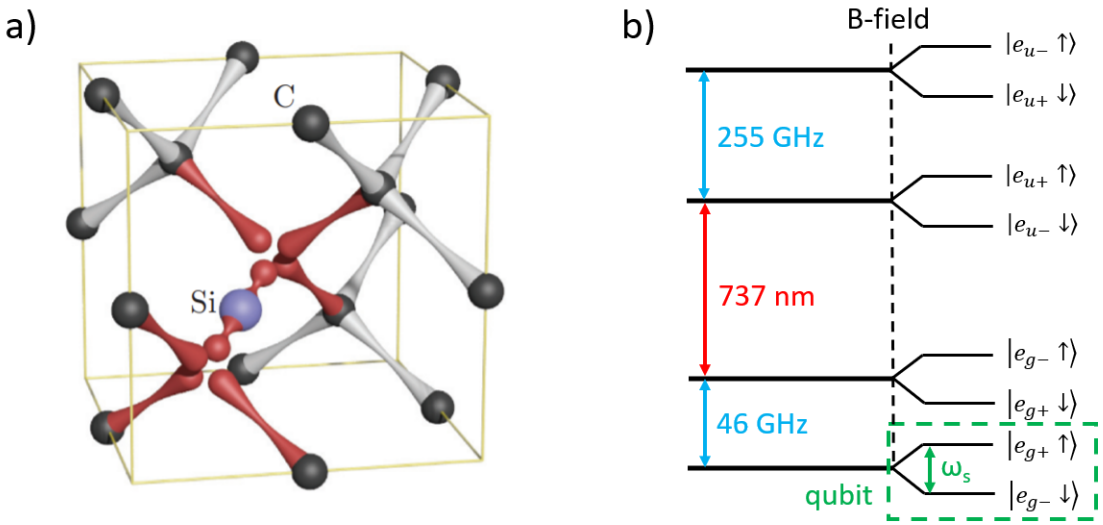

Figure 1.4: a) A schematic of the SiV center in diamond from [58]. b) An energy level diagram for the SiV center, adapted from [59].

tions. NV centers have an orbital singlet, spin triplet ground state and the spin is easily controlled using a combination of green laser pulses to optically pump the spin into the $m_s = 0$ state and microwave fields to drive transitions to the $m_s = \pm 1$ states. The same mechanism that allows for spin polarization, namely an intersystem crossing from the excited state to a metastable singlet state, also causes the $m_s = 0$ spin state to produce more photoluminescence when excited with green light. Thus, the spin state can be measured via detection of the light emitted from an NV center upon optical excitation. Taken together, the NV center is a relatively easy to use quantum platform.

However, considering measured spin-strain coupling constants [34, 36] and simulated strain generated by diamond OMCs, we predicted zero-point spin-strain coupling of only 200 Hz. Even taking into account typical OMC mechanical quality factors of 10^5 and realistic NV center spin coherence times of on the order of ms with intensive dynamical decoupling [56, 57], reaching $C > 1$ seemed difficult.

This led us to consider silicon-vacancy centers (the negatively-charged variety) [60],

which consist of an interstitial silicon atom between two adjacent vacancies in the diamond lattice (figure 1.4a). As shown in figure 1.4b, the SiV has doublet ground and excited orbital states that are separated by $\approx$ 737 nm optical transitions. The orbital splitting in both the ground and excited states is due to spin-orbit coupling from the silicon nucleus. The orbital branches can be further split by application of a magnetic field. Due to the spin-orbit coupling, these spin states inherit orbital character that makes them highly susceptible to strain [59, 26] (as discussed in detail in chapter 3). However, high strain susceptibility also makes the spin sensitive to phonons near the 50 GHz splitting of the ground state orbital branches, requiring SiV spins to be very cold in order to suppress the thermal occupation of phonons at that frequency and achieve good coherence [61].

Unlike NV centers, SiV center spins are not highly susceptible to microwave control (unless in the presence of large intrinsic strain) and therefore alternative methods of manipulating the spin have had to be developed. All-optical control with Raman pulses [62], optical pumping to initialize the spin, and even mechanical driving [26] provide a toolbox for controlling the SiV spin. SiV centers have also proven to be a promising platform for photonic quantum networks, with impressive demonstration of aligned implantation with a diamond photonic crystal [58], a technology that could be used in future hybrid mechanical experiments with SiV centers to place SiVs deterministically in the high-strain region of a mechanical resonator.

Chapter 2

Optomechanics

[63, 49, 50] all provide excellent overviews of different aspects of optomechanics, including the optical and mechanical subsystems. Here we will simply highlight important calculations, equations, and definitions for use later on.

2.1 Optical resonators

2.1.1 Quality factor

[1] Because in general we work with the fundamental (lowest frequency) mode in our optical cavity, our optical quality factor Q_o is equivalent to the finesse and is given by :

$$Q_o = \omega_{cav}\tau = \omega_{cav}/\kappa \tag{2.1}$$

where ω_{cav} is the optical cavity frequency (which is $\approx$ 190-200 THz for the $\approx$ 1550 nm light that we use in our experiment), τ is the photon lifetime, and $\kappa = 1/\tau$ is the photon decay rate. By decay, it is meant that, absent any input of light into the cavity, the

[1] Note that the discussion of quality factor can be applied to mechanical resonators as well, just replace photons with phonons and obviously the frequency scale will be different

number of photons inside as a function of time t is proportional to $e^{-\kappa t}$. Starting from this, we can derive some meaning from the equation for Q_o. Say that the energy inside the cavity is E (which is linearly proportional to the number of photons inside the cavity n_c). Assuming that $\kappa \ll \omega_{cav}$ (such that the resonator oscillates much faster then it decays), then the amount of energy lost during one oscillation is $E(1 - e^{\kappa/\omega_{cav}}) \approx E\kappa/\omega_{cav}$ (since $\Delta t = 1/\omega_{cav}$ for one oscillation and κ/ω_{cav} is small to second order). Thus the energy stored in the cavity divided by the energy lost in one oscillation is $E/(E\kappa/\omega_{cav}) = \omega_{cav}/\kappa$. Thus, the quality factor describes the fraction of the resonator's energy that it loses each oscillation. The most accurate way to measure the quality factor of a cavity is to excite the resonator (such that it has some amount of energy in it) and then measure the energy as a function of time after the excitation to extract the decay constant κ. This is a "ring down" measurement and is easier said then done, but that discussion will come later. Lastly, note that light exiting the cavity has a functional form proportional to $e^{-i\omega_{cav}t}e^{-\kappa t}$, which under Fourier transformation yields a Lorentzian in the frequency domain $\propto 1/((\omega - \omega_{cav})^2 + \kappa^2/4)$ such that measuring the response as a function of frequency will give a Lorentzian signal the width of which is κ at half of its maximum. Thus, assuming there are no other effects contributing to the linewidth, we can find the quality factor by measuring the signal in frequency space and dividing the cavity frequency (or wavelength) by the "full width half maximum" (FWHM). However, this assumption regarding the linewidth is not always a good one to make, since frequency jitter can broaden the measured linewidth, so one has to be careful when estimating the quality factor this way.

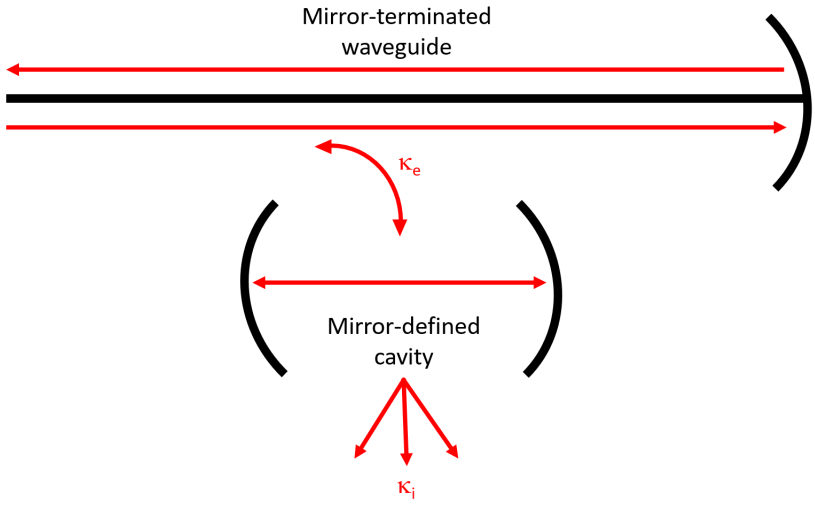

Figure 2.1: A diagram of an optical cavity evanescently coupled to a mirror-terminated optical waveguide. The waveguide and cavity are coupled with rate κ_e while light is lost from the cavity (through material losses, loss through the cavity mirrors, and scattering into vacuum) at a rate of κ_i.

2.1.2 Input-Output theory

Now assume that the cavity is coupled to an input waveguide with rate κ_e either through one of the mirrors or evanescently from the side. In our devices, it will always be the case that the input channel and the output channel are the same since we terminate the coupling waveguide with a mirror such that all light that leaves the cavity through the waveguide is directed back along the direction of the input light. Following [49] and [64], the cavity mode has Hamiltonian $H_{cav} = \hbar\omega_{cav}\hat{a}^\dagger\hat{a}$, where $\hat{a}^\dagger/\hat{a}$ are the photon creation/annihilation operators for the cavity mode and $[\hat{a}, \hat{a}^\dagger] = 1$. Similarly, the waveguide has Hamiltonian $H_{wg} = \hbar\int d\omega\omega\hat{A}^\dagger_\omega\hat{A}_\omega$, where $\hat{A}^\dagger_\omega/\hat{A}_\omega$ are the creation/annihilation operators for the waveguide mode at frequency ω, $[\hat{A}_\omega, \hat{A}^\dagger_{\omega'}] = \delta(\omega, \omega')$, and the waveguide operators commute with the cavity operators. Finally, we assume the cavity and the waveguide couple linearly with strength f_ω, such that the interaction Hamiltonian is

$$H_{int} = i\hbar \int d\omega (f_\omega \hat{A}_\omega \hat{a}^\dagger - f_\omega^* \hat{a} \hat{A}_\omega^\dagger) \tag{2.2}$$

The time evolution of the cavity and waveguide operators under the Hamiltonian $H = H_{cav} + H_{wg} + H_{int}$ is thus

$$\dot{\hat{a}} = \frac{i}{\hbar}[H, \hat{a}] = -i\omega_{cav}\hat{a} - \int d\omega f_\omega \hat{A}_\omega \tag{2.3}$$

$$\dot{\hat{A}}_\omega = \frac{i}{\hbar}[H, \hat{A}_\omega] = -i\omega \hat{A}_\omega + f_\omega^* \hat{a} \tag{2.4}$$

The equation for $\dot{\hat{A}}_\omega$ can be integrated using $e^{i\omega t}$ as an integrating factor to give

$$\hat{A}_\omega(t) = \hat{A}_\omega(t_i)e^{-i\omega(t-t_i)} + \int_{t_i}^{t} d\tau \hat{a}(\tau) f_\omega^* e^{-i\omega(t-\tau)} \tag{2.5}$$

or

$$\hat{A}_\omega(t) = \hat{A}_\omega(t_f)e^{-i\omega(t-t_f)} - \int_{t}^{t_f} d\tau \hat{a}(\tau) f_\omega^* e^{-i\omega(t-\tau)} \tag{2.6}$$

where t_i (t_f) is some initial (final) time. Substituting the solution with initial conditions into the equation for $\dot{\hat{a}}$ gives

$$\dot{\hat{a}} = -i\omega_{cav}\hat{a}(t) - \int d\omega f_\omega \hat{A}_\omega(t_i) e^{-i\omega(t-t_i)} - \int d\omega \int_{t_i}^{t} d\tau |f_\omega|^2 \hat{a}(\tau) e^{-i\omega(t-\tau)} \tag{2.7}$$

Assuming $f_\omega = f$ is constant for the frequency range of interest, the integrals in the

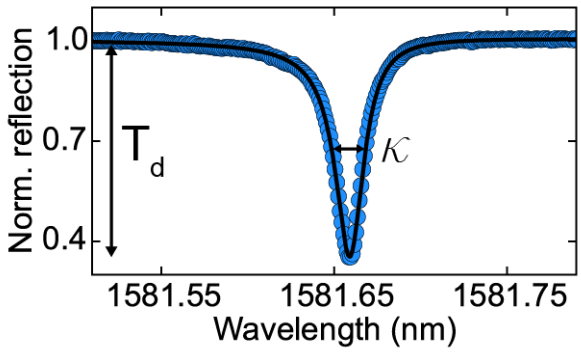

Figure 2.2: A normalized plot of reflected light as a function of wavelength that shows κ and T_d.

last term are worked out as follows:

$$\int d\omega |f_\omega|^2 \int_{t_i}^{t} d\tau \hat{a}(\tau) e^{-i(\omega)(t-\tau)} = |f|^2 \int_{t_i}^{t} d\tau \hat{a}(\tau) \int d\omega e^{-i\omega(t-\tau)} \tag{2.8}$$

$$= 2\pi |f|^2 \int_{t_i}^{t} d\tau \hat{a}(\tau)\delta(t,\tau) = \pi |f|^2 \hat{a}(t) = \frac{\kappa_e}{2}\hat{a}(t) \tag{2.9}$$

where we have used the integration identities $\int d\omega e^{-i\omega(t-\tau)} = 2\pi\delta(t,\tau)$, $\int_{t_i}^{t} d\tau a(t)\delta(t,\tau) = a(t)/2$, and defined $\kappa_e = 2\pi|f|^2$. Further, we define $\hat{a}_{in}(t)$ as

$$\hat{a}_{in}(t) = -\frac{1}{\sqrt{2\pi}} \int d\omega \hat{A}_\omega(t_i) e^{-i\omega(t-t_i)} \tag{2.10}$$

Putting all of this together, moving into a frame rotating at our laser frequency ω_L, and defining $\Delta = \omega_L - \omega_{cav}$ the equation for $\dot{\hat{a}}$ becomes

$$\dot{\hat{a}}(t) = i\Delta\hat{a}(t) + \sqrt{\kappa_e}\hat{a}_{in}(t) - \frac{\kappa_e}{2}\hat{a}(t) \tag{2.11}$$

Finally, defining $\hat{a}_{out}(t)$ as

$$\hat{a}_{out}(t) = \frac{1}{\sqrt{2\pi}} \int d\omega \hat{A}_{\omega}(t_f) e^{-i\omega(t-t_f)} \tag{2.12}$$

we find another equation for $\dot{\hat{a}}$

$$\dot{\hat{a}}(t) = i\Delta\hat{a}(t) - \sqrt{\kappa_e}\hat{a}_{out}(t) + \frac{\kappa_e}{2}\hat{a}(t) \tag{2.13}$$

Subtracting 2.11 and 2.13 gives us the boundary condition for the cavity[2]

$$\hat{a}_{in} + \hat{a}_{out} = \sqrt{\kappa_e}\hat{a} \tag{2.14}$$

We then define as κ_i the sum of all other loss rates (loss in the device or substrate material, scattering into the vacuum, light that exits either of the cavity mirrors but isn't collected). Thus, the total loss rate κ that was discussed in the previous section is[3] $\kappa = \kappa_i + \kappa_e$. κ_i just enters equation 2.11 as another decay term $-\kappa_i/2\hat{a}(t)$ such that the equation for $\dot{\hat{a}}$ including internal losses is

$$\dot{\hat{a}}(t) = i\Delta\hat{a}(t) + \sqrt{\kappa_e}\hat{a}_{in}(t) - \frac{\kappa}{2}\hat{a}(t) \tag{2.15}$$

In the steady state, $\dot{\hat{a}} = 0$ and we can solve for $\langle\hat{a}\rangle$

[2]Some references will give the boundary condition as $\hat{a}_{out} - \hat{a}_{in} = \sqrt{\kappa_e}$, which is just the result of defining $\hat{a}_{in}$ and $\hat{a}_{out}$ with the same sign, it doesn't change the solutions.

[3]In the review paper they use κ_0 and κ_{ex} instead of κ_i and κ_e

$$\langle \hat{a} \rangle = \frac{\sqrt{\kappa_e}\langle \hat{a}_{in} \rangle}{i\Delta - \frac{\kappa}{2}} \tag{2.16}$$

from which we can find the average number of photons in the cavity $n_c = |\langle \hat{a} \rangle|^2$

$$n_c = \frac{\kappa_e}{\Delta^2 + \frac{\kappa^2}{4}} \frac{P_{in}}{\hbar \omega_L} \tag{2.17}$$

where $P_{in} = \hbar\omega_L |\langle \hat{a}_{in} \rangle|^2$ is the input power to the cavity. The transmission coefficient for the cavity (which is the same as reflection for the single-sided cavity) is

$$T = \frac{\langle \hat{a}_{out} \rangle}{\langle \hat{a}_{in} \rangle} = 1 - \frac{\kappa_e}{i\Delta + \frac{\kappa}{2}} \tag{2.18}$$

At $\Delta = 0$ (i.e. on resonance with the cavity) $T = 1 - 2\kappa_e/\kappa$. The transmission on resonance is then

$$|T|^2 = 1 - \frac{4\kappa_e}{\kappa} + \frac{4\kappa_e^2}{\kappa^2} \tag{2.19}$$

from which we can extract a *transmission depth* T_d (transmission on resonance relative to transmission far off resonance (which is 1 for large Δ)).

$$T_d = 1 - |T|^2 = \frac{4\kappa_e}{\kappa} - \frac{4\kappa_e^2}{\kappa^2} \tag{2.20}$$

Solving for κ_e gives

$$\kappa_e = \frac{\kappa \pm \kappa\sqrt{1 - T_d}}{2} \tag{2.21}$$

So, in practice, by normalizing the measured cavity response and extracting T_d and κ (the total linewidth) from the plot, you can extract κ_e. The plus sign would be the case where the cavity is overcoupled $\kappa_e > \kappa/2$, whereas the minus sign would be the case where the cavity is undercoupled $\kappa_e < \kappa/2$. Whether the cavity is over- or undercoupled can be determined from an 'OMIT-type' measurement of the cavity resonance, as discussed in chapter 6.

2.2 Mechanical resonators

2.2.1 Damped mechanical resonator

A mechanical resonator is a mass or collection of masses that obey the spring equation

$$m_{\text{eff}}\ddot{x}(t) + m_{\text{eff}}\omega_m^2 x(t) = F_{ext}(t) \tag{2.22}$$

where m_{eff} is the effective mass[4] of the system, ω_m is a frequency at which the system possesses a normal mode that solves the equation, and $F_{ext}(t)$ is the sum of all external forces acting on the resonator, such as thermal and optomechanical forces, in our case. $x(t) \propto \sin(\omega_m t)$ here is an overall, time-dependent scaling of the motion, which is multiplied by a normalized spatially-dependent function $\vec{u}(\vec{r})$ that is determined by the

[4]The effective mass captures the fact that in a continuous system not every point contributes equally to the energy of the system. We will discuss this further below.

geometry and boundary conditions of the system and which characterizes the displacement at a given point in the system in order to give the total time-dependent displacement throughout the system $\vec{u}(\vec{r},t) = x(t)\vec{u}(\vec{r})$. This elucidates that a normal mode is a collection of displacements in the mechanical system that all oscillate at the same frequency ω_m. These modes are called "normal" because they are orthogonal to one another. That is to say, for two different normal modes of a system characterized by $\vec{u}_i(\vec{r})$ and $\vec{u}_j(\vec{r})$, then $\int dV \rho(\vec{r})\vec{u}_i(\vec{r}) \cdot \vec{u}_j(\vec{r}) = 0$ where ρ is the density of the material. Practically, this means that for an ideal system (no damping), driving one normal mode will not excite any other normal modes. For small discrete systems of masses and simple continuous geometries such as cantilevers, the shapes of the normal modes can be calculated analytically. For more complicated geometries, such as our OMCs, the shape of the normal modes can be found using finite-element simulation in COMSOL, which breaks the geometry up into small pieces and estimates solutions to the differential equation that describes the elastic interactions between all of those pieces. Linear damping of the motion at a rate γ_m can be included such that the total equation is

$$m_{\text{eff}}\ddot{x}(t) + m_{\text{eff}}\gamma_m\dot{x}(t) + m_{\text{eff}}\omega_m^2 x(t) = F_{ext}(t) \tag{2.23}$$

Assuming no external force, we can solve for the form of x by guessing a solution $x(t) \propto e^{ct}$ and solving for c. This gives

$$c = -\frac{\gamma_m}{2} \pm \sqrt{\frac{\gamma_m^2}{4} - \omega_m^2} \tag{2.24}$$

which results in three different cases: overdamping ($\gamma_m/2 > \omega_m$), critical damping

($\gamma_m/2 = \omega_m$), and underdamping ($\gamma_m/2 < \omega_m$). Only in the case of underdamping is the square root imaginary, giving oscillatory motion. This will always be the case for our systems, in which ω_m is generally several orders of magnitude larger than γ_m, giving $c \approx -\gamma_m/2 \pm i\omega_m$. The form of $x(t)$ in this case is

$$x(t) \propto e^{-\gamma_m t/2} e^{\pm i\omega_m t} \tag{2.25}$$

From this form, it can be seen that the oscillation amplitude decays as $\gamma_m/2$, whereas the energy in the resonator, which goes as x^2, decays as γ_m. As we will see, this is quantum-mechanically the same as how we defined decay in the case of the optical cavity, since $x \propto \hat{b}$, where $\hat{b}$ is the phonon creation operator for the mechanical mode, while the energy is proportional to $\langle \hat{b}^\dagger \hat{b} \rangle$, so you would expect the decay rate for the energy to be double that for the vibration amplitude.

For a sinusoidal driving force $F_{ext}(t) = F_0 e^{-i\omega t}$, $x(t)$ will have a steady state form of $x(t) = F_0 \chi_m e^{-i(\omega t + \phi)}$, where ϕ is a phase lag and χ_m is the mechanical susceptibility, which can be solved for by plugging this form of $x(t)$ into eq. 2.23

$$\chi_m = \frac{1}{m_{\text{eff}}((\omega_m^2 - \omega^2) - i\omega\gamma_m)} \tag{2.26}$$

When $\omega \approx \omega_m$, $(\omega_m^2 - \omega^2) \approx 2\omega_m(\omega_m - \omega)$, such that the approximately Lorentzian form of χ_m for small γ_m becomes clear

$$\chi_m(\omega \approx \omega_m) \approx \frac{1}{m_{\text{eff}}\omega_m(2(\omega_m - \omega) - i\gamma_m)} \tag{2.27}$$

Lastly, we by defining the mechanical quality factor $Q_m = \omega_m/\gamma_m$, we see that on resonance ($\omega = \omega_m$), the susceptibility is $\chi_m(\omega = \omega_m) = iQ_m/m_{\text{eff}}\omega_m^2$, so the larger the mechanical quality factor, the more of an effect a given force has on the amplitude of motion.

2.2.2 Effective mass

It may have been apparent that there is a degree of flexibility to how the mode profile $\vec{u}(\vec{r})$ mentioned in the previous section is normalized. This choice effects the magnitude of the time-dependent $x(t)$ term since $\vec{u}(\vec{r}, t) = x(t)\vec{u}(\vec{r})$. A common choice is to set $\max[|\vec{u}(\vec{r})|] = 1$. This choice then effects how the effective mass is defined, since the elastic energy must equal $m_{\text{eff}}\omega_m^2\langle x^2\rangle/2$. For the choice of scaling above where $\max[\vec{u}(\vec{r})] = 1$, the effective mass becomes an integral over the mode shape.

$$m_{\text{eff}} = \int_V d\vec{r}\rho(\vec{r})|\vec{u}(\vec{r})|^2 \tag{2.28}$$

Practically speaking, when COMSOL solves for a normal mode, it does not provide a normalized mode shape, so we must account for that when using a COMSOL solution (which is an unnormalized $\vec{u}(\vec{r})$), by just dividing eq. 2.29 by $\max[|\vec{u}(\vec{r})|^2]$, giving a more general equation for m_{eff}

$$m_{\text{eff}} = \frac{\int_V d\vec{r}\rho(\vec{r})|\vec{u}(\vec{r})|^2}{\max[|\vec{u}(\vec{r})|^2]} \tag{2.29}$$

2.2.3 The simple harmonic oscillator Hamiltonian

Moving on, the review glosses over the quantum mechanical formulation of a mechanical oscillator, specifically using a creation/annihilation operator formalism like the one we used for the optical cavity. It is worth quickly deriving for reference purposes. The simple harmonic oscillator potential at frequency ω_m is just the integral of the spring force in eq. 2.22: $V = \int_0^x dx m_{\text{eff}}\omega_m^2 x = m_{\text{eff}}\omega_m^2 x^2/2$, so the simple harmonic oscillator Hamiltonian is

$$H_{SHO} = \frac{1}{2}m_{\text{eff}}\omega_m^2\hat{x}^2 + \frac{\hat{p}^2}{2m_{\text{eff}}} \tag{2.30}$$

Where $\hat{x}$ and $\hat{p}$) are the position and momentum operators. Next, a simple algebraic trick is performed where you recognize that this is a sum of squares, which can be factored as such:

$$\frac{m_{\text{eff}}\omega_m^2}{2}(\hat{x}^2 + \frac{\hat{p}^2}{m_{\text{eff}}^2\omega_m^2}) = \frac{m_{\text{eff}}\omega_m^2}{2}(\hat{x} + i\frac{\hat{p}}{m_{\text{eff}}\omega_m})(\hat{x} - i\frac{\hat{p}}{m_{\text{eff}}\omega_m}) \tag{2.31}$$

Note that this is not equivalent to the Hamiltonian, since the position and momentum operators do not commute, but it does motivate the definition of operators $\hat{o}$ and $\hat{o}^\dagger$ which can be further investigated:

$$\hat{o} = \sqrt{\frac{m_{\text{eff}}\omega_m^2}{2}}(\hat{x} + i\frac{\hat{p}}{m_{\text{eff}}\omega_m}), \hat{o}^\dagger = \sqrt{\frac{m_{\text{eff}}\omega_m^2}{2}}(\hat{x} - i\frac{\hat{p}}{m_{\text{eff}}\omega_m}) \tag{2.32}$$

which have units of square root energy. The product $\hat{o}^\dagger\hat{o}$ can be found to be (recalling

$[\hat{x}, \hat{p}] = i\hbar$)

$$\hat{o}^\dagger \hat{o} = \frac{1}{2} m_{\text{eff}} \omega_m^2 \hat{x}^2 + \frac{\hat{p}^2}{2m_{\text{eff}}} + \frac{i\omega_m}{2}[\hat{x}, \hat{p}] = H_{SHO} - \frac{\hbar\omega_m}{2} \tag{2.33}$$

so that $H_{SHO} = \hat{o}^\dagger \hat{o} + \hbar\omega_m/2$. Similarly, $\hat{o}\hat{o}^\dagger = H_{SHO} + \hbar\omega_m/2$, such that $[\hat{o}, \hat{o}^\dagger] = \hbar\omega_m$. Finally, we define the boson creation and annihilation operators $\hat{b}^\dagger$ and $\hat{b}$ by dividing $\hat{o}^\dagger$ and $\hat{o}$ by $\sqrt{\hbar\omega_m}$ to make the operators unitless (since we'll usually end up caring about the number of phonons in the oscillator, not the energy), giving

$$\hat{b} = \sqrt{\frac{m_{\text{eff}}\omega_m}{2\hbar}}(\hat{x} + i\frac{\hat{p}}{m_{\text{eff}}\omega_m}), \hat{b}^\dagger = \sqrt{\frac{m_{\text{eff}}\omega_m}{2\hbar}}(\hat{x} - i\frac{\hat{p}}{m_{\text{eff}}\omega_m}) \tag{2.34}$$

for which $H_{SHO} = \hbar\omega_m \hat{b}^\dagger \hat{b} + \frac{\hbar\omega_m}{2}$ and $[\hat{b}, \hat{b}^\dagger] = 1$. Note that if a state ψ has energy E (i.e. $H_{SHO}\psi = E\psi$), then the state $\hat{b}^\dagger\psi$ has energy $E + \hbar\omega_m$ while $\hat{b}\psi$ has energy $E - \hbar\omega_m$, so $\hat{b}^\dagger/\hat{b}$ creates/annihilates a phonon of energy $\hbar\omega_m$ in the system. We can define number states that correspond to states of integral phonon occupation in the resonator, where a state with n phonons is given by $(\hat{b}^\dagger)^n|0\rangle$, where $|0\rangle$ is the zero-phonon vacuum state, for which $\hat{b}|0.\rangle = 0$. We then see that the expectation value of $\hat{b}^\dagger\hat{b}$ for a given state $|n\rangle$ is $\langle n|\hat{b}^\dagger\hat{b}|n\rangle = n$, so that $\hat{b}^\dagger\hat{b}$ is the phonon number operator.

We can solve for $\hat{x}$ in terms of these operators:

$$\hat{x} = \sqrt{\frac{\hbar}{2m_{\text{eff}}\omega_m}}(\hat{b} + \hat{b}^\dagger) \tag{2.35}$$

While for the ground state, $\langle\hat{x}\rangle = \langle 0|\hat{x}|0\rangle = 0$, $\langle\hat{x}^2\rangle = \hbar/2m_{\text{eff}}\omega_m = x_{zpf}^2$, where we have defined the zero-point fluctuation amplitude x_{zpf}

$$x_{zpf} = \sqrt{\frac{\hbar}{2m_{\text{eff}}\omega_m}} \tag{2.36}$$

The potential energy in the ground state is therefore $m_{\text{eff}}\omega_m^2 x_{zpf}^2/2 = \hbar\omega_m/4$, which is half of the vacuum energy $\langle 0|H_{SHO}|0\rangle = \hbar\omega_m/2$. We could have arrived at the zero-point fluctuation amplitude by recognizing that the average potential energy would be half of the zero-point energy (corresponding to strain energy in the resonator) while the other half would correspond to the kinetic energy of the masses in the system. Thus, we could just set $m_{\text{eff}}\omega_m^2 x_{zpf}^2/2 = \hbar\omega_m/4$ and solve for x_{zpf}. Recalling our discussion of effective mass, we see that the way we define effective mass in turn affects x_{zpf}, so consistency is important.

2.2.4 Thermalization

When the mechanical resonator is coupled to a thermal bath at temperature T that has phonon occupation $n_{th} \approx k_B T/\hbar\omega_m$ with rate γ_m (the damping or decay rate previously mentioned), then the phonon number $\overline{n}$ in the resonator will decay with rate $\overline{n}\gamma_m$ and increase with rate $n_{th}\gamma_m$ as phonons decay out of the resonator and leak into it from the bath. Thus, $\frac{d\overline{n}}{dt} = -\gamma_m(\overline{n} - n_{th})$. Thus, for $\overline{n} = 0$, we have $\frac{d\overline{n}}{dt} = \gamma_m n_{th}$, which we define as the *thermalization rate* γ_{th} at low temperature

$$\gamma_{th} = \gamma_m n_{th} \approx \frac{\gamma_m k_B T}{\hbar\omega_m} = \frac{k_B T}{\hbar Q_m} \tag{2.37}$$

where we recall the mechanical quality factor $Q_m = \omega_m/\gamma_m$. Note that the thermalization rate goes to 0 as T goes to 0, so its importance diminishes for very low temperatures

($n_{th} \ll 1$) while at moderately high temperatures ($n_{th} > 1$) it is the dominant phonon decoherence mechanism. This distinction is important when we consider quantum interactions between the mechanical resonator and other systems and want to define a cooperativity for the interaction, which will go as $1/\Gamma_m$ with Γ_m the phonon decoherence rate. For higher temperatures, $\Gamma_m \approx \gamma_{th}$, while at lower temperatures, $\Gamma_m \approx \gamma_m$, or whatever the mechanical linewidth is due to other effects such as frequency jitter.

2.2.5 Mechanical damping mechanisms

There are many different mechanisms which contribute to the total mechanical damping, the relative importance of which vary with temperature, pressure, and device design. [50] gives a good overview of most of them. The mechanisms that account for most damping are viscous damping, Akhieser/Landau-Rumer damping, thermoelastic damping, clamping loss, and two-level system damping. Each mechanism has an associated quality factor, which add in inverse to give the total quality mechanical quality factor

$$Q_m^{-1} = \frac{1}{Q_{\text{vis}}} + \frac{1}{Q_{\text{A/LR}}} + \frac{1}{Q_{\text{TE}}} + \frac{1}{Q_{\text{CL}}} + \frac{1}{Q_{\text{TLS}}} \tag{2.38}$$

Viscous damping is due to interactions between the mechanical resonator surface and the surrounding medium (air, for instance) and can be mitigated by simply measuring the resonator in vacuum, with higher vacuum leading to less viscous damping. Viscous damping can also arise from lossy material deposited on the sample, such as the bonding agent to which we attribute the low mechanical quality factors in chapter 5 or material that cryopumps onto the device at low temperature.

Akhieser and Landau-Rumer [65, 66] damping correspond to interactions between thermal phonons in the material and phonons in the acoustic mode that result in energy

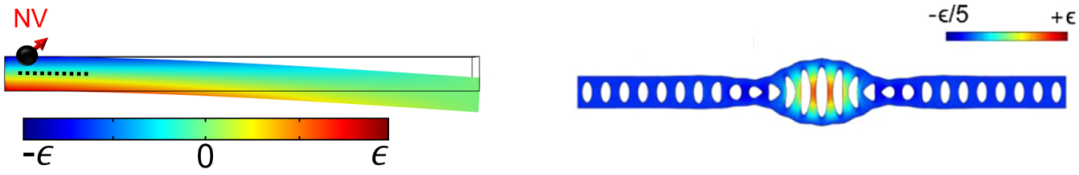

Figure 2.3: Left: the strain profile of a singly-clamped cantilever, showing high strain at the clamping point. Right: The strain profile of the breathing mode of an optomechanical crystal, showing low strain at the clamping points.

being carried away from the acoustic mode. Akhieser damping is valid for higher temperatures where the thermal phonon lifetime is short (increasing likelihood of interaction with acoustic phonons), while Landau-Rumer damping is valid at lower temperatures and is characterized by three-phonon scattering processes between acoustic phonons and single thermal phonons. Both mechanisms lead to damping rates that scale linearly with temperature.

Thermoelastic damping [67] results from strain-generated thermal gradients within the device that result from the device's vibration. The process of these gradients equilibrating absorbs energy from the acoustic mode. At lower temperatures, these temperature gradients become smaller due to a reduced coefficient of thermal expansion, so thermoelastic damping is primarily a high-temperature effect [5].

At room temperature in air, the mechanical quality factor of our optomechanical crystals is dominated by viscous, Akhieser, and thermoelastic damping, with $Q_{\mathrm{vis}} \approx Q_{\mathrm{A+TE}} \approx 10^4$, as we see Q_m approximately double from 5,000-6,000 in ambient conditions to 11,000-13,000 in vacuum.

Clamping loss takes into account the fact the mechanical resonator is not floating in space, but is in fact tethered to a bulk somewhere. Clamping losses consist of mechanical

[5]COMSOL simulations of the thermoelastic damping of a diamond optomechanical crystal at 300K give $Q_{\mathrm{TE}} = 90,000$, however this uses the bulk thermal conductivity of diamond, which may deviate from its thin-film value [68]

energy radiated from the clamping point into the bulk. The strain profile of a cantilever on the left side of figure 2.3 demonstrates the high strain generated at the clamping point, leading to energy being radiated into the bulk. These losses can be mitigated by minimizing the strain induced by the resonator motion at the clamping points. This is achieved in OMCs by the Bragg-like quasi-mirrors (discussed further in chapter 4) that attenuate modes at the mechanical frequency of interest, confining strain to the center of the device, as shown in the strain profile of an OMC shown on the right of figure 2.3. However, this isolation is not perfect [50], and fabrication imperfections can couple the OMC mechanical mode to modes that can leak through the Bragg mirror and generate clamping losses. These losses are further suppressed by surrounding the clamping point with a phononic shield that hosts a full bandgap around the OMC mechanical frequency such that mechanical radiation in a wide band around the OMC mechanical frequency cannot be emitted into the bulk, allowing for very highly-confined mechanical modes.

The last and weakest (but by no means the least important) damping mechanism is coupling to two-level systems (TLSs) [1], structural defects within the device material (generally near the surface, in the native oxide layer of silicon, for example) and which have two energetic configurations which can be excited by coupling to the mechanical resonator's motion. When these TLSs relax, they emit energy back into the mechanical resonator, but not necessarily into the mode of interest. For OMCs, this results in coupling to modes that lie outside the quasi- and full bandgaps of the Bragg mirror and phononic shield, providing an avenue for mechanical loss through the clamping point. This mechanism is what ultimately limits the mechanical quality factors of silicon OMCs.

2.3 Optomechanics

2.3.1 Optomechanical Hamiltonian

The prototypical optomechanical system consists of an optical cavity with one moveable mirror, such that the cavity length L is dependent on the position x of the moveable mirror, as shown in figure 2.4. In this case the cavity frequency ω_c can be expanded to first order in x

$$\omega_c(x) \approx \omega_c + x\frac{\partial \omega_c}{\partial x} \tag{2.39}$$

Using this and $x \to x_{zpf}(\hat{b} + \hat{b}^\dagger)$ we can rewrite the Hamiltonian for the optical mode

$$\hbar\omega_c(x)\hat{a}^\dagger\hat{a} \approx \hbar(\omega_c + x_{zpf}\frac{\partial \omega_c}{\partial x}(\hat{b} + \hat{b}^\dagger))\hat{a}^\dagger\hat{a} \tag{2.40}$$

We then can make the definition $g_0 = -x_{zpf}\partial\omega_c/\partial x$[6] and write the interaction portion of the Hamiltonian as $H_{OM} = -\hbar g_0 \hat{a}^\dagger\hat{a}(\hat{b} + \hat{b}^\dagger)$, where g_0 is the vacuum optomechanical coupling rate and corresponds to the change in cavity frequency due to zero-point motion of the mechanical mode.

Thus, the entire optomechanical Hamiltonian is

$$H = \hbar\omega_c\hat{a}^\dagger\hat{a} + \hbar\omega_m\hat{b}^\dagger\hat{b} - \hbar g_0\hat{a}^\dagger\hat{a}(\hat{b} + \hat{b}^\dagger) \tag{2.41}$$

[6]The sign convention here is such that a positive displacement lengthens the cavity and thus lowers the cavity frequency.

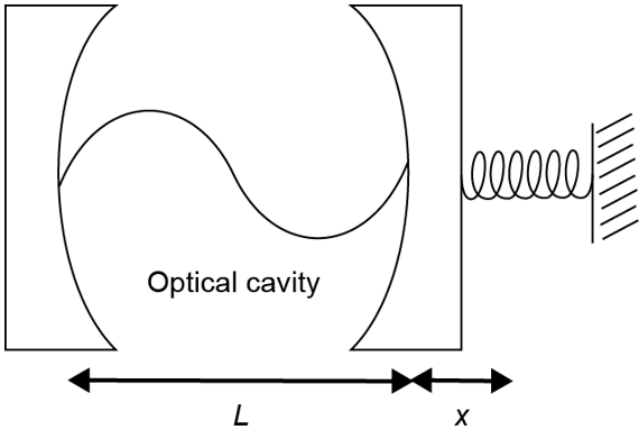

Figure 2.4: A prototypical optomechanical cavity consisting of an optical cavity with one moveable mirror.

We note that this Hamiltonian is general, g_0 need not (and often does not) correspond to a physical lengthening of an optical cavity, but encapsulates all mechanisms that lead to a change of an optical cavity frequency due to the motion of a mechanical oscillator. The two mechanisms that we treat in further detail later on are the moving boundary and photoelastic contributions.

As in section 2.1.2, we typically apply a laser drive tone at ω_L and transform into a basis rotating at that frequency using the rotating wave approximation (RWA)

$$H = \hbar\Delta\hat{a}^\dagger\hat{a} + \hbar\omega_m\hat{b}^\dagger\hat{b} - \hbar g_0\hat{a}^\dagger\hat{a}(\hat{b} + \hat{b}^\dagger) \tag{2.42}$$

where $\Delta = \omega_c - \omega_L$. To proceed, it is typical to linearize the optical field by introducing the transformation $\hat{a} \to \alpha + \hat{a}$ where α is the large steady-state photon amplitude such that $|\alpha|^2 = n_c$ and $\hat{a}$ describes the quantum dynamics that occur on top of that steady-state. Applying this transformation and keeping terms that are linear in α (the quadratic terms in α describe steady state phenomena and the quadratic terms in $\hat{a}$ are small), the

optomechanical dynamics are captured by

$$H = \hbar\Delta\hat{a}^\dagger\hat{a} + \hbar\omega_m\hat{b}^\dagger\hat{b} - \hbar G(\hat{a}^\dagger + \hat{a})(\hat{b} + \hat{b}^\dagger) \tag{2.43}$$

where $G = g_0\alpha = g_0\sqrt{n_c}$ is the optomechanical coupling due to the steady-state photon amplitude. When $\Delta = \omega_m$ (which we refer to as the red sideband and is the regime we will work in later on), the Hamiltonian describes two oscillators of equal frequency that can exchange quanta. Thus, we only keep excitation-preserving terms in the interaction Hamiltonian

$$H_{OM,\text{rsb}} = -\hbar G(\hat{a}^\dagger\hat{b} + \hat{a}\hat{b}^\dagger) \tag{2.44}$$

This elucidates the mechanism behind optomechanical cooling of the mechanical mode, in which quanta of mechanical energy are transferred into the cold optical mode.

As we did for the optical resonator above, we can generate equations of motions for the optomechanical system

$$\dot{\hat{a}} = -(i\Delta + \frac{\kappa}{2})\hat{a} - ig_0\hat{a}(\hat{b} + \hat{b}^\dagger) - \sqrt{\kappa_e}\hat{a}_{\text{in}} \tag{2.45}$$

$$\dot{\hat{b}} = -(i\omega_m + \frac{\gamma_i}{2})\hat{b} - ig_0\hat{a}^\dagger\hat{a} - \sqrt{\gamma_i}\hat{b}_{\text{in}} \tag{2.46}$$

where γ_i is the intrinsic mechanical damping and $\hat{a}_{\text{in}}$ and $\hat{b}_{\text{in}}$ are the optical input field and thermal bath noise operator, respectively.

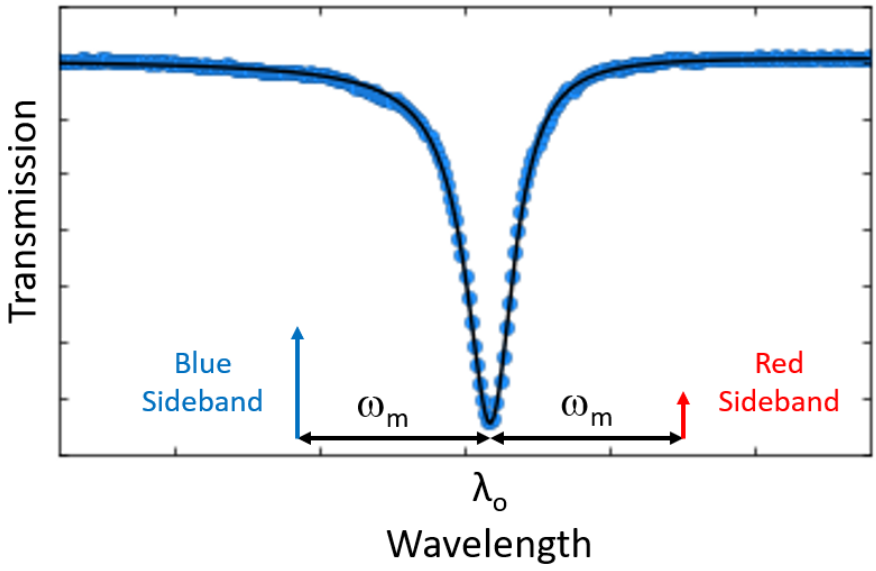

Figure 2.5: The positions of the red and blue sidebands relative to the optical cavity spectrum.

2.3.2 Optomechanical effects

Solving these equations of motion [49, 63, 50] illuminates the effects of the optomechanical coupling on the mechanical mode. Of interest to us is the effect on the mechanical mode frequency and damping. The optomechanical interaction introduces an extra damping term γ_{OM} into the overall damping of the mechanical mode, such that the total damping $\gamma = \gamma_i + \gamma_{OM}$ where

$$\gamma_{OM} = G^2 \left(\frac{-\kappa}{\kappa^2/4 + (\Delta + \omega_m)^2} + \frac{\kappa}{\kappa^2/4 + (\Delta - \omega_m)^2} \right) \tag{2.47}$$

This reduces to $\gamma_{OM} \approx \pm 4G^2/\kappa$ for $\Delta = \pm\omega_m$, such that on the red sideband ($\Delta = \omega_m$, the optomechanical interaction adds damping, while on the blue sideband ($\Delta = -\omega_m$ the interaction leads to anti-damping, to the point where for high enough G we have $\gamma < 0$, leading to a phonon lasing condition where the mechanical mode can reach

extremely large amplitudes. We also define the optomechanical cooperativity on the sidebands

$$C = |\frac{\gamma_{OM}}{\gamma_i}| \approx \frac{4G^2}{\kappa\gamma_i} \tag{2.48}$$

The optomechanical interaction also shifts the mechanical frequency by

$$\delta\omega_m = -G^2\left(\frac{(\Delta-\omega_m)}{\kappa^2/4+(\Delta-\omega_m)^2} + \frac{(\Delta+\omega_m)}{\kappa^2/4+(\Delta+\omega_m)^2}\right) \tag{2.49}$$

Furthermore, by solving for the phonon operator spectrum $\hat{b}(\omega)$ [50], one can calculate the steady state phonon occupation of the mechanical mode

$$\langle\hat{b}^\dagger(t)\hat{b}(t)\rangle = \frac{1}{2\pi}\int_{-\infty}^{\infty} d\omega S_{bb}(\omega) \tag{2.50}$$

where $S_{bb}(\omega)$ is the spectral density of $\hat{b}$

$$S_{bb}(\omega) = \int_{-\infty}^{\infty} d\omega' \langle\hat{b}^\dagger(\omega)\hat{b}(\omega')\rangle \tag{2.51}$$

The result of these integrations is steady state phonon occupancy as a function of laser detuning

$$\overline{n}(\Delta) = \frac{\gamma_i n_b}{\gamma} + \frac{|G|^2\kappa}{\gamma}\frac{1}{\kappa^2/4+(\Delta+\omega_m)^2} \tag{2.52}$$

From this we can see that as more photons are put into the cavity, C gets larger and $\overline{n}$ gets smaller, such that applying a laser tone on the red sideband cools the mechanical mode. Also note that $(\kappa/4\omega_m)^2$ sets a lower bound on the final phonon occupancy.

In particular, for the red sideband $\Delta = \omega_m$, the phonon occupation is

$$\overline{n} \approx \frac{\gamma_i n_b}{\gamma} + \frac{\gamma_{OM}}{\gamma}\Big(\frac{\kappa}{4\omega_m}\Big)^2 = \frac{n_b}{1+C} + \frac{C}{1+C}\Big(\frac{\kappa}{4\omega_m}\Big)^2 \tag{2.53}$$

2.3.3 Optomechanical coupling mechanisms

For our OMCs, we only concern ourselves with two optomechanical coupling mechanisms: the moving boundary contribution g_{mb} and the photoelastic contribution g_{pe} which add together to give the total vacuum optomechanical coupling rate

$$g_0 = g_{mb} + g_{pe} \tag{2.54}$$

Moving boundary optomechanical coupling

The moving boundary contribution to the optomechanical coupling is typically the smaller of the two contributions and arises from the change in shape of the mechanical resonator while it is oscillating, modifying the dielectric boundary experienced by the optical mode. The coupling strength is given by [17, 50, 69]

$$g_{mb} = -\frac{\omega_c}{2}\frac{\oint(\mathbf{q}\cdot\hat{\mathbf{n}})(\Delta\varepsilon\mathbf{E}_{\parallel}^2 - \Delta\varepsilon^{-1}\mathbf{D}_{\perp}^2)dA}{\int\varepsilon|\mathbf{E}|^2dV} \tag{2.55}$$

where $\mathbf{q}$ is the displacement of the mechanical mode at a given point, $\hat{\mathbf{n}}$ is the outward

direction of the surface normal, $\Delta\varepsilon = \varepsilon_m - \varepsilon_{\text{air}}$, $\Delta\varepsilon^{-1} = \varepsilon_m^{-1} - \varepsilon_{\text{air}}^{-1}$, and ε_m is the permittivity of the mechanical resonator material (in our case, diamond). $\mathbf{E}_{\parallel}$ and $\mathbf{D}_{\perp}$ are the parallel electric and perpendicular displacement fields to the resonator surface. The integral in the numerator is over the surface of the mechanical resonator, while the integral in the denominator is over the mechanical resonator volume and the surrounding air.

Photoelastic optomechanical coupling

The photoelastic contribution is caused by changes in the refractive index of the mechanical resonator material due to strain induced by the mechanical motion, characterized by the photoelastic tensor of the material. For our diamond OMCs, which are oriented along the 110 crystal axis, this coupling is given by (as in [17] but repeated here for clarity and accessibility)

$$g_{pe} = -\frac{\omega_c \epsilon_0 n^4}{2} \frac{\int \begin{bmatrix} E_x^* & E_y^* & E_z^* \end{bmatrix} \begin{bmatrix} pS_{xx} & pS_{xy} & pS_{xz} \\ pS_{xy} & pS_{yy} & pS_{yz} \\ pS_{xz} & pS_{yz} & pS_{zz} \end{bmatrix} \begin{bmatrix} E_x \\ E_y \\ E_z \end{bmatrix} dV}{\int \varepsilon |\mathbf{E}|^2 dV} \tag{2.56}$$

where

$$\begin{bmatrix} pS_{xx} \\ pS_{yy} \\ pS_{zz} \\ pS_{yz} \\ pS_{xz} \\ pS_{xy} \end{bmatrix} = \begin{bmatrix} \tilde{p_{11}} & \tilde{p_{12}} & \tilde{p_{13}} & 0 & 0 & \tilde{p_{16}} \\ \tilde{p_{12}} & \tilde{p_{22}} & \tilde{p_{23}} & 0 & 0 & \tilde{p_{26}} \\ \tilde{p_{13}} & \tilde{p_{23}} & \tilde{p_{33}} & 0 & 0 & 0 \\ 0 & 0 & 0 & \tilde{p_{44}} & 0 & 0 \\ 0 & 0 & 0 & 0 & \tilde{p_{55}} & 0 \\ \tilde{p_{16}} & \tilde{p_{26}} & 0 & 0 & 0 & \tilde{p_{66}} \end{bmatrix} \begin{bmatrix} S_{xx} \\ S_{yy} \\ S_{zz} \\ 2S_{yz} \\ 2S_{xz} \\ 2S_{xy} \end{bmatrix} \tag{2.57}$$

with S_{ij} components of the strain tensor in the rotated frame of interest (x along 110) and the components of the rotated photoelastic tensor:

$$\tilde{p_{11}} = \tilde{p_{22}} = \frac{1}{4}(p_{11}(3 + \cos(4\theta)) + (p_{12} + 2p_{44})(1 - \cos(4\theta)) \tag{2.58}$$

$$\tilde{p_{33}} = p_{11} \tag{2.59}$$

$$\tilde{p_{12}} = \frac{1}{4}(p_{12}(3 + \cos(4\theta)) + (p_{11} - 2p_{44})(1 - \cos(4\theta)) \tag{2.60}$$

$$\tilde{p_{13}} = \tilde{p_{23}} = p_{12} \tag{2.61}$$

$$\tilde{p_{44}} = \tilde{p_{55}} = p_{44} \tag{2.62}$$

$$\tilde{p_{66}} = \frac{1}{4}(2p_{44}(1 + \cos(4\theta)) + (p_{11} - p_{12})(1 - \cos(4\theta)) \tag{2.63}$$

$$\tilde{p_{16}} = \frac{1}{4}\sin(4\theta)(2p_{44} + p_{12} - p_{11}) \tag{2.64}$$

$$\tilde{p_{26}} = \frac{1}{4}\sin(4\theta)(p_{11} - p_{12} + 2p_{44}) \tag{2.65}$$

where $p_{11} = -0.25$, $p_{12} = 0.043$, and $p_{44} = -0.172$ are the photoelastic coefficients of diamond [17, 70].

Chapter 3

Strain coupling to silicon vacancy centers in diamond

3.1 Introduction

In this chapter we are going to gather some calculations for strain coupling to the negatively-charged SiV in diamond focusing on reconciling the notation in [54] and [59] and trying to find an exact solution for the spin-strain coupling before estimating the zero-point coupling to our OMCs. The SiV [60] has an orbital ground (g) state and excited state (u) separated by ≈ 737 nm, where g and u designate the parity of the states (g = even, u = odd) upon inversion. Both the ground state and the excited state are orbital doublets, the degeneracy of which is lifted by spin-orbit coupling of $\lambda_{SO,g} \approx 46$ GHz and $\lambda_{SO,e} \approx 255$ GHz respectively. The SiV also hosts an S = 1/2 spin. Like with the NV, we can also divide the 4 possible orientations of the SiV into two groups. Assuming the OMC is along the 110 axis, the two groups are with SiV axis parallel or perpendicular to the OMC length (when projected into the plane of the OMC).

3.2 Spin-orbit coupling in the SiV

The fine structure of the SiV in both the ground and excited states consists of e_x and e_y states (dropping the g and u subscripts that [59] uses to differentiate the ground and excited states), analogous to the NV center's excited state (see [54] for the definitions), which are mixed by the spin-orbit coupling Hamiltonian $H_{SO} = -\lambda_{SO}(L_z \otimes S_z)$ (the transverse terms only couple to far off A-symmetry states, so we can ignore them). For both the ground and excited state, in the $\{|e_x \downarrow\rangle, |e_x \uparrow\rangle |e_y \downarrow\rangle, |e_y \uparrow\rangle\}$ basis and with the appropriate λ_{SO}, we have

$$H_{SO} = -\lambda_{SO} \begin{pmatrix} 0 & -i \\ i & 0 \end{pmatrix} \otimes \begin{pmatrix} -1 & 0 \\ 0 & 1 \end{pmatrix} = \begin{pmatrix} 0 & 0 & -i\lambda_{SO}/2 & 0 \\ 0 & 0 & 0 & i\lambda_{SO}/2 \\ i\lambda_{SO}/2 & 0 & 0 & 0 \\ 0 & -i\lambda_{SO}/2 & 0 & 0 \end{pmatrix} \quad (3.1)$$

Note that this has eigenstates $\{|e_- \downarrow\rangle, |e_+ \uparrow\rangle, |e_+ \downarrow\rangle, |e_- \uparrow\rangle\}$ with eigenvalues $\{-\lambda_{SO}/2, -\lambda_{SO}/2, \lambda_{SO}/2, \lambda_{SO}/2\}$, where $e_\pm = \mp\frac{1}{\sqrt{2}}(e_x \pm i e_y)$. We will use this basis later for working out the spin-strain coupling.

3.3 Orbital-strain coupling

The orbital-strain coupling between the e_x and e_y states (in both the ground state and excited state) ends up having the same form as for the e_x and e_y states of the NV excited state, where we take the SiV-axis to be the z-axis and the projection of one of the carbon-vacancy bonds as the x-axis. In the notation of [54] following [71] for strain

interacting with C_{3v} and D_{3d}-symmetric defects, this interaction is

$$H_{\text{strain}} = [\lambda_{A_1}\epsilon_{zz} + \lambda_{A_1'}(\epsilon_{xx}+\epsilon_{yy})](|e_x\rangle\langle e_x| + |e_y\rangle\langle e_y|) \tag{3.2}$$

$$+ [\lambda_E(\epsilon_{yy}-\epsilon_{xx}) + \lambda_{E'}(\epsilon_{xz}+\epsilon_{zx})](|e_x\rangle\langle e_x| - |e_y\rangle\langle e_y|) \tag{3.3}$$

$$+ [\lambda_E(\epsilon_{xy}+\epsilon_{xy}) + \lambda_{E'}(\epsilon_{yz}+\epsilon_{zy})](|e_x\rangle\langle e_y| + |e_y\rangle\langle e_x|) \tag{3.4}$$

Now, in [59]'s notation

$$H_{\text{strain}} = [t_\parallel\epsilon_{zz} + t_\perp(\epsilon_{xx}+\epsilon_{yy})](|e_x\rangle\langle e_x| + |e_y\rangle\langle e_y|) \tag{3.5}$$

$$+ [-d(\epsilon_{yy}-\epsilon_{xx}) + f\epsilon_{zx}](|e_x\rangle\langle e_x| - |e_y\rangle\langle e_y|) \tag{3.6}$$

$$+ [-2d\epsilon_{xy} + f\epsilon_{yz}](|e_x\rangle\langle e_y| + |e_y\rangle\langle e_x|) \tag{3.7}$$

Some quick notes: for the ϵ_{xz} and ϵ_{yz} terms, instead of using e.g. $(\epsilon_{xz}+\epsilon_{zx})$, [59] combines this into one term since the strain tensor is symmetric, and absorbs the factor of 2 into f. Also, [59] has the sign of the $|e_x\rangle\langle e_x| - |e_y\rangle\langle e_y|$ term switched, making it impossible to equate these constants with those in [54]. This doesn't actually change the result, but does affect whether the result is invariant under $2\pi/3$ rotations (which it should be since the x-axis definition is arbitrary).

$$\lambda_{A_1} = t_\parallel \tag{3.8}$$

$$\lambda_{A_1'} = t_\perp \tag{3.9}$$

$$\lambda_E = -d \tag{3.10}$$

$$\lambda_{E'} = \frac{f}{2} \tag{3.11}$$

[59] then lumps together the strain terms into ϵ_{A_1}, $\epsilon_{E_{gx}}$, and $\epsilon_{E_{gy}}$ (this is a bit confusing because these are, strictly speaking, energies, not strain) whereas [54] uses V_{A_1}, V_{E_1}, and

V_{E_2}, where the subscripts just denote the symmetry of the term. So we have

$$H_{\text{strain}} = V_{A_1}(|e_x\rangle\langle e_x| + |e_y\rangle\langle e_y|) \tag{3.12}$$

$$+ V_{E_1}(|e_x\rangle\langle e_x| - |e_y\rangle\langle e_y|) \tag{3.13}$$

$$+ V_{E_2}(|e_x\rangle\langle e_y| + |e_y\rangle\langle e_x|) \tag{3.14}$$

where

$$V_{A_1} = \lambda_{A_1}\epsilon_{zz} + \lambda_{A_1'}(\epsilon_{xx} + \epsilon_{yy}) \tag{3.15}$$

$$V_{E_1} = \lambda_E(\epsilon_{yy} - \epsilon_{xx}) + \lambda_{E'}(\epsilon_{xz} + \epsilon_{zx}) \tag{3.16}$$

$$V_{E_2} = \lambda_E(\epsilon_{xy} + \epsilon_{xy}) + \lambda_{E'}(\epsilon_{yz} + \epsilon_{zy}) \tag{3.17}$$

Adding in the spin degree-of-freedom via tensor product with $\mathbb{I}_2$ (since the strain does not affect the spin) in the $\{|e_x\downarrow\rangle,|e_x\uparrow\rangle\,|e_y\downarrow\rangle,|e_y\uparrow\rangle\}$ basis we have

$$H_{\text{strain}} = \begin{pmatrix} V_{A_1}+V_{E_1} & V_{E_2} \\ V_{E_2} & V_{A_1}-V_{E_1} \end{pmatrix} \otimes \mathbb{I}_2 = \begin{pmatrix} V_{A_1}+V_{E_1} & 0 & V_{E_2} & 0 \\ 0 & V_{A_1}+V_{E_1} & 0 & V_{E_2} \\ V_{E_2} & 0 & V_{A_1}-V_{E_1} & 0 \\ 0 & V_{E_2} & 0 & V_{A_1}-V_{E_1} \end{pmatrix} \tag{3.18}$$

Adding the spin-orbit Hamiltonian to this, we get the total Hamiltonian for the $\{|e_x\downarrow\rangle,|e_x\uparrow\rangle\,|e_y\downarrow\rangle,|e_y\uparrow\rangle\}$ states in the presence of strain

$$H_{\text{orbit}} = \begin{pmatrix} V_{A_1}+V_{E_1} & 0 & V_{E_2}-i\lambda_{SO}/2 & 0 \\ 0 & V_{A_1}+V_{E_1} & 0 & V_{E_2}+i\lambda_{SO}/2 \\ V_{E_2}+i\lambda_{SO}/2 & 0 & V_{A_1}-V_{E_1} & 0 \\ 0 & V_{E_2}-i\lambda_{SO}/2 & 0 & V_{A_1}-V_{E_1} \end{pmatrix} \tag{3.19}$$

Diagonalizing this, we find eigenenergies

$$E_{\pm} = V_{A_1} \pm \frac{1}{2}\sqrt{\lambda_{SO}+4(V_{E_1}^2+V_{E_2}^2)} \tag{3.20}$$

Thus, the strain interaction manifests as a change in the ZPL due to A_1 strain of $\Delta = V_{A_1,e}-V_{A_1,g} = (t_{\parallel,e}-t_{\parallel,g})\epsilon_{zz}+(t_{\perp,e}-t_{\perp,g})(\epsilon_{xx}+\epsilon_{yy})$, where e and g indicate the different constants for the ground and excited state. [59] measures $(t_{\parallel,e}-t_{\parallel,g}) = -1.7$ PHz/strain and $(t_{\perp,e}-t_{\perp,g}) = 0.078$ PHz/strain. We can see that the E-strain splits the orbital branches of both the ground and excited state, but this effect is washed out until the V_{E_1} and V_{E_2} terms are of order the spin-orbit splitting, which requires $\approx 1000\times$ the zero-point amplitude.

3.4 SiV spin-strain coupling

Transforming the above Hamiltonian into the spin-orbit eigenbasis $\{|e_{-\downarrow}\rangle, |e_{+\uparrow}\rangle, |e_{+\downarrow}\rangle, e_{-\uparrow}\rangle\}$ and ignoring the constant V_{A_1} along the diagonal, we have

$$H_{\text{orbit}} = \begin{pmatrix} -\lambda_{SO}/2 & 0 & -(V_{E_1} + iV_{E_2}) & 0 \\ 0 & -\lambda_{SO}/2 & 0 & -V_{E_1} + iV_{E_2} \\ -V_{E_1} + iV_{E_2} & 0 & \lambda_{SO}/2 & 0 \\ 0 & -(V_{E_1} + iV_{E_2}) & 0 & \lambda_{SO}/2 \end{pmatrix} \tag{3.21}$$

Now we apply a magnetic field with components parallel (B_z) and transverse (B_x) to the SiV axis. Including the Zeeman interaction of both the spin and orbital states with this magnetic field, the total Hamiltonian in the $\{|e_{-\downarrow}\rangle, |e_{+\uparrow}\rangle, |e_{+\downarrow}\rangle, e_{-\uparrow}\rangle\}$ basis is

$$H_{\text{tot}} = \begin{pmatrix} -\frac{\lambda_{SO}}{2} - (\gamma_L + \gamma_s)B_z & 0 & -(V_{E_1} + iV_{E_2}) & \gamma_s B_x \\ 0 & -\frac{\lambda_{SO}}{2} + (\gamma_L + \gamma_s)B_z & \gamma_s B_x & -V_{E_1} + iV_{E_2} \\ -V_{E_1} + iV_{E_2} & \gamma_s B_x & \frac{\lambda_{SO}}{2} + (\gamma_L - \gamma_s)B_z & 0 \\ \gamma_s B_x & -(V_{E_1} + iV_{E_2}) & 0 & \frac{\lambda_{SO}}{2} + (\gamma_S - \gamma_L)B_z \end{pmatrix} \tag{3.22}$$

where $\gamma_s = \mu_B/h = 14$ GHz/T and $\gamma_L = q\mu_B/h$, with $q = 0.1$ as an orbital angular momentum quenching factor. Note also that I have absorbed the factor of 1/2 from the spin into the spin gyromagnetic ratio, which is nominally $2\mu_B/h$. Furthermore, we have V_{E_2} terms, which [59] ignores (we can ignore them too, but we'll leave them in). Now, looking at this Hamiltonian, we don't see any coupling between what we eventually want to use as our qubit basis $\{|e_{-\downarrow}\rangle, |e_{+\uparrow}\rangle\}$ but that the off-axis magnetic field component B_x does couple states of different spin, while the strain terms couple states of

different orbital character. It is reasonable to guess that the combination of the two will lead to an effective coupling between our qubit states. To determine this coupling, we can project our Hamiltonian onto the qubit subspace using a Schrieffer-Wolff transform $\tilde{H} = e^{\alpha A} H_{\text{tot}} e^{-\alpha A} \approx H_{\text{tot}} + \alpha[A, H_{\text{tot}}]$ that makes the Hamiltonian block-diagonal to first order in the small, arbitrary parameter α, with A a to-be-determined matrix. To find A, split H_{tot} into block diagonal H_E and block off-diagonal $H_c = \alpha V_c$ components. Then $\tilde{H} = H_E + \alpha V_c + \alpha[A, H_E] + \alpha^2[A, V_c]$. To first order in α, we want to eliminate the block off-diagonal components, which gives us the condition $V_c = [H_E, A]$. Solving this gives us the requisite A

$$A = -\frac{1}{\alpha}\begin{pmatrix} 0 & 0 & -\frac{V_{E_1}+iV_{E_2}}{\lambda_{SO}+2\gamma_L B_z} & \frac{\gamma_s B_x}{\lambda_{SO}+2\gamma_s B_z} \\ 0 & 0 & \frac{\gamma_s B_x}{\lambda_{SO}-2\gamma_s B_z} & \frac{-V_{E_1}+iV_{E_2}}{\lambda_{SO}-2\gamma_L B_z} \\ \frac{V_{E_1}-iV_{E_2}}{\lambda_{SO}+2\gamma_L B_z} & -\frac{\gamma_s B_x}{\lambda_{SO}-2\gamma_s B_z} & 0 & 0 \\ -\frac{\gamma_s B_x}{\lambda_{SO}+2\gamma_s B_z} & \frac{V_{E_1}+iV_{E_2}}{\lambda_{SO}-2\gamma_L B_z} & 0 & 0 \end{pmatrix} \tag{3.23}$$

Using this A, we find the projected Hamiltonian in the $\{|e_{-\downarrow}\rangle, |e_{+\uparrow}\rangle\}$ basis, ignoring the constant $-\lambda_{SO}/2$ on the diagonal

$$\tilde{H}_{\text{tot}} = \begin{pmatrix} -(\gamma_L+\gamma_s)B_z - \frac{2(V_{E_1}^2+V_{E_2}^2)}{\lambda_{SO}+2\gamma_L B_z} - \frac{2\gamma_s^2 B_x^2}{\lambda_{SO}+2\gamma_s B_z} & \frac{4\gamma_s B_x \lambda_{SO}(V_{E_1}+iV_{E_2})(\lambda_{SO}^2-2B_z^2(\gamma_L^2+\gamma_s^2))}{(\lambda_{SO}-2\gamma_L B_z)(\lambda_{SO}-2\gamma_s B_z)(\lambda_{SO}+2\gamma_L B_z)(\lambda_{SO}+2\gamma_s B_z)} \\ \frac{4\gamma_s B_x \lambda_{SO}(V_{E_1}-iV_{E_2})(\lambda_{SO}^2-2B_z^2(\gamma_L^2+\gamma_s^2))}{(\lambda_{SO}-2\gamma_L B_z)(\lambda_{SO}-2\gamma_s B_z)(\lambda_{SO}+2\gamma_L B_z)(\lambda_{SO}+2\gamma_s B_z)} & (\gamma_L+\gamma_s)B_z - \frac{2(V_{E_1}^2+V_{E_2}^2)}{\lambda_{SO}-2\gamma_L B_z} - \frac{2\gamma_s^2 B_x^2}{\lambda_{SO}-2\gamma_s B_z} \end{pmatrix} \tag{3.24}$$

The strain term on the diagonal is of order kHz, while everything else is GHz, so we can safely ignore it and estimate the energy difference between our qubit states to be

$$\Delta E = 2(\gamma_L+\gamma_s)B_z - \frac{8\gamma_s^3 B_x^2 B_z}{\lambda_{SO}^2 - 4\gamma_s^2 B_z^2} \tag{3.25}$$

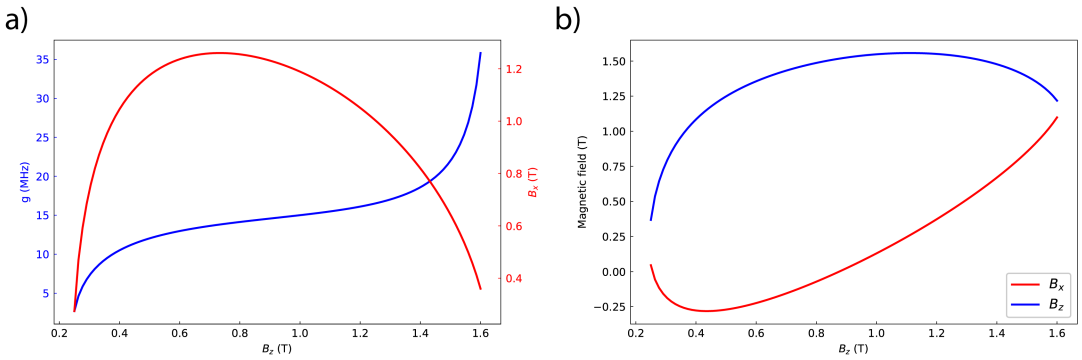

Figure 3.1: a) g_{spin} and B_x as a function of B_z for constant ΔE. b) B_x and B_z in the lab frame as a function of B_z in the SiV frame for constant ΔE.

and the magnitude of the coupling between the states to be

$$g_{\text{spin}} = \frac{4\gamma_s B_x \lambda_{SO} \sqrt{V_{E_1}^2 + V_{E_2}^2}(\lambda_{SO}^2 - 2B_z^2(\gamma_L^2 + \gamma_s^2))}{(\lambda_{SO} - 2\gamma_L B_z)(\lambda_{SO} - 2\gamma_s B_z)(\lambda_{SO} + 2\gamma_L B_z)(\lambda_{SO} + 2\gamma_s B_z)} \tag{3.26}$$

Now, [59] measured $d = 1.3$ PHz/strain and $f = -1.7$ PHz/strain for the ground state, which we can plug in along with our simulation of the strain tensor to determine the values of $V_{E_{1,2}}$. Furthermore, if we define $B_z = B\cos\theta$ and $B_x = B\sin\theta$ as the projections of the magnetic field along the SiV z and x axes, with $\theta = 54.736$ degrees the angle between the SiV z axis and 001, we can determine the magnetic field magnitude required to match the qubit energy to our mechanical resonator frequency. Now, [59] seems to just assume $\lambda_{SO} \gg \gamma_s B_z, \gamma_s B_x$ and simplifies the coupling term to $g_{\text{spin}} \approx (2\gamma_s B_x/\lambda_{SO})V_{E_1}$. If we make this simplification, we end up with twice this estimate, $g_{\text{spin}} \approx (4\gamma_s B_x/\lambda_{SO})V_{E_1}$, and I'm not sure where the disparity arises.

3.4.1 Optimizing strain coupling with magnetic field

g_{spin} is dependent on B_x and B_z while B_x and B_z are related by the energy splitting between the spin states, which we set to be the mechanical frequency. Solving for B_x,

we find

$$B_x = \sqrt{\frac{(f_m - 2(\gamma_l + \gamma_s)B_z)(4\gamma_s^2 B_z^2 - \lambda_{SO}^2)}{8\gamma_s^3 B_z}} \tag{3.27}$$

Note that this relation requires $f_m/2(\gamma_l + \gamma_s) < B_z < \lambda_{SO}/2\gamma_s$, which for $f_m = 7.5$ GHz, corresponds to a range of $\approx 0.24 - 1.64$ T. Figure 3.1a shows how g_{spin} and B_x depend on B_z for this case. We can then determine what the required magnetic field in the lab frame would be to achieve the SiV-frame fields in figure 3.1a by taking

$$B_{x,\text{lab}} = B_z \sin\theta - B_x \cos\theta \tag{3.28}$$

$$B_{z,\text{lab}} = B_x \sin\theta + B_z \cos\theta \tag{3.29}$$

Chapter 4

Diamond optomechanical crystal design and fabrication

4.1 Device geometry

OMC

As discussed in chapter 1, our OMC geometry (based off the design described in [50]) fundamentally consists of a rectangular cross-section nanobeam, typically along the 110 crystal direction, into which elliptical holes of different sizes are etched, defining a "defect cell" at the center of the OMC which hosts optical and mechanical modes, "mirror cells" at either end of the OMC which have optical and mechanical quasi-bandgaps around the defect cell mode frequencies due to the periodic nature of the dielectric in those regions and which therefore act as a Bragg mirror, and cells that adiabatically transition the cell geometry between the defect cell and the mirror cells. In practice, we first define our geometry by parameterizing the mirror cell hole shape with h_x and h_y (the radii in the x and y directions, with x being defined as the direction along the beam length and y across the beam width) in addition to the mirror cell lattice constant a_{mir}, which is the distance between adjacent mirror cell holes. We then define the defect cell in terms of the mirror cell using four parameters: d, χ, ξ, and η. The defect cell lattice

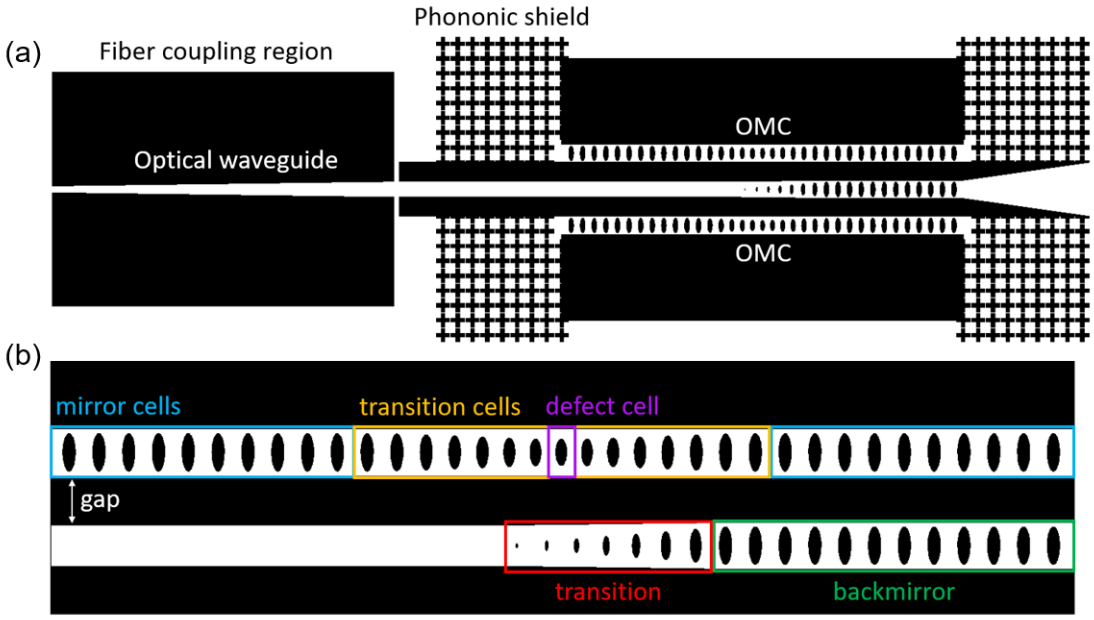

Figure 4.1: a) An overview of a typical pair of OMC devices on either side of a central optical waveguide, which has a tapered coupling region on the left and an optical backmirror on the right. The OMC clamping points are surrounded by a cross pattern phononic shield. b) A zoom-in of the OMC and waveguide.

constant is given by $a_0 = ab_0$, where $b_0 = 1 - d$ while the defect cell hole dimensions are $h_{x,0} = h_x\sqrt{s_0/r_0}$ and $h_{y,0} = h_y\sqrt{s_0 r_0}$, where $s_0 = 1 - \chi(1 - b_0)$ and $r_0 = b_0^{\xi}$. We then define a function that describes the transition from defect cell to mirror cell over N intermediate cells. The distance between hole i and $i + 1$, where $i = 0$ is the defect hole, is $a_i = b_i a_m ir$, with $b_i = 1 - d(2j^3 - 3j^2 + 1)$ and $j = (2g)^{\eta}/2$ for $g = i/N \leq 0.5$ or $j = 1 - (2(1 - g))^{\eta}/2$ for $g = i/N > 0.5$. Furthermore, $h_{x,i} = (\sqrt{s_i/r_i})h_x$ and $h_{y,i} = (\sqrt{s_i r_i})h_y$, where $s_i = 1 - \chi(1 - b_i)$ and $r_i = b_i^{\xi}$. After this transition are N_{mir} mirror cells. Note that $i = N$ describes a mirror cell, such that there are actually $N_{mir}+1$ mirror cells on either side of the OMC. Together with the OMC width w and thickness t, we fully describe the OMC geometry.

Waveguide

The waveguide for coupling light into the OMC consists of two main parts: the fiber coupling region and the OMC coupling region. The fiber coupling region consists of a waveguide that tapers from an initial width $w_{wg,i}$ to a final width $w_{wg,f}$ over a distance l_{wg}. For coupling with tapered optical fibers, the waveguide is clamped at the narrow end while for lensed fiber coupling it is unclamped to allow for optical access to the waveguide endface. For tapered fiber coupling, the waveguide tapers in the opposite direction of the fiber, allowing for adiabatic transfer of light over a region where the optical mode goes from primarily confined in the fiber (wide fiber/narrow waveguide) to primarily confined in the waveguide (narrow fiber/wide waveguide [72]. Longer tapering regions allow for higher coupling efficiencies but are difficult to fabricate in non-high stress materials and require significant room on a chip, so we compromise with $l_{wg} = 15\mu$m which is robust after fabrication but still gives a tapering angle of $< 1^\circ$ for typical $w_{wg,i} = 300$ nm and $w_{wg,f} = 700$ nm, which is much less than typical fiber tapering angles of $\approx 5^\circ$. For the lensed fiber region, $w_{wg,i}$ is chosen to be 200 nm to mode match the waveguide to the incoming gaussian beam of width 2.5 μm from the lensed fiber. The simulations for these parameters are discussed in the next section.

The OMC coupling region is described by $N_{mir,wg}$, which is the number of mirror cells at the end of the waveguide, N_{wg}, which is the number of cells over which the hole size and beam width are linearly tapered up to the full mirror cell (to minimize scattering losses at the mirror), and the gap between the waveguide and the OMC, which determines the coupling strength between the waveguide and the OMC κ_e.

Finally, for both the tapered and lensed fiber variations, the waveguide is clamped to the bulk after the tapering region by wide tethers and after the backmirror for stability. The clamping geometry after the backmirror differs between the devices presented in

chapters 5 and 6 but presently we employ the geometry shown in figure 4.1, which clamps the waveguide outside of the phononic shield with a flared structure that provides added structural stability to the waveguide.

Phononic shield

The phononic shield consists of a 2D array of cross-shaped holes in the diamond surrounding the OMC clamping points and is parameterized by lattice spacing a_{shield} of the crosses in addition to the cross arm width w_{cross} and cross height h_{cross} which are defined as fractions of a_{shield}. In [1] it was reported that having 8 layers of shielding between the OMC clamping point and the bulk was sufficient to provide mechanical isolation of the OMC.

Rectangular versus triangular cross-section

We choose to fabricate our diamond OMCs with a rectangular cross-section (as opposed to a triangular cross-section as in [17]) in keeping with the design used in the majority of the optomechanical crystal community. A rectangular cross-section is compatible with our top-down diamond-on-insulator fabrication method and does not require the specialized angled etching used in fabrication of triangular cross-sections. The triangular cross-section devices do have advantages, however. The angled etching techniques [73, 74] used to form them allows for device fabrication out of bulk diamond, doing away with the requirement for diamond membranes. Also, the triangular geometry allows for the formation of a full phononic bandgap in the mirror regions of the OMC, which is not possible for rectangular cross-sections. However, these devices are highly sensitive to fabrication imperfections, particularly the etch angle and the angled etching technique does not allow for creation of more robust phononic shields around the device to mitigate these effects. In terms of strain coupling to defects, both geometries generate comparable

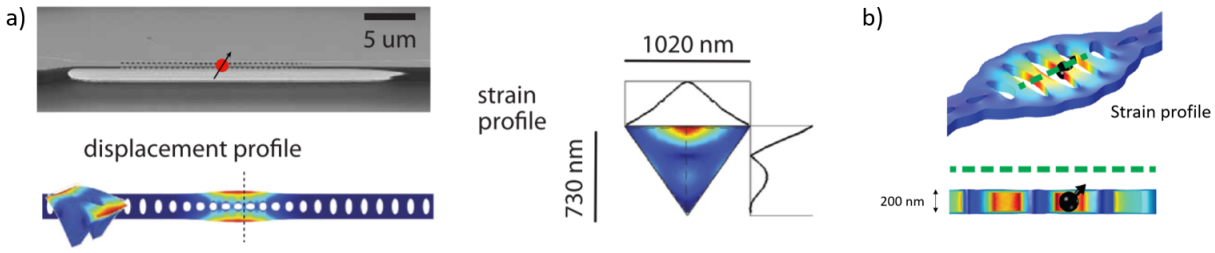

Figure 4.2: a) Displacement and strain profiles for the flapping mode of a triangular cross-section diamond OMC from [59]. b) Strain profile of the breathing mode of a rectangular cross-section diamond OMC from [18].

strain. However, the flapping mode of triangular cross-section OMCs generates a strain profile that is highest at the top surface of the device, as opposed to the z-symmetric strain profile of rectangular cross-section OMCs.

4.2 Simulation

4.2.1 OMC optics

Simulation of the OMC optical mode is accomplished using an eigenfrequency study in COMSOL using the "electromagnetic waves, frequency domain" package. The model is generated with a MATLAB script that interfaces with COMSOL and defines the OMC geometry and material parameters and surrounds the OMC with an air box, which in turn is surrounded by a perfectly matched layer (PML) that serves to approximate infinite vacuum, ensuring that optical power that exits the air box is not reflected back into the simulation volume, allowing for accurate determination of quality factors later on. The model is then reduced to 1/8 of the volume by taking advantage of the known symmetries of the optical mode we are interested in and applying symmetry conditions along the symmetry planes of the model. These consist of the perfect electric conductor

condition along the xz[1] and yz planes and the perfect magnetic conductor condition across the xy plane. The mesh of the model must be set rather fine for these simulations in order to accurately pixelate the OMC geometry and prevent artificial scattering losses from dominating the simulated optical loss. Due to the large size and fine mesh of these simulations, they are very memory and time-intensive, so applying symmetries is critical for running the simulation under memory and time constraints. Running the simulation gives a series of eigenmodes and their corresponding complex frequencies emw.freq (which are complex due to scattering loss in the model). The quality factor of a given mode is simply Re(emw.freq)/Im(emw.freq) and is accessible via the COMSOL parameter emw.Qfactor. This quality factor is equal to the standard definition of quality factor as described in equation 2.1 (energy stored in the system divided by power lost per cycle) which in the case of our model is

$$Q_o = \frac{\omega U_{EM}}{\int_{S_{air}} \overrightarrow{P} \cdot \overrightarrow{n}} \tag{4.1}$$

where ω = emw.omega is the angular frequency of the mode, $U_{EM} = 2$(emw.intWe) is the total electromagnetic energy in the air box and OMC, and $\int_{S_{air}} \overrightarrow{P} \cdot \overrightarrow{n}$ is the power lost through the air box integrated over the whole surface and the power flow along the different axes is emw.Poavx(y,z). In practice it is generally easier to access the COMSOL quality factor result, as the calculation above requires the addition of a surface just within the air box-PML interface to integrate over since that interface can give unwanted distortions. The fundamental TE mode of interest will almost always have the highest quality factor of the simulated modes (if it is with the frequency range of the modes returned by COMSOL) and is thus easy to identify. If the fundamental TE mode

[1]Our coordinate system has x along the length of the OMC and z in the direction of the OMC thickness

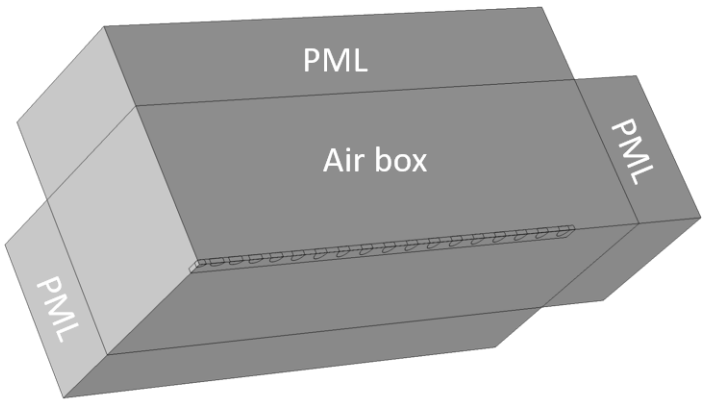

Figure 4.3: A COMSOL optical simulation model

isn't found, we must expand the number of eigenmodes that COMSOL finds or change the center frequency of the search. The quality factor extracted from this simulation describes the scattering into vacuum, mostly in the $\pm z$ directions, that ultimately limits the optical quality factor in the absence of other loss mechanisms. In general, this value is much higher than measured values and can be several million for optimized geometries.

Waveguide coupling

To simulate the coupling between an OMC and the optical waveguide we need to add the waveguide geometry to our model, which reduces the symmetry of the model, allowing us to only apply a symmetry in the xy plane. Otherwise, the model is similar to that described above, but the analysis must be done more manually, as the figure of merit that we are interested in (the external quality factor) is not a standard result that COMSOL calculates. We calculate this by assuming that the vast majority of the power that exits the air box through the surface normal to the left side of the OMC and waveguide (the opposite side from the mirror-terminated portion of the waveguide) is due to coupling to and propagation in the waveguide. We confirm this by measuring the

power through this surface in the absence of a waveguide and find it to be negligible. We can also check the power lost through the surface at the mirror-terminated end of the waveguide and find it to be negligible as well. In this case the external quality factor is

$$Q_e = \frac{\omega U_{EM}}{\int P_x} \tag{4.2}$$

where P_x = emw.Poavx is integrated across the surface described above. Intuitively, the farther the waveguide is from the OMC (the gap distance shown in figure 4.1), the smaller the overlap between the OMC mode and the waveguide mode and the smaller the power emitted from the end of the waveguide. The waveguide geometry should be carefully ensured to be the same as will be used in eventual devices, as the positions of the holes at the end of the waveguide relative to the OMC pattern will effect the mode overlap. Because diamond is a small-index material, the OMC mode is not as well-contained in the diamond as it would be in silicon, requiring a larger OMC-waveguide gap to achieve a given coupling rate. After simulating a range of gaps we make a plot of $\kappa_e = f/Q_e$ vs the gap distance. We can select a range of gaps that give κ_e close to or less than the κ_i that we typically measure, on the order of 2 GHz ($Q_i \approx 10^5$), in order to achieve close to critical coupling ($\kappa_e = \kappa_i$) in fabricated devices without overcoupling the optical mode ($\kappa_e > \kappa_i$).

Scattering into the bulk

A device parameter that is difficult but important to control in our devices is the gap underneath the OMC between the OMC and the bulk material, normally silicon but potentially diamond. This simulation is very similar to the regular optical simulation but we replace one of the PML boxes above or below the OMC with a box of the bulk material of interest. The presence of this material reduces the symmetry of the model

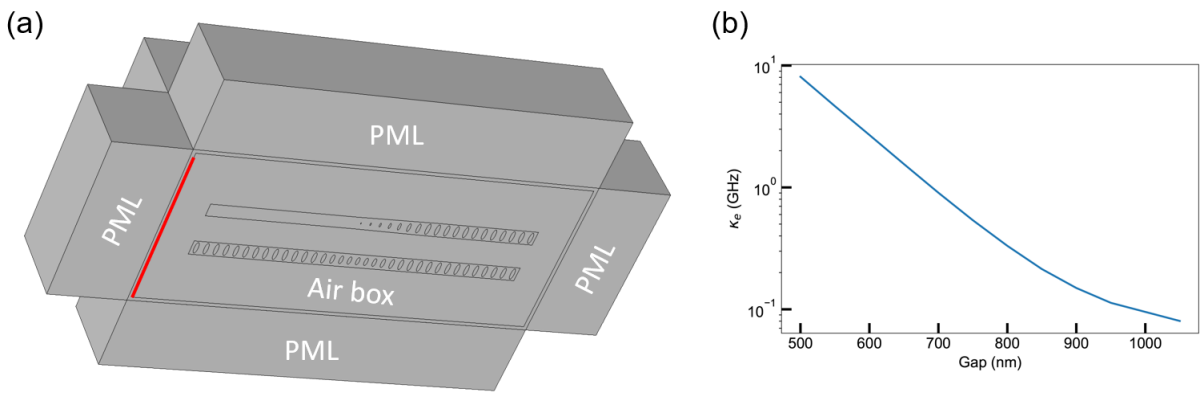

Figure 4.4: a) A COMSOL optical simulation model for OMC-waveguide coupling. The bottom edge of the surface that the exiting optical power is integrated over is highlighted in red. An example plot of κ_e vs OMC-waveguide gap showing that κ_e decreases rapidly for increasing gap.

such that we must simulate a quadrant of the model instead of an octant. We then vary the distance between the bottom of the OMC and this bulk material and extract the quality factor and κ_i for the fundamental TE mode. Figure X shows a plot of κ_i vs the gap distance above bulk silicon for the Nov_2020_8GHz design, which has a scattering-limited simulated optical quality factor of $> 10^6$ ($\kappa_i < 200$ MHz). The simulated κ_i is much smaller than typically experimentally realized values for gaps greater than 1 μm, indicating that this gap distance is the minimum that we should have in our devices. Scattering losses increase when fabrication imperfections are taken into account, so this gap should be made as large as practically possible to minimize unwanted scattering into the bulk.

4.2.2 Fiber coupling

Tapered fiber coupling

To determine $w_{wg,i}$ and $w_{wg,f}$ for the tapered fiber coupling region of the waveguide, finite-difference time domain simulations were performed by the Safavi-Naeini group using

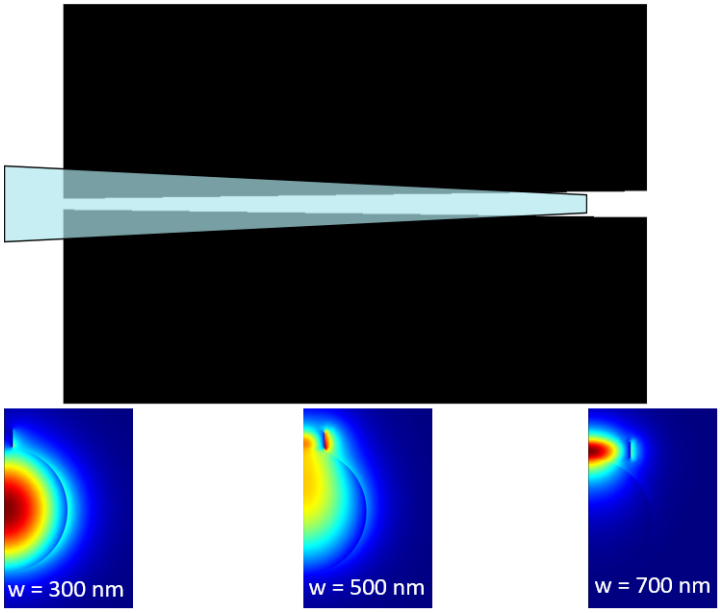

Figure 4.5: The tapered fiber coupling geometry, where a tapered optical fiber (blue) tapers down in width while the diamond optical waveguide tapers up in width. As can be seen by the Lumerical simulations underneath the geometry, the optical mode transitions from residing primarily in the fiber to primarily in the waveguide as the waveguide width increases relative to the fiber.

the simulation package Lumerical. The simulation consisted of a two-dimensional model of a 1.5 μm-wide optical fiber above a 200 nm-thick diamond waveguide, the width of which is varied. Figure 4.5 shows how the hybridized waveguide-fiber mode transitions from existing primarily within the fiber to primarily within the waveguide.

Lensed fiber coupling

To determine the optimal waveguide endface width for mode matching to the focused gaussian beam of a lensed fiber, we perform a 3D simulation in Lumerical in which a gaussian beam with the correct width (2.5μm in our case for a commercially-available fiber) is incident upon the narrow end of our tapered waveguide geometry. We then sweep $w_{wg,i}$ and monitor the transmission of the beam through a cross-section at the end of the waveguide. Figure X shows transmission T through the waveguide as a function

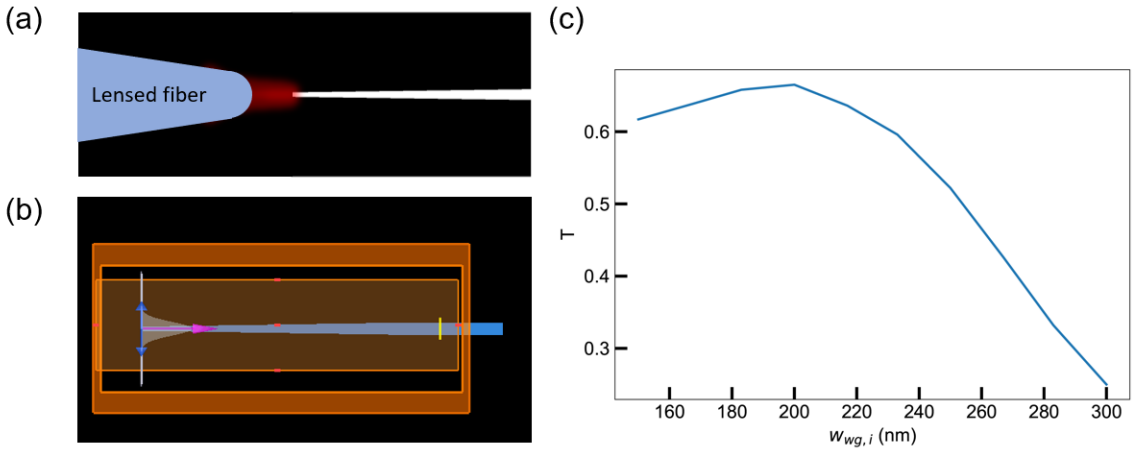

Figure 4.6: a) The lensed fiber coupling geometry (not to scale), in which a fiber with a polished lens on its endface emits light toward the coupling waveguide. b) The lensed fiber coupling simulation model in Lumerical. A gaussian waveform of 1550 nm light is incident on the left end of the waveguide and its transmission is measured through the yellow box at the right end of the waveguide. c) Transmission versus $w_{wg,i}$ for a 300 nm-thick waveguide and $w_{wg,f} = 700$ nm.

of $w_{wg,i}$ for a 300 nm-thick waveguide, where we see that the peak transmission is for $w_{wg,i} = 200$ nm.

4.2.3 Mechanics

Simulating the OMC mechanical mode in COMSOL is simpler than the optical mode, as it does not require an air box or PML [2]. Similar to the optical simulation, however, we can apply symmetry operations to the model and only have to simulate 1/8 of the geometry. We apply symmetry conditions across the xy, xz, and yz planes. We also set the displacement at the end of the OMC (after the mirror cells) to zero using a fixed condition in order to suppress uninteresting flexural modes. We can then find the mechanical eigenmodes that have the symmetry of the mechanical breathing mode

[2] A PML is required for simulating mechanical loss from the OMC in the case of simulating fabrication disorder or engineered leakage, but we typically do not do this and can assume that the simulated mechanical Q is infinite.

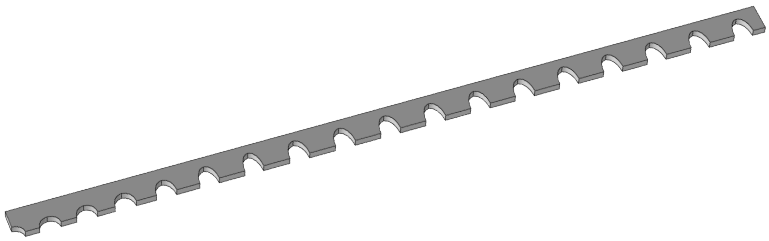

Figure 4.7: A mechanical model in COMSOL consisting of 1/8 of an OMC.

by performing an eigenfrequency study in the solid mechanics package. One can then manually search for the breathing mode among the calculated eigenmodes. However, usually the mechanics are simulated in the course of an optomechanical model that couples the optical and mechanical simulations and the breathing mode is easily picked out as it has the highest optomechanical coupling to the fundamental TE mode. This is discussed in the section describing simulation of optomechanical coupling below.

Strain

Once the breathing mode frequency is determined, we would like to determine the zero-point strain in the OMC that an SiV would experience. To do this, we perform a frequency domain simulation at the breathing mode frequency while applying a prescribed displacement in the y-direction that is of order the zero-point motion amplitude as given in equation 2.36. This displacement is not exactly the zero-point motion amplitude, however, as that is a normalized displacement over the entire mode shape, but serves as a guess for determining a displacement which gives a strain energy equal to $\hbar\omega_m/4$. We perform this simulation with the guess amplitude $y = x_{zpf}$ and then calculate a fractional energy difference

$$\Delta_E = \frac{\hbar\omega_m/4}{8U_\varepsilon} - 1 \tag{4.3}$$

where ω_m = solid.omega is the angular frequency of the mechanical mode and U_ε = solid.Ws_tot is the total strain energy in the model, which we multiply by 8 to determine the strain energy in a full OMC since we are only simulating an octant. If $abs(\Delta_E) > .01$, we recalculate $y_{new} = y_{old}(1+\Delta_E/2)$ and iterate until $abs(\Delta_E) < .01$, indicating less than a 1% difference between the simulated and theoretical strain energy. With this model, we then calculate the strain tensor in the OMC basis $\varepsilon_{\mathrm{OMC}}$ at a point of interest, typically at $x = a_0/2$, $y, z = 0$, where a_0 is the lattice constant of the defect cell. This point corresponds to a point in the high-strain region near the center of the OMC that is simultaneously well-separated from surfaces, as it is maximally distance from the top and bottom surfaces of the OMC as well as the nanobeam sidewalls. It is not the point of maximal strain (which is along the perimeter of the defect cell hole). We then rotate the strain tensor into the SiV basis for both SiV orientations (orientation 1: 111 and orientation 2:$\bar{1}11$) by applying the transformation $\varepsilon_{\mathrm{SiV}} = R_2(\theta_2)R_1(\theta_1)\varepsilon_{\mathrm{OMC}}R_1^T(\theta_1)R_2^T(\theta_2)$. For orientation 1, $R_1 = R_y$ with $\theta_1 = -54.736$ degrees, and $R_2 = R_z$ with $\theta_2 = 180$ degrees. For orientation 2, $R_1 = R_x$ with $\theta_1 = 54.736$ degrees, and $R_2 = R_z$ with $\theta_2 = 90$ degrees. With the strain tensor in the SiV bases, we can then calculate V_{E_1} and V_{E_2} as in equation 3.15 which are the strain susceptibilities that factor into the SiV spin-strain coupling strength given by equation 3.26.

Phononic shield

The phononic shield is simulated with an eigenfrequency study in the solid mechanics package using a model consisting of a unit cell of the phononic shield: an a_{shield} square,

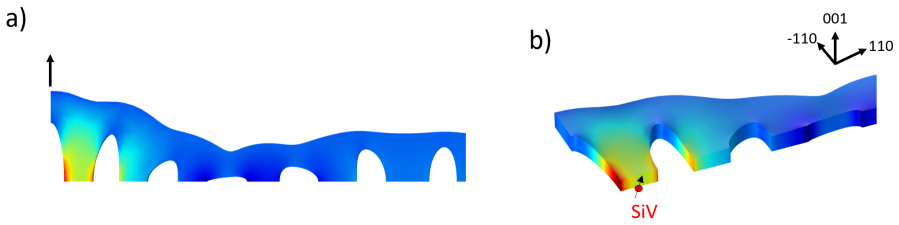

Figure 4.8: a) The direction of the edge displacement for the simulation. b) The point at which the strain tensor is evaluated.

t-thick block with a cross-shaped hole with arm width w and height h. We also take into account rounding of the right angles in the cross that occur during fabrication as in [1] and which fortuitously tend to actually give large bandgaps than perfect right angles. SEMs of fabricated devices have shown typical radii of curvature of ≈ 35 nm, but this should be continuously verified for different devices and fabrication processes. Floquet periodicity conditions are applied between the top/bottom and left/right edges of the model with k-vector $(k_x, k_y, 0)$ with $k_{x,y} = m_{x,y}\pi/a_{shield}$. We then sweep m_x and m_y to trace out a path in k-space shown in figure 4.9c, performing an eigenfrequency study for each $m_{x,y}$ pair to determine the first ten eigenmodes of the phononic shield cell (ten is usually enough to see the phononic bandgap). In practice, this takes three separate parametric sweeps in COMSOL. One keeping $m_y = 0$ and sweeping m_x from 0 to 1, one keeping $m_x = 1$ and sweeping m_y from 0 to 1, and then finally sweeping m_x and m_y from 1 to 0 simultaneously. The result is a bandstructure that will reveal a full mechanical bandgap around some frequency, as shown in figure 4.9c. The dimensions of the phononic shield cell can then be adjusted to change the center frequency and width of this bandgap to suit the frequency of the OMC mechanical mode.

4.2.4 Optomechanical coupling

The optomechanical simulation is achieved with a model in which we run both optical and mechanical simulations. The model is set up similarly to the regular optical

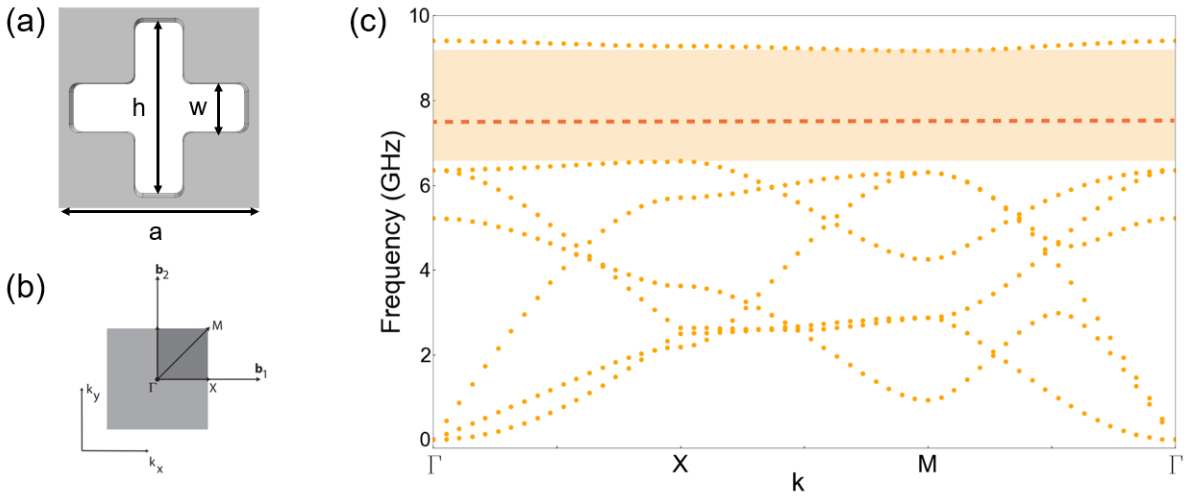

Figure 4.9: a) The geometry of the simulated phononic shield unit cell. b) A map in k-space of the simulated k-vectors. c) The resulting bandstructure generated from simulating the phononic shield over a range of k-vectors, showing a full bandgap (highlighted in orange) around the OMC breathing mode frequency (dark orange line).

simulation: an octant of the OMC surrounded by air box and PML, but we include both electromagnetic wave and solid mechanics physics and apply the mechanical symmetry operations to the diamond portion of the model. We also define three regions of integration for calculations with the simulated model: the diamond volume (intop1), the air box volume (intop2), and the diamond surface (intop3). We then run an optical eigenfrequency simulation at the previously-determined optical frequency of the OMC (with the solid mechanics physics turned off) and then a solid mechanics eigenfrequency simulation (with electromagnetic wave physics turned off) around the expected mechanical frequency (6-8 GHz) and find 40 modes within which we expect to find the breathing mode. We then pass the model to a MATLAB script that uses the simulated parameters of the two simulations together with material definitions (particularly components of the rotated photoelastic tensor p_{ij} given in equation 2.58 and diamond's relative permittivity $\epsilon_d = 5.7$) to perform calculations. For each simulated mechanical mode, the script calculates the zero-point motion amplitude x_{zpf} and the moving boundary (g_{mb}) and

photoelastic (g_{pe}) contributions to the optomechanical coupling (see section 2.3.3).

In particular, we calculate ten different integrals. I_{esq} integrates the electric field energy of the optical mode in both the diamond and the air box. I_{bnd} calculates the integral over the diamond surface in equation 2.55 which captures how the displacement of the mechanical mode boundary interacts with the optical mode electric field. Lastly, I_{11}, I_{12}, I_{13}, I_{16}, I_{26}, I_{33}, I_{44}, and I_{66} are integrals over the diamond volume which describes how strain in the material interacts with the optical mode electric field. We then have

$$g_{mb} = -\frac{x_{zpf}}{d_{max}} \frac{f_m}{2} \frac{I_{bnd}}{I_{esq}} \tag{4.4}$$

$$g_{pe} = \frac{x_{zpf}}{d_{max}} \frac{f_m \epsilon_0 \epsilon_d^2}{2} \frac{p_{11}I_{11} + p_{12}I_{12} + p_{13}I_{13} + p_{16}I_{16} + p_{26}I_{26} + p_{33}I_{33} + p_{44}I_{44} + p_{66}I_{66}}{I_{esq}} \tag{4.5}$$

We then pick out the breathing mode, which is the mode for which $abs(g_0) = abs(g_{mb}+g_{pe})$ is maximized (assuming that it was within the 40 simulated mechanical modes, which it typically is). Also note that in both equations we use the normalization factor x_{zpf}/d_{max} where d_{max} is the maximum displacement in the mechanical simulation. This scales all of the simulated displacements in the mechanical eigenfrequency result down to the level of the zero-point motion. This is not an exact normalization, which requires determination of what the maximum displacement of the OMC is for the breathing mode zero-point motion as described in the Strain section above, but because we do not know a priori the frequency of the breathing mode we use this as an estimate of the correct scaling

during optimization of the OMC design, which is where the optomechanical simulation is typically used. Once the breathing mode is selected, the optomechanical coupling can be corrected in postprocessing by simulating the maximum displacement for zero-point motion $d_{max,zpf}$ using the strain simulation and multiplying the previously calculated optomechanical couplings by the correction factor $d_{max,zpf}/x_{zpf}$, which is typically very close to 1.

4.2.5 Optimization

We automate optimization of the OMC pattern using MATLAB's genetic algorithm in conjunction with a cost function that simulates the optical quality factor and optomechanical coupling for a set of OMC parameters and returns a fitness value (typically $-g_0^2 Q_o$, with Q_o limited to 1 million to avoid unphysically high Qs from dominating) that the genetic algorithm tries to minimize. We define a seed set of parameters to give the algorithm that we know give a good fitness value (originally scaled parameters from a silicon OMC design in [50]). The genetic algorithm then produces a 'population' of parameters based on the seed parameters with a preset bounds that are simulated to give fitness values. The cost function ensures that these parameters are physical, checking for example that the mirror cell ellipse is not longer than the beam width. The best sets of parameters based on these simulations then move on to the next 'generation' and more sets of parameters are generated via inheritance of parameters from the dominant sets and random mutation. This process repeats until the algorithm finds a local minimum in the cost function that corresponds to an optimized geometry. The algorithm can then be re-seeded to exit this local minimum unless a satisfactory geometry has already been found. Typically, this process results in several sets of parameters that have $Q_o > 1$ million and $g_0/2\pi > 200$ kHz after a day or two of running. It is worth noting

that optimizing for g_0 inherently optimizes for zero-point strain since the photoelastic optomechanical coupling dominates g_0 and is dependent on the strain in the OMC, so strain or defect-spin coupling typically does not need to directly factor into the fitness value.

4.3 Fabrication

4.3.1 Diamond samples

To fabricate diamond OMCs, we obviously need to begin with a piece of diamond. This is generally a 500 μm-thick bulk electronic-grade single-crystal diamond formed by chemical vapor deposition from ElementSix. These diamonds are extremely high purity, with less than 5 parts per billion nitrogen, and have been shown to be mechanically superior to lower-purity diamonds [37], making them an excellent clean slate from which to fabricate our devices. From there we have to decide whether we are going fabricate our devices out of bulk diamond using a helium-implantation or quasi-isotropic etch technique or out of a thin, 1-20 μm diamond membrane bonded to silicon via our diamond-on-insulator (DOI) method.

For devices fabricated in bulk diamond we first clean the samples with our standard 2-acid clean of a 1:1 mixture of sulfuric and nitric acid at 190 C for $\approx$ 1 hour to ensure a pristine surface for initial processing. Then we move on to a strain-relief etch to remove polishing-induced strain at the surface of the diamond. This etch involves 15-60 min of our standard inductively-coupled plasma (ICP)[3] etch with ArCL plasma with gas flows 25 and 40 sccm respectively at a pressure of 0.7 Pa and 500 W ICP power/200 W bias power. This corresponds to etching $\approx$ 1-4 μm of diamond. We generally use this ArCl etch for

[3]For more information about ICP etching see appendix X

longer etches, despite the fact that it is rather slow, as it minimizes the formation of unwanted 'grass' that results from micromasking (redeposition of etched material, which then modifies the etch in its immediate vicinity) in oxygen-containing ICP etches. We follow this with 5s of our standard O_2 ICP etch, with a flow of 30 sccm, pressure of 1.33 Pa, and ICP/bias powers of 700/200 W. This etches $\approx$ 10 nm of diamond to remove any shallow-implanted Cl from the previous etch, which could have deleterious effects on any spins we introduce into our devices later on.

For DOI devices, we must form a membrane either by etching graphitized diamond formed via helium implantation, resulting in a $\approx$ 1 μm-thick membrane (discussed in more detail below) or by having the bulk diamond laser cut and polished into 20 μm-thick membranes. These membranes are then carefully electrostatically bonded to a piece of silicon. Then membranes are then cleaned using the same 2-acid clean described above. The 1 μm membranes are then ready for ion implantation while the 20 μm membranes first undergo strain relief etching and potentially another 2-acid clean.

4.3.2 Defect implantation

The ion species we have implanted include $_{14}$N, $_{28}$Si, and $_{4}$He. The nitrogen and silicon are implanted with the intent of forming nitrogen- and silicon-vacancy centers, while the helium is implanted with the intent of forming graphitized carbon for later removal (which we ignore for now and discuss in further detail below). Before implantation, we need to determine the ion implantation energy, dose, and angle. The energy controls the depth of the defect layer and for nitrogen and silicon we typically would like a depth of $\approx$ half of the OMC thickness in order to place the defect layer as far from the top and bottom OMC surfaces as possible. This corresponds to $\approx$ 100 nm and using the Stopping and Range of Ions in Matter (SRIM) simulation package, we determine that the energy required

for this depth is 90 keV for nitrogen and 150 keV for silicon. The dose together with the conversion efficiency of implanted ions to defect centers ($\approx 3\%$ for NV centers and 5% for SiV centers) determines the density of defects. For initial experiments we aim for a defect density of $\approx 1\ \mu\text{m}^{-2}$, which should give an array of individually-resolvable, non-interacting defects. This results in a required dose of $3 \times 10^9\ \text{cm}^{-2}$ for nitrogen and $2 \times 10^9\ \text{cm}^{-2}$ for silicon. Finally, we choose to implant at a tilt of 7°, which allows for channeling of the implanted ions through the diamond lattice, minimizing damage induced by the implantation.

Following ion implantation, the samples are annealed at 450 C in an O_2 atmosphere and next at 850 C in a H_2/Ar atmosphere to mobilize vacancies introduced during implantation. This serves two purposes: to form vacancy centers with the implanted ions and to move the lattice damage from implantation to the surface of the diamond. This graphitized layer is then removed with a one hour clean in a boiling perchloric, nitric, and sulfuric acid mixture which also serves to oxygen terminate the diamond surface.[4]

4.3.3 Diamond-on-insulator

All of the devices measured in this dissertation were fabricated using a diamond-on-insulator technique in which a diamond membrane is mounted (defect side down) to a silicon carrier chip with Hydrogen silsesquioxane (HSQ) and cured in a wafer bonder at 420 C and with 80 mBar of bonding pressure. After this bonding/curing process, the HSQ acts functionally as SiO_2 (hence 'on insulator') and is robust to the temperatures and acids required in subsequent fabrication steps, only being etched by hydrofluoric acid, which we take advantage of to undercut our devices toward the end of the fabrication process. Excess HSQ is removed from the silicon carrier wafer with a 10s dip in buffered

[4]This graphitized layer can also be removed with a much less scary clean involving a heated mixture of sodium nitrate and sulfuric acid. We discuss this in the context of helium implantation later on

hydrofluoric acid (BHF) before the diamond is thinned to the device thickness of 200-300 nm with repeated ArCl plasma etches (as described above) interleaved with solvent cleaning of the sample in acetone and isopropyl alcohol and 2-acid cleaning as necessary.

A significant drawback to using 20 μm membranes with this method is that they typically have a wedge to their thickness, sometimes varying in thickness by up to 1 μm or more over 2 mm. This results in only a portion of the thinned diamond being the correct thickness for fabricating OMCs. If one is lucky and the wedge is small, this area can be rather large, as for the samples described in chapter 5. However, for the sample in chapter 6, the wedge was more significant, resulting in only a single row of functional devices. This uncertainty in fabrication and device yield is one motivation for seeking other methods of fabricating our OMCs. The 1 μm membranes formed via helium implantation avoid this since their thickness is determined by the highly uniform depth of implanted helium ions. However, these membranes are difficult to form and release from the bulk diamond, and because of this typically have much smaller areas (a few hundred μm to a side) than the mm-sized 20 μm samples and are very fragile and difficult to handle. A drawback to the DOI technique overall is the inability to high-temperature ($>$ 850 C) anneal the sample post-fabrication, as the diamond membrane delaminates from the HSQ bond at these temperatures. Ideally, we would like to be able to perform such an anneal to heal any lattice damage incurred during fabrication, which should improve the properties of both the OMCs and any embedded vacancy centers.

Following bonding and thinning, the sample is ready to be patterned with our OMCs. We have done this using two different etch masks for transferring the OMC pattern into the diamond membrane. For the devices in chapter 5 we used an HSQ mask, while in 6 we used a SiN hard mask. These two process are described below.

HSQ mask

The original method used for fabricating diamond OMCs employed an HSQ mask for defining the devices and was adapted from the previously-developed recipe for making earlier diamond cantilever devices. The benefit of this method is that it does not require additional films to ask as hard masks since HSQ is able to withstand the O_2 etch used to transfer our device pattern into the diamond membrane, but the high dose required for electron beam lithography with HSQ can lead to charging issues and over-curing of HSQ on the backside of the device, making the bonding HSQ more difficult to remove.

After thinning and cleaning the sample (typically 2-acid and then piranha if needed), 3 nm of Cr are evaporated onto the diamond using the thermal evaporator. This acts as a sticking layer for the HSQ that we use as an electron-beam resist. 6% HSQ is then spun onto the Cr-coated diamond at 3 krpm [5] and baked at 95 C for 1 minute, followed by spinning Aquasave at 3 krpm and baking at 95 C for 15 seconds. The Aquasave provides a conductive surface above the HSQ, increasing the sample's conduction to ground to attempt to mitigate charging during electron beam lithography. Next, we perform electron beam lithography on the sample. A typical dose for this Aquasave/HSQ bilayer on top of our DOI stack is 1100 μC/cm^2. Following the lithography, the Aquasave is removed with a 5 second dip in de-ionized (DI) water. The HSQ is developed in 25% tetramethylammonium hydroxide (TMAH) for 1 minute. The development in stopped with a DI water dip.

The pattern is quickly inspected with a scanning electron microscope. If the pattern turned out well, the sample is ICP etched, first with O_2/Cl_2 (40/25 sccm, 500W ICP/15W bias, 0.7 Pa) for 30 seconds to remove the Cr sticking layer, then in O_2 (30 sccm, 700W ICP/200W bias, 1.33 Pa) for $\approx$ 4 minutes to transfer the pattern into the diamond. The

[5] Recipe #5 on the nanofab spinners

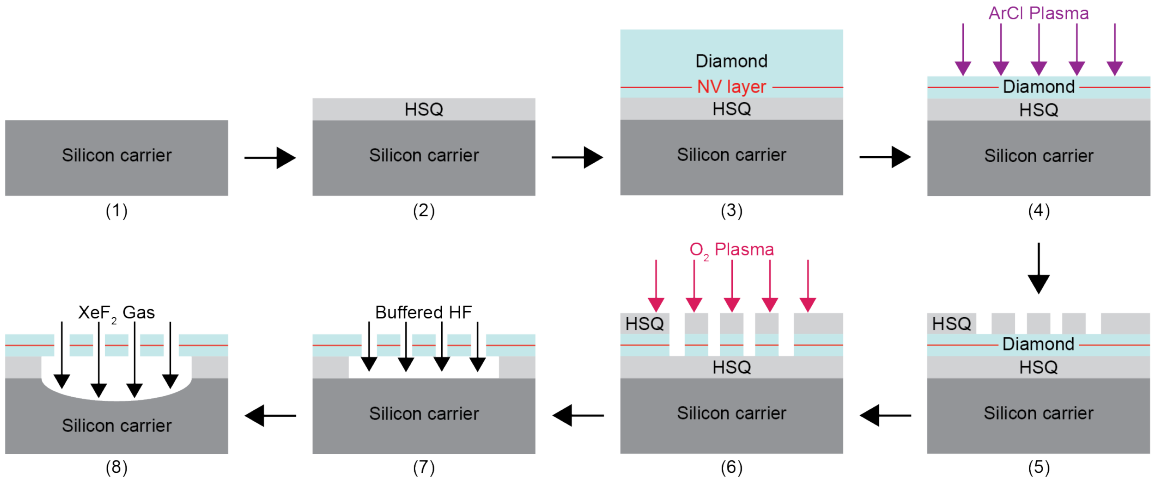

Figure 4.10: A simplified fabrication flow for diamond OMCs fabricated with an HSQ mask.(1) A silicon carrier chip is prepared and (2) coated with HSQ. (3) A ≈ 20 μm thick diamond membrane is wafer-bonded to the HSQ above the curing temperature for HSQ.(4) The diamond is thinned to the device layer thickness of 200 nm using a series of ArCl inductively coupled plasma (ICP) etches.(5) HSQ is patterned on top of the diamond using electron-beam lithography and then (6) used as an etch mask to define the devices in the diamond with an O_2 ICP etch.(7) The patterned devices are undercut with a BHF dip, which selectively etches the HSQ bonding layer underneath the devices.(8) The devices are further undercut using XeF_2 gas, which isotropically etches the silicon carrier wafer.

sample is then exposed to a gentle plasma for 1 minute while being heated to 200 C[6] to slightly etch the surface of the exposed HSQ layer, making it easier to remove with BHF in the next step.

Next the devices are undercut by etching the HSQ bonding layer with a series of ≈ 10 second BHF dips[7], which are stopped in DI water before transferring to IPA, inspecting after each etch to determine the undercut progression. Once the devices are undercut, we avoid blow drying them, instead transferring them from IPA to a 95 C hotplate for evaporative drying. These BHF dips also remove the HSQ mask. We then etch the sample for 15s in Cr etchant to remove the chrome sticking layer. Finally, we use XeF_2 to

[6]Recipe 2 or 3 in the Gasonics 2000

[7]Originally this was done for $\approx 10 - 15$ seconds before inspecting the undercut, but if this process is used in the future, a short (few second) BHF dip should be done to just remove the exposed HSQ before performing a XeF_2 etch and more, longer BHF dips, as described in the SiN process below.

isotropically etch the silicon bonding wafer under the devices to increase the separation between the OMC and the bulk silicon which is necessary for achieving high optical quality factors since the separation provided by the HSQ bonding layer is typically only ≈ 200 nm. The etch entails 3 15-second cycles of 2 torr of XeF_2 in the etching chamber but can be adjusted in time or pressure to etch more or less silicon. The gap between the OMC and the bulk silicon should be checked after this etch by examining the sample at an angle in the SEM to ensure that it is at least 1 μm, preferably more. Lastly, the sample is cleaned using a standard 2-acid clean.

SiN mask

The current method used for fabricating OMCs out of diamond membranes uses CSAR-62 instead of HSQ as an electron beam resist, which is used to pattern a low-stress SiN hard mask, which in turn is used to transfer the pattern into the diamond. This method has many advantages over the HSQ mask method. These include lower doses required for electron beam lithography (320 μC/cm^2 for CSAR versus 1100 μC/cm^2 for HSQ), spatial separation between the lithography layer and the HSQ bonding layer provided by the ≈ 200 nm-thick SiN layer, and ease/safety of developing, as CSAR is developed in amyl acetate, a common solvent, as opposed to the more dangerous TMAH required to develop HSQ.

After thinning and cleaning the sample, ≈ 20 nm of aluminum oxide (AlOx) is grown on the sample via atomic layer deposition (ALD), followed by ≈ 200 nm[8] of low-stress SiN deposited via plasma-enhanced chemical vapor deposition (PECVD). The AlOx layer serves as an etch stop when the SiN is etched, protecting the diamond membrane. The SiN film surface is then etched for 10 seconds at 200 C in a downstream etcher to slightly

[8]This is typically 30 minutes of deposition in the PECVD2 tool.

modify the surface in preparation for spin-coating electron beam resist[9]. CSAR-62 that has been mixed in a 3:1 ratio with anisole [10] is spun onto the sample at 4 krpm for 1 minute with an 800 rpm/s ramp rate and baked at 150 C for 1 minute.

Next, the resist is exposed using electron beam lithography, with a typical electron dose of 320 μC/cm^2 and developed in amyl acetate for 1 minute followed by a 30 second stop in IPA before blowing dry. The patterned CSAR can be examined in the SEM to ensure that all features have been properly realized. The resist pattern is then transferred into the SiN layer with a $\approx$ 1 minute 15 second CHF_3/O_2 ICP etch (40 sccm/10 sccm, 500W ICP/50W bias, 0.5 Pa, $\approx$ 180 nm/minute). The CSAR is stripped with N-Methylpyrrolidone (NMP) at 80 C for 10 minutes. At this point, the patterned SiN can be inspected in the SEM. If satisfactory, the AlOx layer is etched with a BCl_3 ICP etch (30 sccm, 500W ICP/200W bias, 0.5 Pa, 1.1 nm/second) for 20-25 seconds, exposing the diamond through the mask layers. The OMC pattern is then transferred into the diamond with the same O_2 ICP etch described above. This etches the diamond with a selectivity of at least 20:1 over the SiN, making the SiN a very robust etch mask[11]. The SiN is then removed with a $>$ 1 hour etch in 85% o-phosphoric acid at 155 C. This etch selectively etches the SiN, leaving the bonding HSQ untouched, as opposed to the more commonly used BHF. The sample is then downstream etched for 1 minute at 200 C to prepare the HSQ bonding layer for etching with BHF.

The sample is then dipped in BHF for 10 seconds to etch the HSQ mainly in the exposed regions, then DI water, then IPA before evaporative drying on a hotplate at 95 C. The silicon carrier wafer is then isotropically etched with XeF_2 (3-4 15 second cycles,

[9]The resist will not stick if this step is skipped.

[10]This dilution gives a $\approx$ 300 nm spun layer

[11]The caveat here is that thin features in the SiN mask such as the 40 nm phononic shield linkages can have relatively shallow and rounded sidewalls for SiN layers thinner than 200 nm, worsening during the diamond etch such that the bottom of the mask can be thinned away, causing the diamond feature to be thinner than desired.

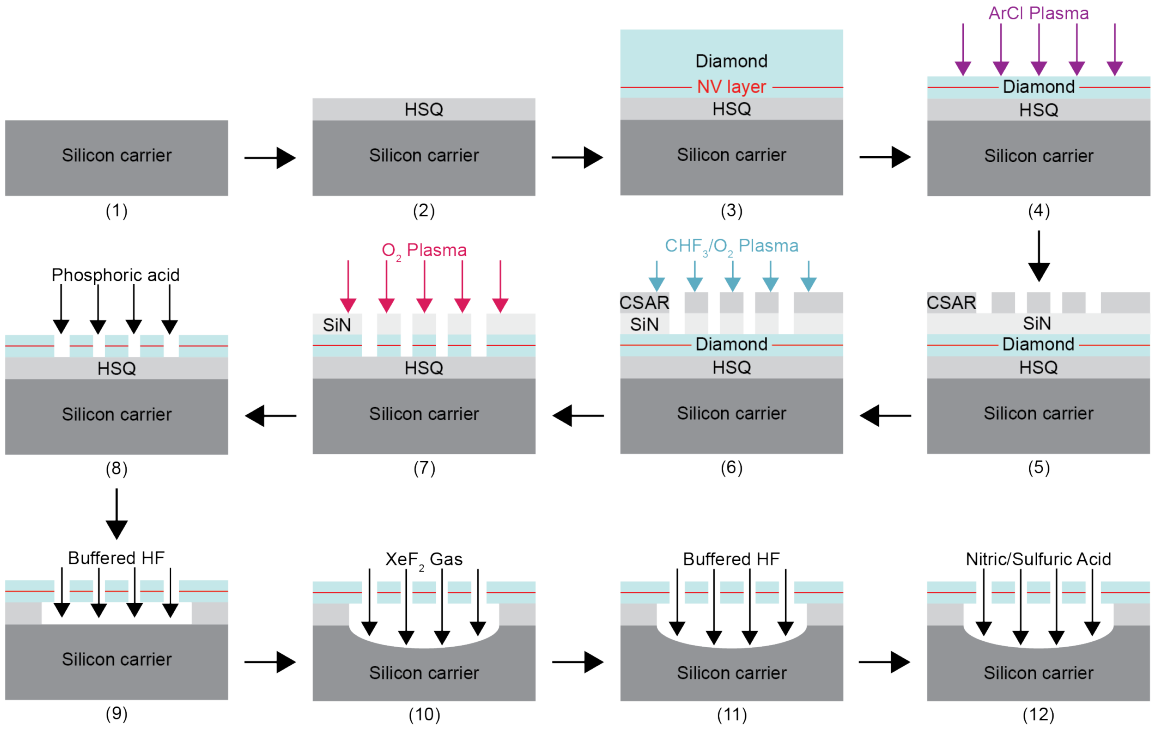

Figure 4.11: A simplified fabrication flow for diamond OMCs fabricated with a SiN mask. (1) A silicon carrier chip is prepared and (2) coated with HSQ. (3) A ≈ 20 μm thick diamond membrane is wafer-bonded to the HSQ above the curing temperature for HSQ. (4) The diamond is thinned to the device layer thickness of 200 nm using a series of ArCl inductively coupled plasma (ICP) etches.(5) Low-stress SiN is deposited and electron beam lithography is performed with CSAR electron beam resist. (6) CHF_3O_2 plasma transfers the electron beam pattern into the SiN mask (7) followed by an O_2 plasma etch to transfer the pattern into the diamond layer. (8) Phosphoric acid removes the SiN layer and (9) buffered HF acid removes the HSQ directly underneath the device. (10) XeF_2 gas etches the silicon carrier wafer to increase the undercut depth below the devices before (11) another buffered HF dip removes any leftover HSQ on the diamond backside. (12) A 2-acid clean removes any additional contaminants prior to measurement.

2 torr XeF_2), before a 5-10 second BHF dip to remove HSQ on the exposed backside of the diamond. The BHF dips also serve to remove the AlOx layer. Lastly, the sample is cleaned with a 2-acid clean.

4.3.4 Uniform-thickness diamond membrane creation via helium implantation and graphitization

As was previously mentioned, an outstanding challenge in diamond fabrication is the creation of large, high-quality, uniform-thickness membranes out of which nanostructures can be fabricated. One potential solution is the creation of a subsurface graphitized layer via ion implantation and subsequent high-temperature annealing [75, 76, 77, 78, 79]. The ion implantation process is capable of producing a damaged diamond layer of uniform depth and thickness. Above a critical vacancy threshold of $\approx 1 - 5 \times 10^{22}\text{cm}^{-3}$ [80] (with deeper damaged layers having a higher graphitization threshold [78]), the damaged layer converts to graphite, which can be selectively etched by a variety of methods, including electrochemical etching [76, 81], annealing in the presence of oxygen [79], etching in a heated solution of sodium nitrate and sulfuric acid, or potentially a quasi-isotropic oxygen plasma etch. However, to this point this method has focused on the creation of lifted-off membranes that can subsequently be used similarly to the laser sliced membranes described in the diamond-on-insulator section above. This focus has limited these membranes in size and quality due to the difficulty of etching a subsurface graphitized layer greater than $\approx 300\ \mu\text{m}^2$ and the fragility and poor surfaces of these lifted-off membranes [82]. In theory, any ion can be used for this process, but helium is typically used due to its narrower implantation distribution (and thus more clearly delineated damage/graphite layer).

Our proposed improvement to this process is to perform device fabrication on a bulk

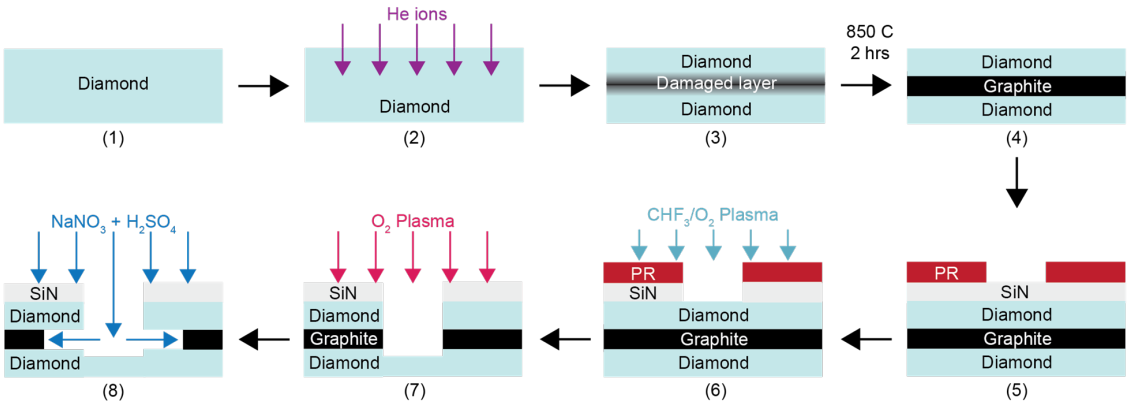

Figure 4.12: A simplified fabrication flow for diamond membranes with a subsurface graphite layer. (1) A bulk diamond piece is prepared and (2) implanted with He ions, leading to (3) a subsurface damaged layer. A high-temperature vacuum anneal causes this damaged layer to become (4) graphitized. (5) Low-stress SiN is deposited and photo- or electron beam lithography is performed to define a device pattern. (6) CHF_3O_2 plasma transfers the electron beam pattern into the SiN mask (7) followed by an O_2 plasma etch to transfer the pattern into the diamond and graphite layers. (8) The graphite layer is selectively removed with either a heated solution of sodium nitrate and sulfuric acid, an oxygen anneal, an electrochemical etch, or a quasi-isotropic oxygen plasma etch.

diamond with a subsurface graphitized layer and perform the graphite etch after defining the devices, as shown in figure 4.12. Retaining the attachment to the bulk diamond would allow for larger sample sizes and for further high-temperature annealing to repair implantation and fabrication-induced damage without fear of the membrane delaminating as in the case of bonded membranes. For our lab, prior to helium implantation the samples are cleaned and undergo a strain-relief etch as described in the previous section. The samples are then sent to Los Alamos/Sandia National Laboratories, which have a variety of ion implantation tools capable of covering a wide range of ion dose and energy combinations. SRIM calculations are carried out to determine the dose and energy of an implantation for a given application. A typical dosage of 1e17 cm^{-2} and energy of several hundred keV should give graphite layers several hundred nm thick and on the order of 1 micron deep. Multiple implantations at different energies can be used to increase

the graphite layer thickness. The implantations are masked with a micromachined grid of openings to create an array of $\approx$ 100 μm^2 damaged regions. This will allow for subsequent removal of graphite while maintaining attachments to the bulk diamond and avoid unwanted stress due to lattice mismatch between the graphite and diamond layers. After implantation, the samples are annealed in high vacuum at 850 C for 2 hours to form the graphitized layer. After this, as is mentioned above, there are several options for removing the graphite while protecting (to varying degrees) the diamond layer. A standard method is to use an electrochemical etch in which the diamond is submerged in ultrapure water and voltage probes (with $\approx$ 50 V across them) are placed close to the diamond. These conditions selectively etch graphite, but it has been seen before in our lab that the etch rate is relatively slow and highly dependent on the positions of the voltage probes relative to the region to be etched. Another method of selectively etching graphite is by using a mixture of 1 cm^3 sodium nitrate and 40 mL sulfuric acid at 245 C for several hours (or days). This etch is very slow but relatively controllable. A cover slip should be used for long etches to minimize evaporation of the etch solution. There are two other methods that can etch graphite but can also etch diamond in undesirable ways. First, the diamond can be annealed at 450 C in the presence of oxygen, however this etch is also rather slow and puts the diamond surface at risk of being roughened, as diamond starts to be etched by oxygen at temperatures slightly higher than this. Lastly, a quasi-isotropic O_2 plasma etch [25] can be used to simultaneously etch the graphite and diamond in the case that etching the diamond is desirable (if one wants to tune the thickness of the diamond membrane layer). Work on this method of diamond fabrication is ongoing but would enable very high fabrication yield and larger, more complex phononic systems if successful.

Chapter 5

Diamond optomechanical crystals with embedded nitrogen vacancy centers

5.1 Introduction

Our OMC design consists of a single-crystal diamond nanobeam with a rectangular cross-section and a one-dimensional array of etched ellipses along its length and is fabricated using a diamond-on-insulator technique. The rectangular cross-section is in contrast to the work in [17], which employs diamond OMCs with triangular cross-sections fabricated using an angled-etching technique. The rectangular cross-section enables important advantages, namely the z-symmetric strain profile of the fundamental 'breathing' acoustic mode and the ability to fabricate two-dimensional phononic shields and couple to single-mode waveguide structures [51]. We engineer the OMC optical resonance to be $\approx$ 200 THz to facilitate integration with mature 1550 nm telecommunication technologies.

OMCs with this optical frequency also host mechanical resonances with frequencies of a few GHz. We choose an OMC thickness of 200 nm, which provides a balance between the competing values of optical quality factor, for which a thicker OMC would be optimal, and strain, which increases for thinner OMCs. We then follow the design prin-

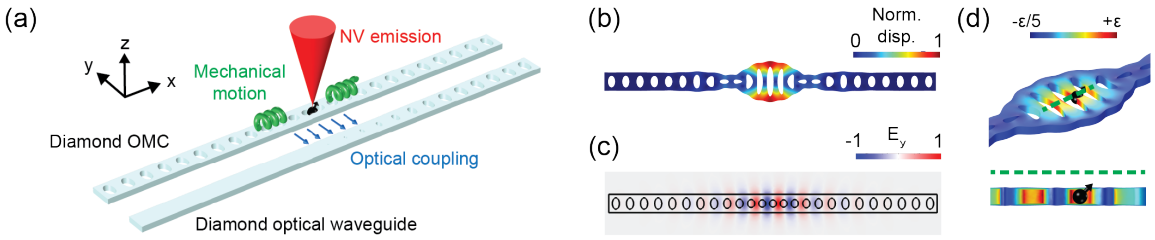

Figure 5.1: a) The system under study, in which an NV center is embedded near the center of a diamond OMC and interacts with the mechanical motion of the OMC via crystal strain. The NV is measured by collecting the light it emits with a confocal microscope, while the OMC is probed via coupling to an adjacent diamond optical waveguide. b) The normalized displacement of the fundamental 'breathing' mechanical mode and c) the normalized electric field of the optical mode of the diamond OMC, simulated using the finite-element method (FEM).(d) The ε_{yy} component of the strain tensor in the device basis due to the displacement of the breathing mode, also simulated with FEM. The line cut shows the z-symmetric nature of the strain profile and the optimal placement of an NV in a large-strain region that is also isolated from the device surfaces.

ciples outlined in [50] in which 'mirror' unit cells at either end of the OMC adiabatically transition to a 'defect' unit cell at the center through slight changes in the shape and spacing of the etched holes in the region between the defect and mirrors. The mirror cells host incomplete, symmetry-dependent acoustic and optical band gaps around the breathing acoustic mode (figure 5.1b)) and fundamental transverse-electric (TE) optical mode (figure 5.1c)) frequencies. Further acoustic isolation is provided by a phononic shield surrounding the OMCs, which hosts a full phononic bandgap around the breathing mode resonance frequency.

5.2 Initial OMC tests

Initial OMC tests were useful for working out general aspects of the OMC geometry and design. The first set of measurements taken in the Safavi-Naeni lab on the first OMC showed fiber coupling but no resonances, leading to the hypothesis that the gap between the OMCs and the silicon was too small. After using a XeF_2 etch to increase this gap,

very low-Q optical resonances were observed near 1400 nm, too low for the mechanical signal to amplified and detected with typical telecom equipment. This result enabled us to fine-tune our OMC design protocol, leading to the second set of devices that are discussed below.

5.3 Adjustments and optimizations

To optimize our OMC design for optical quality factor and strain, we simulate the optical and mechanical resonances of the OMC with the finite element method (FEM) software COMSOL and use a genetic algorithm to search the design parameter space and maximize the product $Q_o\varepsilon_0$, where Q_o is the optical quality factor for the fundamental TE optical mode and ε_0 is the strain due to zero-point motion of the mechanical resonance. We simulate the zero-point optomechanical coupling g_0 between these optical and mechanical modes to be $g_0/2\pi \approx 330$ kHz and a zero-point amplitude of ≈ 3 fm for the finalized design. The strain profile of the breathing acoustic mode for our rectangular cross-section devices is constant throughout the thickness of the device, allowing an embedded NV center to experience high-strain even if it is equidistant from the top and bottom surfaces of the OMC, isolating the NV center from surface-induced noise [38, 56]. Thus, as shown in figure 5.1d, the ideal placement of an NV center in one of our diamond OMCs based on the FEM simulated strain profile for the breathing mode would be approximately halfway between the defect hole and the adjacent hole and equidistant from the top and bottom surfaces of the diamond. This would place the NV in a high-strain region that is approximately 100 nm from any surface, providing isolation from surface-related decoherence mechanisms. At this location, we simulate the strain due to zero-point motion to be $\approx 10^{-8}$. Using the formalisms and measured stress coupling constants presented in [83, 36] for the spin interaction and [71] for the orbital interaction,

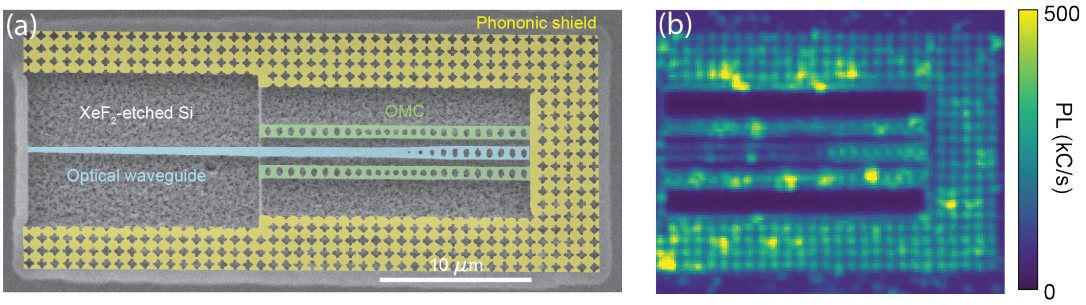

Figure 5.2: a) SEM micrograph of a pair of diamond OMCs on either side of a diamond optical waveguide. The devices are surrounded by a cross pattern phononic shield.b) A scanning confocal micrograph of a device similar to that shown in a). Single NVs can be discerned in the area surrounding the phononic shield but scattering from the etched holes and sidewalls makes them difficult to see inside the OMCs.

we estimate zero-point coupling strengths of ≈ 200 Hz and ≈ 10 MHz, respectively.

5.4 Basic OMC characterization

We measure the optical and mechanical resonances of our OMCs using a room-temperature fiber setup, as shown in figure 5.3. For measurement of optical resonances, light is sent from a wavelength-tunable laser (1500-1630 nm) through a fiber polarization controller to match the polarization of the light to that of the OMC TE optical mode, then through a fiber circulator. To couple the light onto the diamond chip, we employ a tapered optical fiber setup such as in [84], in which light is transferred from a tapered optical fiber into an on-chip diamond optical waveguide (which is centered between two nominally identical OMCs, as shown in figure 5.2a. The optical frequencies of adjacent OMCs are nearly always spectrally resolvable by more than the optical linewidth, ensuring their ability to be individually addressed. The incident light can then evanescently couple into the OMCs when on resonance with the optical mode hosted by the OMC or continue down the waveguide and reflect off mirror cells which are designed to be identical to those in the OMCs. The reflected light then couples back into the tapered fiber

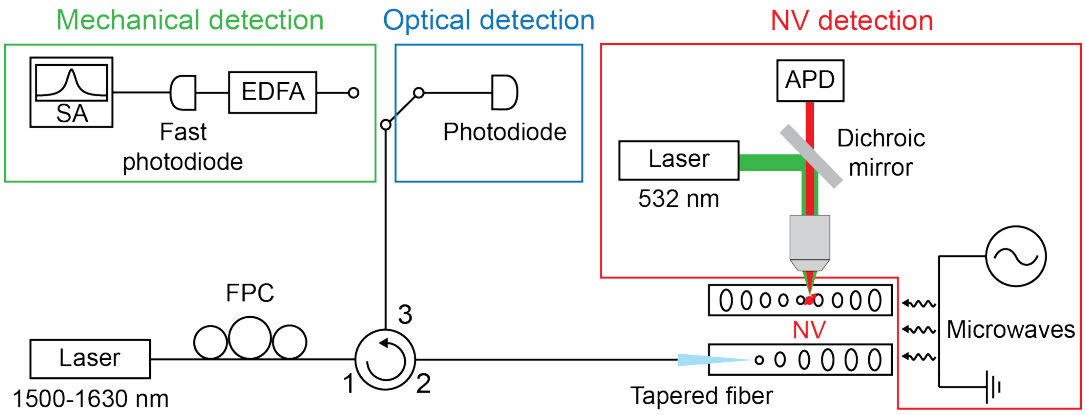

Figure 5.3: A combined NV and OMC characterization setup. To measure the optical response of the OMC, light from a tunable laser is sent through a fiber polarization controller (FPC) and a fiber circulator to a tapered optical fiber, which couples light into an on-chip diamond optical waveguide. The light reflects from the OMC and a patterned mirror at the end of the waveguide and re-enters the tapered fiber. The light goes once more through the fiber circulator before being measured with a DC photodiode. To measure the thermal mechanical motion of an OMC, the laser wavelength is set within an optical resonance but instead of being measured with a DC photodiode, is amplified with an erbium-doped fiber amplifier(EDFA) and sent to a fast photodiode which converts the intensity modulated light into an electrical signal which can be measured with a spectrum analyzer(SA). NV measurements are carried out with a home-built scanning confocal microscope in which 532 nm light is used to excite the NVs and fluoresced red photons are measured using an avalanche photodiode (APD). Microwaves for NV spin manipulation are delivered via a wire bonded over the diamond.

and gets circulated to a photodiode, where the DC power of the reflected light is measured. Light that interacts with the OMC before leaking back into the waveguide gains a phase relative to the light that reflects off the waveguide mirror; an optical resonance is thus identified by a dip in the reflected power spectrum at the OMC optical resonance wavelength due to interference between these two optical paths. Figure 5.4a shows such a spectrum with an optical resonance at 1564.2 nm and a quality factor of 42,000. Since our optical resonances are not in the sideband-resolved regime for the 6 GHz OMC acoustic mode, we detect the mechanical mode by setting our laser to a wavelength within the bandwidth of the OMC optical resonance. The Brownian motion of the OMC imprints phase fluctuations onto the light that interacts with the cavity, which then interferes with light that reflected off the waveguide mirror. The resulting intensity-modulated reflected optical signal is amplified with an erbium-doped fiber amplifier before being measured with a fast (12 GHz) photodetector and sent to a signal analyzer. Figure 5.4b shows the detected mechanical spectrum, which we associate with the breathing acoustic mode. A fit to this signal gives a mechanical quality factor of 118. Due to the inherent thickness wedge of the diamond and intentional variation of the optical coupling gap, there were $\approx$ 100 usable devices on the chip out the $\approx$ 1000 fabricated, of which $\approx$ 50 were measured and found to consistently have optical resonances in the 1530–1560 nm range and quality factors of 10,000–40,000, consistent with the device thickness, coupling gap, and simulated loss in the silicon substrate. Of these, $\approx$ 10 were measured for mechanics and were all found to have mechanical resonances near 5.9 GHz with mechanical quality factors of $\approx$ 100.

This low mechanical quality factor, when compared to other devices in ambient conditions [17], could be due to leftover HSQ on the backside of the devices that was not completely removed during the undercut step (step 7 in figure 4.10), etch-induced sidewall roughness, or deviations in the fabricated device dimensions from the design. The

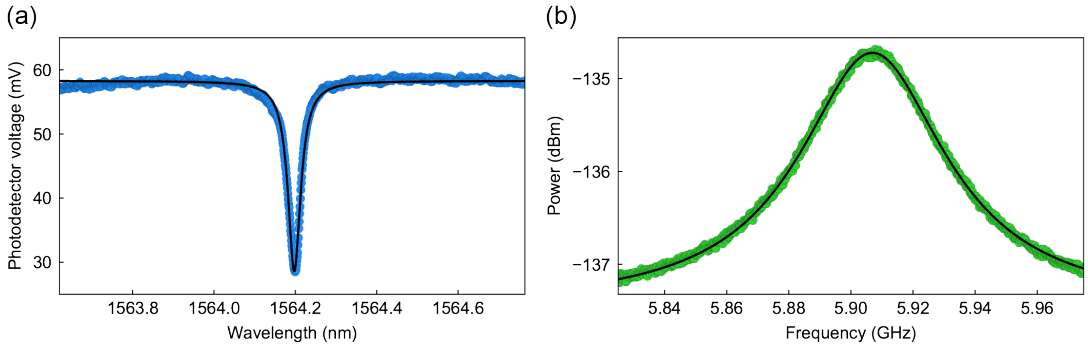

Figure 5.4: a) A typical optical resonance for a diamond OMC. A Lorentzian fit gives a quality factor of 42000. b) The measured mechanical spectrum, which we associate with the OMC breathing mode. A fit to the signal gives a quality factor of 118.

large electron-beam dose required to expose the HSQ mask also exposed the HSQ on the backside of the devices, making it particularly difficult to remove. In the future, this issue can be avoided by using an electron-beam resist that requires a lower dose, undercutting with XeF_2 before the HF HSQ undercut step to allow the HF more access to the backside of the device, and spacing the devices further apart to allow for longer HF etch times without completely releasing the diamond. We do not suspect etch-induced sidewall roughness to be a dominant mechanical dissipation mechanism, as optical quality factors, which are high and consistent with device simulations, would also be deteriorated. Because devices with and without phononic shields had similar quality factors, imperfections in the phononic shield are also not suspected to limit performance. Lastly, from SEM images, we see that the fabricated device dimensions differ slightly from the design: namely, the mirror holes are $\approx 15\%$ wider while the beam width in the y-direction is $\approx 10\%$ narrower. Simulations, however, indicate that these deviations do not limit the mechanical quality factor.

5.5 NV center spins in diamond OMCs

Preserving the spin properties of NV centers near nanofabricated surfaces is a perennial challenge. To characterize the ground state spin properties of the NV centers in our OMCs, we use a home-built confocal microscope, a simplified version of which is shown in figure 5.3. A fluorescence image of representative OMC devices is shown in figure 5.2b. We first detect the presence of NV centers near the center of our OMC using optically-detected magnetic resonance of the NV center spin, in which the NV center is continuously excited with 532 nm light while being irradiated with microwaves. We note that most OMC devices contain an NV center near the center, with some containing 2 or 3. A dip in the photoluminescence of the NV center near 2.68 GHz (figure 5.5a) corresponds to a transition from the $m_s = 0$ spin state to the $m_s = -1$ spin state, with a small external magnetic field shifting the transition from the 2.87 GHz zero-field splitting. Three dips are present due to hyperfine coupling to the $_{14}$N nuclear spin of the NV center. The ability to resolve hyperfine splitting is already indicative of well-preserved spin coherence. To quantitatively characterize the spin coherence of this NV center, we perform microwave-driven Rabi, Ramsey, and Hahn echo measurements in which the NV center is prepared in the $m_s = 0$ ground state with a 532 nm laser pulse before undergoing the microwave pulse sequences called for by these measurements. For the measurement of Rabi oscillations, the NV center spin evolves under continuous exposure to microwaves resonant with the transition from the $m_s = 0$ state to one of the hyperfine sublevels of the $m_s = -1$ state for some amount of time before the spin-state is read out via spin-dependent fluorescence. Figure 5.5b shows persistent Rabi oscillations between these two states. Deviation of the signal from a cosine function is due to beating with the other hyperfine sublevels. For the Ramsey measurement shown in 5.5c, the spin is pulsed into a superposition of the $m_s = 0$ and $m_s = -1$ states with microwaves slightly detuned

from the transition. The spin then freely evolves for $T = \tau$ before being projected back onto the $m_s = 0$ state and measured. The decay of the resulting oscillations, which are due to interference between the different hyperfine sublevels, is fit to $\exp -(\tau/T_2^*)^2$ where T_2^* is the bare coherence time of the NV center spin. From the fit we extract $T_2^* = 1.5$ μs. In order to measure the NV center spin coherence when decoupled from slowly evolving noise sources, we perform a Hahn echo measurement. Microwaves resonant with the $m_s = 0$ to $m_s = -1$ transition place the spin in a superposition of the two states, after which the spin is allowed to evolve for $T = \tau$ before a refocusing pulse is applied and the spin is again allowed to evolve for $T = \tau$, for a total free evolution time of 2τ. The result of this measurement is shown in figure 5.5d. We associate the oscillations in the signal with hyperfine coupling to a proximal $_{13}$C nuclear spin as well as the Larmor precession of the $_{13}$C nuclear spin bath present in the diamond. The decay of this signal is fit to $\exp -(2\tau/T_2)^2$, where T_2 is the Hahn echo coherence time of the NV center spin. From the fit we find $T_2 = 72 \pm 6$ μs, comparable to NVs in non-isotopically purified bulk diamond, in which T_2 is limited to ≈ 300 μs, with further degradation possibly arising due to local implantation damage and adjacency to surfaces [85].

5.6 Summary and discussion

In summary, we have demonstrated the fabrication of rectangular cross-section diamond OMCs with embedded NV center spins. Rectangular cross-section OMCs are particularly promising for hybrid NV-mechanical systems due to the z-symmetric strain profile of the fundamental breathing acoustic mode and the ability to fabricate two-dimensional phononic shields, which should allow for high mechanical quality factors. Our diamond OMCs host optical modes with quality factors of up to 42,000 and an acoustic breathing mode near 6 GHz with quality factors of ≈ 100 in ambient conditions.

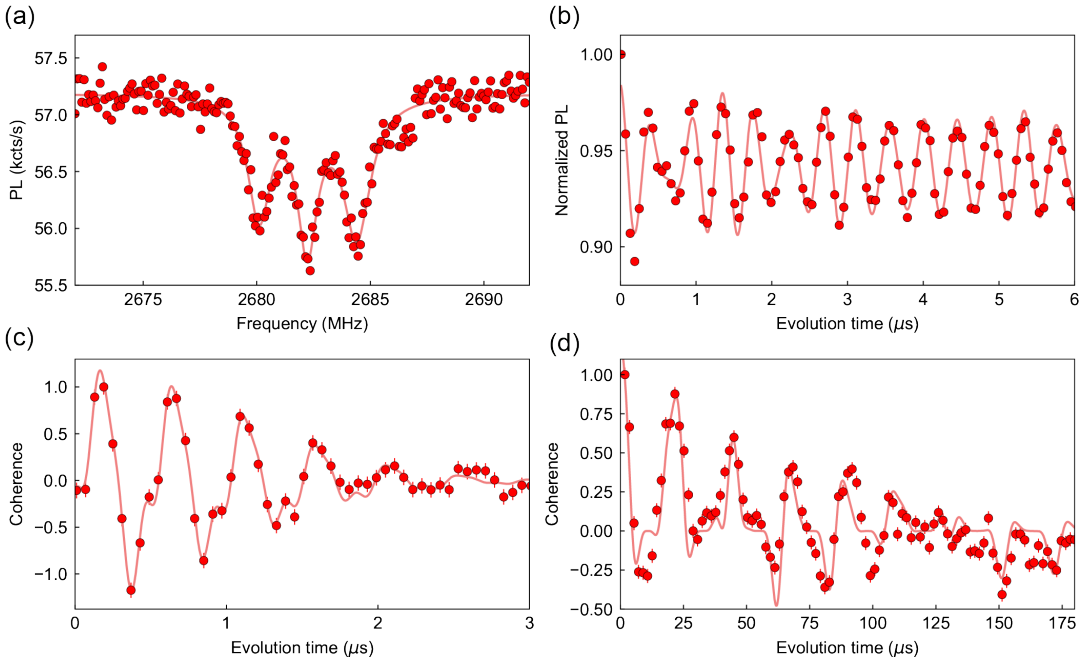

Figure 5.5: a) NV spin characterization measurements for an NV located near the center of an OMC. a) Microwave-driven optically-detected magnetic resonance measurement of the $m_s = -1$ spin state of the NV, in which the hyperfine sublevels due to the adjacent $_{14}$N nucleus are resolved. b) Persistent, microwave-driven Rabi flopping between the $m_s = -1$ and $m_s = 0$ spin states of the NV. c) A Ramsey measurement of the qubit formed by the $m_s = 0$ and $m_s = -1$ spin states. A fit to the decay gives $T_2^* = 1.5$ μs. d) A Hahn echo measurement on the same states as in c). A fit to the signal that includes both the effects of a $_{13}$C spin bath and a proximal $_{13}$C nucleus gives $T_2 = 72$ μs. In c) and d) error bars indicate one standard deviation.

Importantly, our fabrication process preserves the long spin coherence time of NV centers, which we demonstrate by measuring a coherence time of $T_2 = 72$ μs. To reach the high cooperativity regime for coupling between an NV center spin and the mechanical motion of a diamond OMC ($C = 1$ for the current devices), improvements to the mechanical quality factor and NV center spin coherence are necessary, in addition to larger engineered strain. For an OMC with a mechanical quality factor of 10^6 in its ground state of motion, a zero-point coupling strength of 1 kHz, and NV center spin T_2 of 10 ms [57], C $>$ 1 becomes possible. To this end, future iterations of these devices will implement modifications to the design and fabrication procedure to ensure full removal of the HSQ from the backside of the OMCs as well as accuracy of the fabricated device dimensions in an attempt to increase the mechanical quality factor. Furthermore, by using diamond that has been grown with isotopically pure $_{12}$C and using a delta-doped nitrogen layer and electron irradiation to form NV centers [86], we hope to improve the NV center spin properties in our OMCs. If the high cooperativity regime is reached, experiments such as quantum state transfer between 1550 nm light and an NV center spin and phonon-mediated spin–spin interactions become realizable. While the NV center spin properties have been preserved in our OMCs, future experiments at low temperature will be required to determine the properties of the NV center orbital excited state. For a zero-point coupling strength of 10 MHz, a mechanical quality factor of 10^6, and an excited state linewidth of 100 MHz [87], C $\approx$ 10 for the orbital-phonon interaction. This high cooperativity would enable, for example, cooling of the mechanical resonator using phonon-assisted transitions to the NV center orbital excited state. A final phonon occupation $\overline{n} \approx 1$ is possible using either a resonant or off-resonant cooling scheme, assuming optical Rabi frequencies of $\approx$ 1 MHz and $\approx$ 1 GHz, respectively [31]. Furthermore, the larger strain interaction strength in the excited state can be used to provide an enhanced spin-phonon interaction using phonon-assisted Raman transitions [43, 88], indicating a

potential alternative path to high cooperativity for NV spin-mechanical devices.

Chapter 6

Low-temperature characterization and optical absorption heating of diamond OMCs

6.1 Introduction

As mentioned previously, OMCs are an active area of study in the field of quantum technologies due to their long phonon lifetimes and their potential role in quantum communication. However, their uses for sought-after protocols such as frequency conversion between microwave and telecom frequencies and dissipative squeezing of mechanical motion are currently limited by optical absorption heating at the high intracavity optical powers required for these experiments, which raises the phonon bath temperature and lowers the mechanical quality factor. In silicon, this absorption is thought to be predominately due to near-surface defects in the native oxide layer which can be excited by 1550 nm photons and release mechanical energy into the OMC upon relaxation [1, 89]. In silicon OMCs at 20K, at intracavity photon numbers less than 10^3, this absorption has been shown to lead to increases in the bath temperature of more than 10K and a corresponding increase in the intrinsic mechanical linewidth of nearly 50% [20]. The effect of this heating becomes more dramatic at dilution refrigerator temperatures [90, 91, 1]

when the thermal conductivity of the thin film out of which the OMC is fabricated decreases, preventing absorption-generated heat from being effectively dissipated into the bulk [92]. This can be mitigated somewhat by using device architectures that increase thermal contact with the cold surrounding material, but nevertheless significant heating and degradation of mechanical quality factor were still seen in such devices, making operation in the ground state of mechanical motion difficult. From these results, it is clear that minimizing optical absorption heating in OMCs would be a significant boon to the field and enable many interesting experiments that are infeasible with previously demonstrated devices fabricated in other materials. Diamond, which hosts a large optical bandgap and lacks a native surface oxide, is ideally suited to avoid or mitigate heating due to optical absorption.

On the diamond mechanics front, we seek to improve upon the devices presented in the previous chapter by way of modifications to the OMC geometry and fabrication process in order to improve the mechanical quality factors of our devices. We then seek to measure OMCs at low temperature in our closed-cycle helium cryostat to better understand their operation in the quantum regime for future experiments involving embedded defect centers. In particular, demonstration of a diamond mechanical resonator with high enough strain and mechanical quality factor at low temperatures to support high-cooperativity coupling to defect center spins is an outstanding challenge.

In this chapter, we detail the device and fabrication modifications made to improve our diamond OMC performance as well as characterization of these devices at room temperature to determine their zero-point optomechanical coupling rate g_0 their optical and mechanical quality factors at room temperature and 6K, to demonstrate laser cooling of a diamond OMC, and to examine the effects of large photon amplitudes in the OMCs on the OMC temperature and mechanical quality factor. We find the largest fQ product ever reported for a diamond mechanical resonator, demonstrate laser cooling of the OMC

mechanical mode to a mode occupancy of $\overline{n} = 18$, and find mechanical quality factors greater than 10^5 even for $n_c > 10^4$ photons in the cavity.

6.2 Device design and fabrication

Modifications to the device architecture were made to mitigate potential sources of mechanical losses. First, the OMCs were completely decoupled from the optical waveguide such that the OMC was only clamped at points surrounded by phononic shielding. To allow for this decoupling, the optical waveguide was clamped outside of the phononic shielding, and a tapered coupling structure was added at the end of the waveguide to make it a stiffer structure. The parameters for the OMC geometry were determined using a genetic optimization algorithm in tandem with finite element simulations in COMSOL. Two designs resulted from running this optimization for a figure of merit involving the simulated vacuum optomechanical coupling g_0 and optical quality factor Q_o, $f = g_0^2 Q_o$, limiting Q_o to less than 10^6 to avoid unrealistic optical quality factors from unfairly weighting the simulation. Design 1 had a simulated mechanical frequency of $\omega_m/2\pi = 7.64$ GHz for the fundamental breathing mode (shown in figure 6.1a) and optical frequency of $\omega_c/2\pi = 197.5$ THz ($Q_o = 129,000$) for the fundamental TE-mode (shown in figure 6.1b), with a simulated vacuum optomechanical coupling $|g_0|/2\pi = 270$ kHz (moving boundary contribution $g_{mb}/2\pi = -26$ kHz, photoelastic contribution $g_{pe}/2\pi = -244$ kHz). Design 2 had $\omega_m/2\pi = 6.34$ GHz, $\omega_c/2\pi = 195.4$ THz ($Q_o > 10^6$), $|g_0|/2\pi = 224$ kHz (moving boundary contribution $g_{mb}/2\pi = 2.5$ kHz, photoelastic contribution $g_{pe}/2\pi = -226.5$ kHz). The device parameters are listed in appendix **??**.

The diamond OMCs were fabricated using the SiN mask diamond-on-insulator method described in section 4.11. More separation between devices than was used previously allowed for additional BHF etching without fully undercutting the diamond. Due to the

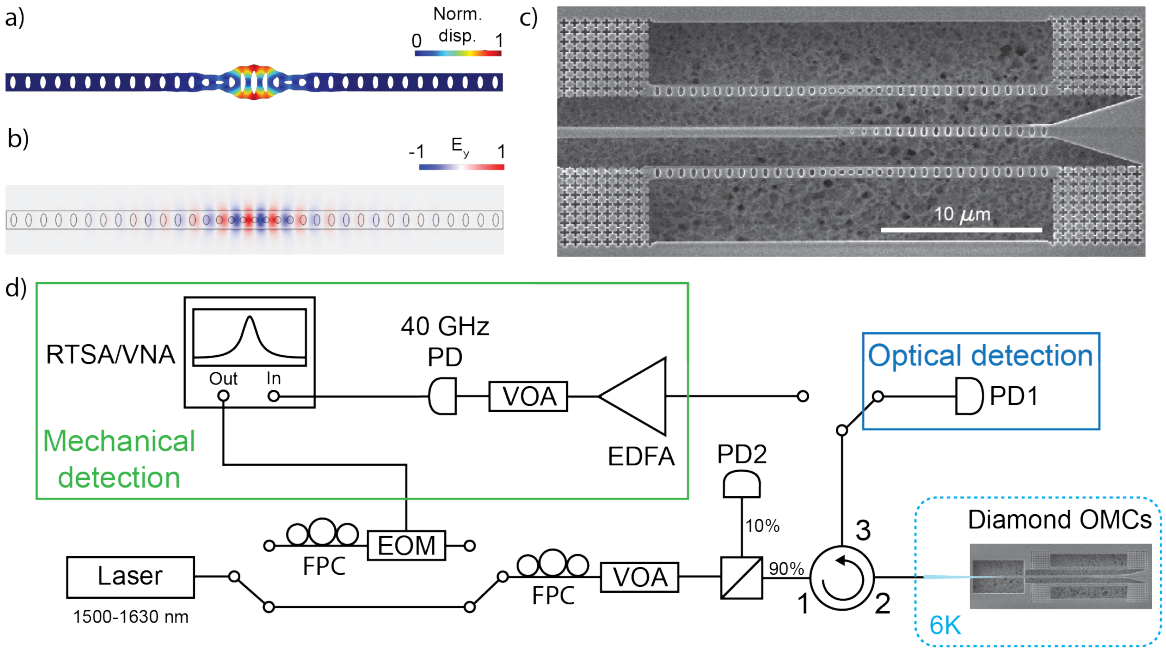

Figure 6.1: COMSOL simulations showing a) the normalized displacement of the OMC mechanical breathing mode and b) the normalized y-component of the electric field of the OMC's fundamental TE mode for device type 1. c) A scanning electron micrograph of a fabricated pair of OMCs on either side of a mirror-terminated optical waveguide. d) Overview of the OMC fiber optic measurement setup. A tunable (1500-1630 nm) laser sends light through a fiber polarization controller (FPC), variable optical attenuator (VOA), and 90/10 beam-splitter that is used to monitor the input power with a photodiode (PD2) before it is circulated into the cryostat. A tapered optical fiber couples light into and out of an on-chip waveguide. Light reflected from the device is recirculated to a switch that directs it to either optical power detection with a DC photodiode (PD1) or a mechanical detection chain in which it is amplified by an erbium-doped fiber amplifier (EDFA) before being slightly attenuated by a VOA to avoid saturating a fast 40 GHz photodiode. The output of the photodiode is detected by a combined real-time spectrum analyzer/vector network analyzer (RTSA/VNA). For measurements involving the VNA, the VNA output drives an electro-optic modulator (EOM). Light is directed through the EOM path by a pair of switches. An FPC controls the polarization of the light entering the EOM.

more significant variation in thickness across the diamond membrane than in chapter 5 (≈ 1 μm across the length of the diamond), only one row of devices was approximately the correct thickness to give measureable devices. A scanning electron micrograph of a fabricated pair of OMCs on either side of an optical waveguide is shown in figure 6.1c.

6.3 Room-temperature OMC characterization

The OMCs were then measured at room temperature in vacuum (< 100 μtorr) by circulating light from a tunable (1500-1630 nm) laser into a single-ended tapered optical fiber that is placed within the coupling region of the optical waveguide by moving the sample with piezoelectric stages. Light is then coupled into the optical waveguide with a typical single-pass efficiency $\eta_f \approx 15\%$ and either reflects off of a patterned mirror at the waveguide or evanescently couples into an OMC before recoupling into the fiber and being circulated to either a DC photodiode for measurement of the OMC optical mode, or an erbium-doped fiber amplifier (EDFA) for amplification before being measured with a fast (40 GHz) photodiode, the output of which is sent to a real-time spectrum analyzer (RTSA), for measurement of the OMC mechanical mode. An overview of the measurement setup is shown in figure 6.1d. The optical resonances of the OMCs are measured by sweeping the laser wavelength and detecting dips in the reflect optical spectrum. Figure 6.3a shows an example optical spectrum for a device of design 1 (which we call device 1_b10_l, and which we study the most in-depth), which was fit with a fano resonance function to extract a linewidth $\kappa/2\pi = 3.4$ GHz, corresponding to an optical quality factor $Q_o = 56,000$. The depth of the dip is used to back out the coupling rate κ_e between the optical waveguide and the OMC. For this device, which was very undercoupled ($\kappa_e < \kappa$, $\kappa_e/2\pi \approx 100$ MHz. The other OMC in this pair of devices (1_b10_u) had $\kappa/2\pi = 2.92$ GHz ($Q_o = 66,000$ and $\kappa_e/2/\pi = 140$ MHz while the single

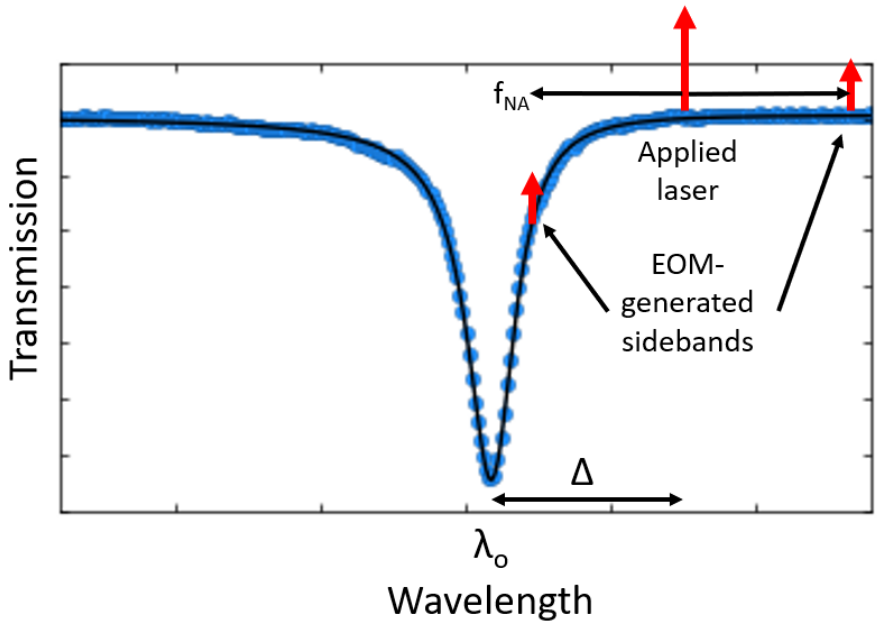

Figure 6.2: An EIT-type measurement in which an applied laser is detuned by Δ from the OMC optical frequency. A network analyzer generates sidebands on the applied laser, one of which is swept across the cavity optical resonance as the network analyzer sweeps its output frequency. The resulting beat signal (see figure 6.3) between this sideband and the applied laser is detected on the network analyzer and can be used to determine κ, κ_e, and Δ by fitting to equations 6.2-6.4.

design 2 device (device 2_b10_u) had $\kappa/2\pi = 1.466$ ($Q_o = 130,000$) GHz and $\kappa_e/2\pi = 42$ MHz.

6.4 Low temperature characterization

The mechanical properties of the OMCs were then measured by setting the applied laser frequency ω_l red-detuned (see figure 2.5) from the cavity by $\Delta = \omega_c - \omega_l = \omega_m$ and detecting the power spectrum of the reflected light for a range of input optical powers (corresponding to different numbers of intracavity photons n_c according to equation) and then fitting the Lorentzian lineshape to extract the total mechanical linewidth

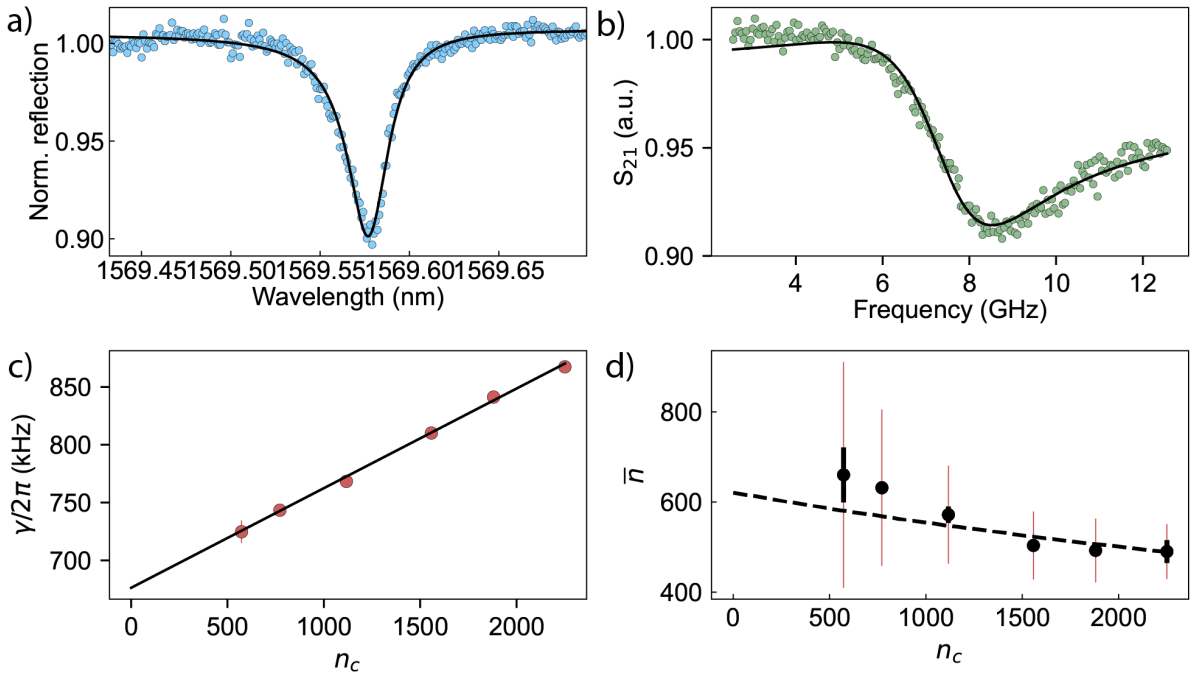

Figure 6.3: Room-temperature vacuum measurements of a diamond OMC. a) Optical resonance near 1570 nm with $\kappa/2\pi = 3.4$ GHz ($Q_o = 56{,}000$) and $\kappa_e/2\pi = 100$ MHz. b) An OMIT-type measurement used for determining laser detuning from the cavity resonance. The small response is indicative of undercoupling. c) $\gamma/2\pi$ versus n_c at room temperature. Fitting the data to equation 6.1 gives a vacuum optomechanical coupling rate $g_0/2\pi = 271$ kHz and $\gamma_i/2\pi = 676$ kHz ($Q_m = 11{,}100$). The error bars on the data correspond to the standard deviation of multiple measurements at each point. d) Inferred phonon occupancy of the mechanical mode for the spectra in c. A fit (dashed black line) to the cooling model in equation 6.7 gives a mechanical bath temperature of $n_b = 621 \pm 43$ (223 ± 15K). The red error bars are determined similarly to those in figure 6.5, while the black error bars are the standard deviation of the inferred phonon occupancy over 5 measurements.

$$\gamma = \gamma_i + \gamma_{\mathrm{OM}} = \gamma_i + \frac{4g_0^2 n_c}{\kappa} \tag{6.1}$$

where γ_i is the intrinsic mechanical linewidth and $\gamma_{\mathrm{OM}} = 4g_0^2 n_c/\kappa$ is the optomechanically-induced damping on the red sideband. The detuning wavelength for these measurements was set using an 'OMIT-type' [1] measurement defined by imprinting sidebands on the input laser using an electro-optic modulator (EOM) driven by a vector network analyzer (VNA) and detecting the transmitted amplitude of the lower-frequency sideband as it was swept across the optical cavity resonance. The result of this sideband locking measurement is fit to:

$$|S_{21}| = |\frac{y(\omega_m)}{y(\infty)}| \tag{6.2}$$

where $y(\Delta)$ is

$$y(\Delta) = -(r(0,\Delta)(\alpha + e^{i\theta}))^* r(-\omega,\Delta)e^{i\theta} + r(0,\Delta)(\alpha + e^{i\theta})(r(\omega,\Delta)e^{i\theta})^* \tag{6.3}$$

and $r(\omega, \Delta)$ is

$$r(\omega,\Delta) = 1 - \frac{\kappa_e}{i(\Delta - \omega) + \kappa/2} \tag{6.4}$$

where $\Delta = \omega_c - \omega_L$ (where ω_L is the laser frequency and ω_c is the optical cavity frequency) is the detuning from the optical cavity, and α and θ are parameters that account for the asymmetric presence of the other sideband generated by the EOM. A typical plot and

[1] OMIT = optomechanically-induced transparency. We are not measuring this here, but it uses the same measurement setup and similar fitting

fit for this measurement is shown in figure 6.3b. This fit allows us to determine the laser detuning from the optical resonance. The laser wavelength is then adjusted until the measurement gives a detuning within 50 MHz of the mechanical frequency. This process is repeated following each measurement. Figure 6.3c shows γ vs n_c for device 1_b10_l's 7.55 GHz breathing mode. Fitting the data to the formula for γ with γ_i and g_0 as fit parameters allows us to determine $g_0/2\pi = 271$ kHz and $\gamma_i/2\pi = 676$ kHz (corresponding to mechanical quality factor $Q_m = 11{,}100$). A similar set of measurements on device 2_b10_l's 6.32 GHz breathing mode gave $g_0/2\pi = 216$ kHz and $\gamma_i/2\pi = 465$ kHz (corresponding to a mechanical quality factor $Q_m = 13{,}600$). Finally, the phonon occupancy of the mode is inferred from the measured spectra, following methodology similar to that described in the following section. The result of $\overline{n}$ vs n_c at room-temperature is shown in figure 6.3d. A fit to equation 6.7 gives $\overline{n} = 621$ ($T = 223$K). The deviation from room-temperature is most likely due to large uncertainty in setting the laser to the correct detuning based on the EIT-type measurement or unaccounted loss in the detection chain.

6.5 Low temperature characterization

Next, we cool the device to 5.9K, measured with a thermometer mounted near the sample, in a closed-cycle helium cryostat (this does not correspond to the mechanical mode temperature, as we will see shortly). Figure 6.4a shows the optical spectrum of device 1_b10_l. From this spectrum we extract $\kappa/2\pi = 3.08$ GHz and $\kappa_e/2\pi = 54$ MHz. Deviations from the room temperature values ($\kappa/2\pi = 3.4$ GHz and $\kappa_e/2\pi = 100$ MHz) are attributed to sample cleanliness in the case of κ and fiber position in the case of κ_e [2]. Figure 6.4b shows a mechanical spectrum taken ≈ 100 pm (12 GHz) red of the optical

[2]The sample was cleaned between the room-temperature and low-temperature measurements, leading to a slight increase in optical quality factor. κ_e is highly dependent on both the fiber being used and

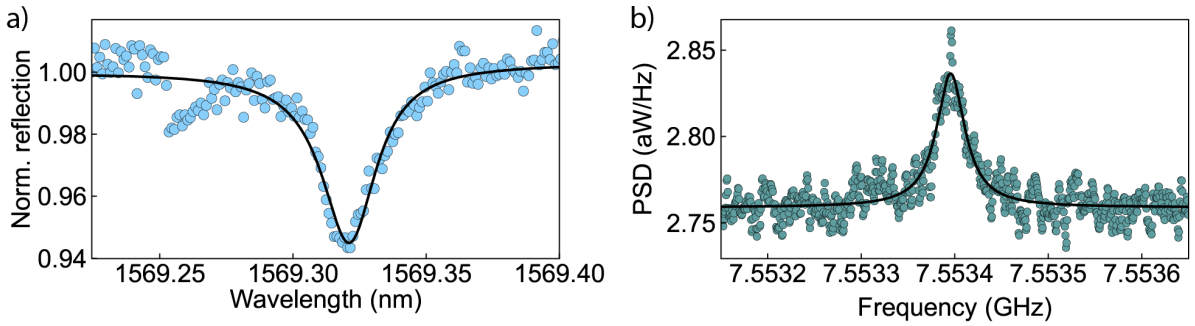

Figure 6.4: Low-temperature measurements of a diamond OMC. a) Optical resonance near 1570 nm with $\kappa/2\pi = 3.08$ GHz ($Q_o = 62{,}000$) and $\kappa_e/2\pi = 54$ MHz. b) A mechanical spectrum taken with the laser far-detuned from the optical resonance. A lorentzian fit to the spectrum gives $\gamma/2\pi = 37$ kHz (corresponding to a lower bound on Q_m of 205,000).

resonance. This large detuning is chosen to minimize optomechanical damping of the mechanical mode while still allowing for a measureable signal. A Lorentzian fit to the spectrum gives $\gamma/2\pi = 37$ kHz. Since even at this large detuning, the mode is being optomechanically damped, this measurement corresponds to placing an upper bound on the intrinsic mechanical linewidth γ_i (or, equivalently, a lower bound on Q_m).

We then look to characterize the mechanics as a function of intracavity photon number to determine the mechanical linewidth γ and phonon occupancy $\overline{n}$ as a function of n_c. In order to determine the red sideband wavelength, we employ a different technique than was used at room temperature. This was required due to drifts in the optical resonance wavelength (several pm per minute) over the course of the long time required by the sideband-locking measurements as a result of poor vacuum at low temperature[3]. This technique involves stepping the applied laser wavelength across where we expect the red sideband to be and taking a mechanical spectra at each wavelength. This gives us a plot of γ versus wavelength such as the plot shown in figure 6.5a. This is fit to the

its position along the coupling waveguide, both of which affect the standing waveguide mode, which in turn modifies the mode overlap between the waveguide mode and the OMC mode that determines κ_e.

[3]Better vacuum, a faster network analyzer, and higher κ_e (and hence a bigger signal) could all circumvent the problem of drift in future experiments.

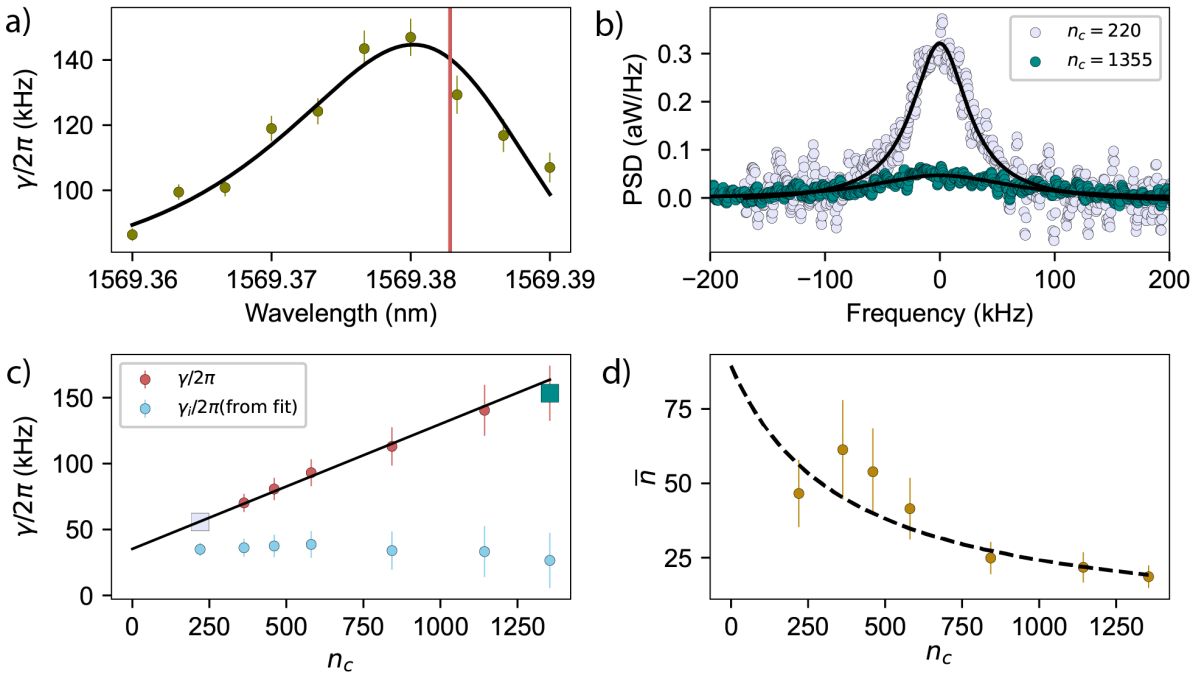

Figure 6.5: **Extracting phonon occupancy under optomechanical damping** a) Mechanical linewidth as a function of laser wavelength as the laser is stepped across the red sideband. A fit to the optomechanical model in equations 6.2-6.4 allows us to estimate the red sideband wavelength (indicated by the red line) and select the mechanical spectrum at the wavelength closest to it for further analysis. b) Power spectral density for low (light purple) and high (teal) applied power on the red sideband, showing significant broadening and cooling of the mechanical mode with higher applied power. c) $\gamma/2\pi$ versus n_c on the red sideband. The linewidths of the spectra shown in b are highlighted in their respective colors. A fit to equation 6.1 with only γ_i as a free parameter gives $\gamma_i/2\pi = 35.3 \pm 3.2$ kHz, corresponding to $Q_m = 214{,}000$. The fit values for $\gamma_i/2\pi$ are shown in blue. d) Inferred phonon occupancy of the mechanical mode for the spectra in c. A fit (dashed black line) to the cooling model in equation 6.7 gives a mechanical bath temperature of $n_b = 90$ (32.5K, compared to the fridge temperature of 5.9K measured with a thermometer mounted near the sample stage). The lowest measured occupancy is $\overline{n} = 18.6 \pm 3.8$ (6.7K).

optomechanical model for damping as a function of detuning from the optical resonance

$$\gamma = \gamma_i + n_c g_0^2 \left(\frac{-\kappa}{\kappa^2/4 + (\Delta + \omega_m)^2} + \frac{\kappa}{\kappa^2/4 + (\Delta - \omega_m)^2} \right) \tag{6.5}$$

where n_c is as in equation 2.17 and $\Delta = \omega_{\mathrm{rsb}} + \omega_m - \omega_L$ (where ω_m is the mechanical frequency and ω_{rsb} is the red sideband frequency). Only the input power P_{in}, γ_i, and ω_{rsb} are allowed to vary. The mechanical linewidth is then calculated using these fit parameters and the spectrum for the wavelength closest to the fit red sideband wavelength is selected for further analysis. Figure 6.5b shows two mechanical spectra selected this way, corresponding to high (teal) and low (light purple) input power. As expected, the spectrum for high input power exhibits significant broadening and damping relative to the spectrum for low input power. This process of determining the mechanical linewidth at the red sideband is repeated for a range of input powers, the results of which are shown in figure 6.5c, which plots the inferred mechanical linewidth (red points) and fit values for the intrinsic mechanical linewidth (blue points) versus n_c. The values of γ are fit to $\gamma = \gamma_i + 4g_0^2/\kappa$, only allowing γ_i to vary. This fit gives $\gamma_i/2\pi = 35.3 \pm 3.2$ kHz, corresponding to $Q_m = 214{,}000$, consistent with our measurement in figure 6.4b. The error bars for these points take into account the standard deviation of the fit parameters for γ_i, P_{in}, and ω_{rsb} in addition to wavelength stability of the laser, uncertainty in κ and κ_e from fits of optical spectra, and uncertainty in the fit value for g_0. Both γ and γ_i appear to decrease from their expected values at higher values of n_c. This could be due to a few different causes. Namely, κ could be increasing with n_c, such that we are overestimating the number of photons in the cavity and therefore underestimating what γ should be. However, optical spectra and OMIT-type detuning measurements taken at a wide range of input powers do not show significant variation of κ with intracavity photon

number (if anything, κ decreases slightly with higher n_c). Another possibility is that γ_i is actually smaller for the higher power measurements because they were taken first and γ_i subsequently increased due to deposition of contaminants on the device. Better vacuum conditions in the chamber in future cooldowns and retaking data in different power regimes over several days should clarify the effect.

Lastly, we aim to infer the phonon occupation of the mode $\overline{n}$ as a function of n_c in an effort to demonstrate red sideband cooling of the mechanical mode. To do so, we follow a similar method to [51] to convert the integrated power in the mechanical spectrum into a rate of photons exiting the OMC, which in turn is proportional to $\overline{n}$. The result is that

$$\overline{n} = \frac{1}{G_{tot}}\left(\frac{P_{RF}}{\hbar\omega_c}\right)\left(\frac{\kappa}{\kappa_e\gamma_{om}\eta_f\eta_0}\right) \tag{6.6}$$

$G_{tot} = G_{\text{norm}}(GA)^2$ is the total gain in the detection chain, with G_{norm} the reflected power-dependent normalized gain which mostly characterizes heterodyne and electronic gains that should not change significantly over time and GA the product of all optical gains and attenuations provided by the EDFA, attenuators, and fiber loss in the mechanical detection chain and which is measured for each data set. P_{RF} is the integrated power in the mechanical signal as measured on the real-time spectrum analyzer, ω_c is the optical cavity frequency, $\gamma_{om} = \gamma - \gamma_i$ is the optomechanical coupling, η_f is the fiber coupling efficiency, and η_0 is the total efficiency of the rest of the detection chain (capturing losses in the circulator and switch). G_{norm} is characterized by running a calibration protocol described in appendix A.1 for a range of reflected optical powers entering the mechanical detection chain, allowing calibration of the gain provided to the optomechanically generated sideband photons both through beating with the high-amplitude reflected laser tone and electronic amplification in the photodiode and RTSA. The result of a calibration run is shown in figure A.2.

The result of this conversion is shown in figure 6.5d, where inferred $\overline{n}$ is plotted versus n_c. The data points are fit to [50]

$$\overline{n} = \frac{n_b}{1+C} + \frac{C}{1+C}(\frac{\kappa}{4\omega_m})^2 \tag{6.7}$$

where n_b is the bath temperature and $C = \gamma_{OM}/\gamma_i = 4g_0^2 n_c/\kappa\gamma_i$ is the optomechanical cooperativity. Only n_b is allowed to vary and γ_i is taken from the fit in figure 6.5c. The fit to the $\overline{n}$ data gives a bath temperature of $n_b = 90$ (32.5K). The discrepancy between this temperature and the thermometer temperature is first attributed to radiative heating of the device through a window in the radiation shield surrounding the sample mount and stages within the cryostat that is used for imaging fiber placement, akin to what has been seen in silicon OMCs at similar temperatures [20, 51]. Further heating could be due to physical contact between the tapered optical fiber and the diamond, an effect that will be removed in the future through the use of lensed optical fibers that do not require physical contact with a waveguide to operate. The lowest $\overline{n}$ recorded in these measurements was 18.6, corresponding to a mode temperature of 6.7K. This corresponds to an optomechanical cooperativity $C = 4.6$, comparable to what has been demonstrated in other diamond optomechanical crystals [17] but with two orders of magnitude fewer photons.

6.6 Conclusions and future directions

The apparent insensitivity of γ_i and n_b for $n_c > 10^3$ are promising initial indications that diamond either experiences less optical absorption heating or is more robust to its effects than silicon. Further testing is required to study how $n_c = 10^4 - 10^5$ affects the

mechanical properties of diamond OMCs. Cooling into the mechanical ground state with $\overline{n} < 1$ without witnessing deviation from the theoretical cooling curve at high n_c would be a strong demonstration of diamond's superior material properties for optomechanical devices.

The main limitations to cooling further with this sample are low fiber coupling efficiency and severe undercoupling between the OMC and the waveguide, both of which limit the maximum achievable n_c. For reasonable values of $\kappa/2\pi = 3$ GHz, and critical coupling $\kappa_e/2\pi = 1.5$ GHz, cooling to $\overline{n} < 1$ with achievable P_{in} from $\overline{n} = 90$ is possible. For more liberal optical parameters $\kappa/2\pi = 1$ GHz, $\kappa_e/2\pi = 500$ MHz, in addition to a potential four-fold enhancement in η_f provided by lensed fiber coupling [51], cooling from $\overline{n} = 90$ to $\overline{n} = .25$ is theoretically possible. Lastly, measuring diamond OMCs at mK temperatures in a dilution refrigerator would be another test of diamond's insensitivity to optical absorption, since its thermal conductivity would decrease significantly such that any heating effects would be readily apparent.

Another potential direction to demonstrating diamond's lack of absorption heating would be on-resonance thermometry, in which the laser is tuned to the optical resonance and the optomechanically generated photons from the interaction between the resonant light and the OMC mechanics are detected and converted into a phonon occupation. Being resonant with the optical cavity would allow for very large $n_c > 10^5$. This discussed in more detail in the following chapter.

Chapter 7

Future directions

7.1 On-resonance thermometry

We would like to perform on-resonance thermometry for a couple of reasons: being on resonance with the optical cavity allows us to generate a large steady-state photon occupation in the cavity while simultaneously extracting the intrinsic mechanical linewidth and (hopefully) the mechanical bath temperature. Let's start with the steady-state quantum Langevin equation for the quantum component of the intra-cavity field (where the field is linearized as $\hat{a} \rightarrow \alpha_0 + \hat{a}$, with α_0 a steady-state classical amplitude).

$$\dot{\hat{a}} = 0 = -(\pm i\omega_m + \frac{\kappa}{2})\hat{a} - iG(\hat{b} + \hat{b}^\dagger) \tag{7.1}$$

where $\pm$ is for photons detuned from the cavity by $\Delta = \omega_c - \omega = \pm\omega_m$ and $G = \alpha_0 g_0$ is the enhanced optomechanical coupling rate due to the classical steady state photon occupation. Solving for $\hat{a}$ and using the input-output relation $\hat{a}_{out} = \sqrt{\kappa_e}\hat{a}$ gives the output fields of red (+) and blue (-) detuned photons a mechanical frequency from the cavity resonance

$$\hat{a}_\pm = iG(\hat{b} + \hat{b}^\dagger)\frac{\sqrt{\kappa_e}}{\mp i\omega_m - \kappa/2} \tag{7.2}$$

Now the total output field $\alpha(t)$ will be proportional to the sum of the outputs of the classical field $\alpha_{out} = \sqrt{\kappa_e}\alpha_0(t)$ where $\alpha_0(t) = \alpha_0 e^{-i\omega_c t}$ and the quantum fields $\hat{a_\pm}(t) = \hat{a}_\pm e^{-i(\omega_c \mp \omega_m)t}$. The time-dependent voltage generated at the photodiode upon detection is proportional to $|\alpha(t)|^2$

$$\begin{aligned} v(t) \propto |\alpha(t)|^2 &= \alpha_{out}[\hat{a}_+^\dagger e^{-i\omega_m t} + \hat{a}_+ e^{i\omega_m t} + \hat{a}_-^\dagger e^{i\omega_m t} + \hat{a}_- e^{-i\omega_m t}] \\ &\propto (\hat{a}_+^\dagger + \hat{a}_-)e^{-i\omega_m t} + (\hat{a}_-^\dagger + \hat{a}_+)e^{i\omega_m t} \\ &\propto \big(\frac{-i}{i\omega_m - \kappa/2} + \frac{i}{i\omega_m - \kappa/2}\big)e^{-i\omega_m t} + \big(\frac{-i}{-i\omega_m - \kappa/2} + \frac{i}{-i\omega_m - \kappa/2}\big)e^{-i\omega_m t} \\ &= 0 \end{aligned}$$

So obviously, our standard method of measuring the mechanical spectrum and extracting a phonon occupation will not work here. However, if we employ a tunable Fabry-Perot cavity on the detection chain to block pump laser tone and the blue-sideband generated photons, then we can detect the optomechanically generated photon flux from a single sideband with a superconducting nanowire single photon detector and use that to determine the number of phonons in the mechanical resonator, as was done in [92]. In this case the detected photon flux Γ will be

$$\Gamma = |a_{+,det}|^2 = \eta G^2 \frac{\kappa_e}{\kappa^2/4 + \omega_m^2}\left(\frac{x^2}{x_{zpf}^2}\right) = \eta G^2 \frac{\kappa_e}{\kappa^2/4 + \omega_m^2}\overline{n} \tag{7.3}$$

where η is the product of various inefficiencies in the detection chain (fiber and insertion losses, switches, circulators). Therefore, the phonon occupancy is

$$\overline{n} = \Gamma \frac{\kappa^2/4 + \omega_m^2}{\eta G^2 \kappa_e} \tag{7.4}$$

If $\kappa \ll \omega_m$ this can be simplified to

$$\overline{n} \approx \frac{\Gamma}{\eta \gamma_{OM}} (\frac{2\omega_m}{\kappa})^2 \tag{7.5}$$

where $\gamma_{OM} = 4G^2/\kappa$ and the optical efficiency κ_e/κ has been lumped into η.

The drawback here is that we only get information about the phonon occupancy, not the mechanical linewidth, so another method of measuring the linewidth at high optical powers will need to be developed.

7.2 Dissipative mechanical squeezing

In an optomechanical system, if one applies pump laser tones on both the red (+) and blue (-) sidebands with corresponding optomechanical couplings G_+ and G_-, with $G_+ > G_-$, then an arbitrarily large squeezing interaction is generated [93, 94], dependent only on the optical power capabilities of the pump tones and the amount of optical power the cavity can handle before either the optical or mechanical mode begin to heat. The optimal ratio of red and blue driving power for the optomechanical cooperativity of the red pump tone $C = 4G_+^2/\kappa\gamma_i$ is

$$\frac{G_-}{G_+} \approx \frac{1}{2}\sqrt{\frac{1+n_b}{C}} \tag{7.6}$$

which gives a variance of the squeezed quadrature $\hat{X}_1$

$$\frac{\langle \hat{X}_1^2 \rangle}{\langle \hat{X}_1^2 \rangle_{zpf}} = \frac{\gamma_i}{2\kappa}(1 + 2n_b) + \sqrt{\frac{1 + 2n_b}{C}} \tag{7.7}$$

For the approximate measured parameters of our OMC in chapter 6 intrinsic mechanical linewidth $\gamma_i/2\pi = 35$ kHz, optical linewidth $\kappa = 3$ GHz, cooperativity $C = 5$, and bath temperature $n_b = 90$, this would give $\langle \hat{X}_1^2 \rangle / \langle \hat{X}_1^2 \rangle_{zpf} = 6$. With improved device parameters, increased fiber coupling, and lower bath temperature in a dilution refrigerator, $\kappa = 1$ GHz, $C = 360$, and $n_b \approx 1$, we would have $\langle \hat{X}_1^2 \rangle / \langle \hat{X}_1^2 \rangle_{zpf} = 0.09$, over 10dB of squeezing. However, this depends on the increased optical power not heating the mechanical bath temperature, showing once again the importance of avoiding optical absorption heating. In fact, demonstration of this expected strong squeezing would be a de facto demonstration of lack of optical absorption heating.

The squeezed mechanical mode $\hat{\beta}$ can be measured analogously to the detection of phonon occupancy in the previous chapter, by integrating the detected mechanical spectrum and backing out the occupancy of the squeezed mechanical mode $\langle \hat{\beta}^\dagger \hat{\beta} \rangle$. This measurement gives an upper bound on the variance of the squeezed quadrature

$$\frac{\langle \hat{X}_1^2 \rangle}{\langle \hat{X}_1^2 \rangle_{zpf}} \leq e^{-2r}(1 + 2\langle \hat{\beta}^\dagger \hat{\beta} \rangle) \tag{7.8}$$

where r is the squeezing parameter $\tanh(r) = G_-/G_+$.

The squeezing can also be measured at an arbitrary angle in quadrature space by applying slightly detuned (by several mechanical linewidths), equal-power weak probe tones red of both the blue and red pump tones. Then by varying the phase ϕ of these tones relative to the pump tones and detecting the sideband spectra and using them to

back out $\langle \hat{\beta}^\dagger \hat{\beta} \rangle$, one can map out $\langle \hat{X}_\phi^2 \rangle$ as in [94, 22].

Appendix A

Experimental setup details

A.1 Gain calibration

The gain calibration protocol for the phonon occupancy measurement in chapter 6 follows the supplement of [51]. We use two lasers tuned near the optical resonance of the OMC of interest (but far enough detuned to not interact with the OMC). The two lasers are detuned from each other by approximately the mechanical frequency of the mode being calibrated for. One laser, the 'carrier' laser simulates the laser tone that we use to measure the OMC. The 'probe' laser simulates the optomechanically generated photons emitted from the cavity. Both lasers are sent through variable optical attenuators (VOAs) to control their power. The power of the probe laser is set to be constant throughout of the course of the calibration run, while the carrier laser power is varied. The two lasers are combined at a 90/10 beamsplitter with the carrier tone entering the 90 arm and then combined pathway is split at another 90/10 beamsplitter for power monitoring with a photodiode (PD2) in order to calculate the fiber coupling efficiency η_f as described in the following section. The fiber coupling efficiency is not actually important for the calibration measurement, but just for the user to maximize the range of possible reflected powers. The tones are then circulated (with calibrated efficiency η_{c12} into a tapered optical fiber that couples into the on-chip diamond waveguide, reflects off the mirror at

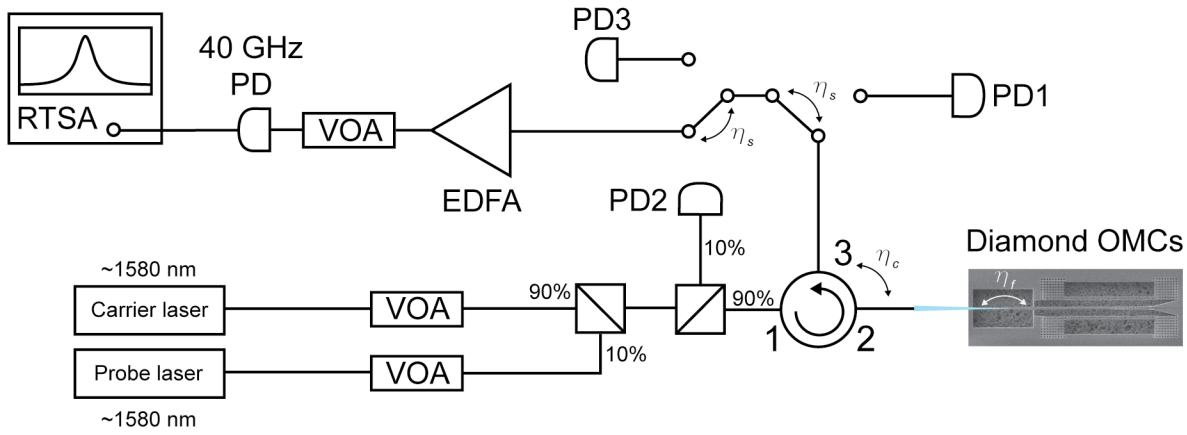

Figure A.1: The setup for calibrating measurement gain (described in detail in the text).

the end of the waveguide, re-enters the fiber, and is circulated (with efficiency η_{c23} to the detection chain. The first measurement we take is with the probe laser turned off (the VOA tuned to its maximum attenuation, $\approx$ 50dB), by sending the reflected carrier tone to photodiode PD1 through a switch with efficiency η_{s13}. The power measured here P_{PD1} is then used to define the reflected carrier power $P_{car} = P_{PD1}\eta_{s14}\eta_{s23}/\eta_{s13}$ where we have divided out η_{s13} and then multiplied the efficiency for the other configuration of the first switch and the efficiency of the configuration of the next switch that directs the light toward an EDFA. This gives us the carrier power immediately before entering the EDFA, which we typically vary from 10-200 μW to mimic values we see when taking actual measurements. We also measure the power P_{PD} incident on the fast 40 GHz photodiode, which we use a VOA to keep constant at $\approx$ 9 dBm. We use this power and the carrier power to define the gain-attentuation product GA provided by the EDFA and subsequent VOA:

$$GA = \frac{P_{PD}}{P_{car}} \tag{A.1}$$

Next, we turn off the carrier tone and measure the power of the reflected probe tone with photodiode PD3, which we then use to define the power of the probe tone $P_{probe} = P_{PD3}\eta_{s23}/\eta_{s23}$. This power is typically ≈ 20 nW. Then, with both beams on, we first use a broad measurement bandwidth spectrum analyzer to find the ≈ 7 GHz beat signal of the reflected carrier and probe tones before zooming in on that signal with a narrow (10 MHz) measurement bandwidth real-time spectrum analyzer (RTSA) (which is conveniently just a different mode of the same tool as the spectrum analyzer). The RTSA displays the raw, unaveraged beat signal, which jumps around quite rapidly due to small variations in the laser wavelengths in time. Here, there is an interruption of the automation of the rest of the protocol and the user must stop the RTSA measurement while the signal is within the 10 MHz measurement window. A typical trace is shown in figure A.2a. This process is repeated for a range of P_{car} that correspond to the anticipated range during measurements.

In processing, each probe signal is divided by the resolution bandwidth (typically 35.7 kHz) to give a spectral density of the signal, the area under which is then integrated to give a total power in the detected signal P_{RF}. The total system gain is then

$$G_{tot} = \frac{P_{RF}}{P_{probe}} \tag{A.2}$$

We then define a normalized gain

$$G_{norm} = \frac{G_{tot}}{(GA)^2} \tag{A.3}$$

which characterizes the (usually stable) electronic gain of the system. The denomi-

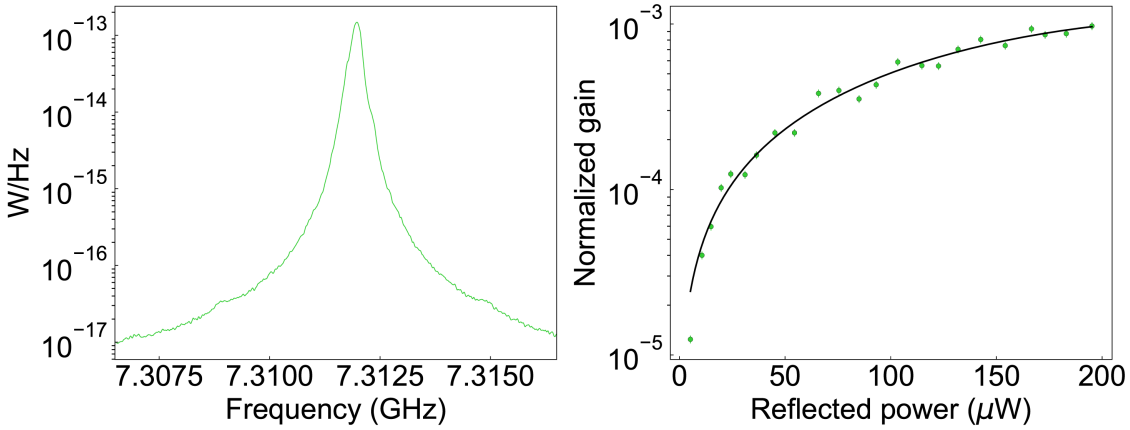

Figure A.2: a) A typical trace of the beat signal between the reflected carrier and probe tones. b) A plot of G_{norm} versus P_{car} for one set of calibration measurements. The black line indicates the fit to the third-degree polynomial.

nator is squared because, while the voltage $v(t)$ output by the fast photodiode is linear in GA, the detected electrical power at the RTSA is proportional to $|v(t)|^2$, which is proportional to $(GA)^2$ (see the supplement to [51]). The data processing takes all the calibration runs for different P_{car} and creates a plot of normalized gain versus reflected carrier power, as shown in figure A.2b. We then fit this data to a third-degree polynomial, such that the inferred normalized gain can be calculated for any P_{car} within the range measured. In subsequent measurements of $\overline{n}$, we can measure GA and P_{car} in real-time and use them to calculate the expected total gain, which we can then use in our calculation of $\overline{n}$.

A.2 Fiber coupling efficiency

If we are waveguide-coupled, then measuring the fiber coupling efficiency is straightforward. Assuming that the reflection from the end of the waveguide is near-unity then we can infer η_f by measuring the power entering and exiting the tapered fiber and noting that $\eta_f^2 = P_0/P_{out}$ where P_0 is the power before the tapered fiber and P_{out} is the power

exiting the tapered fiber. Practically speaking, the way we actually do this is by splitting off $\approx 10\%$ of our laser light with a beamsplitter before the circulator and measuring that power, then inferring P_0 by accounting for the measured asymmetry of the beamsplitter and loss in the circulator. P_{out} is measured after going back through the circulator and the optical/mechanical detection chain switch. For side-coupling, the situation is more complicated, since we don't have the luxury of a well-defined mirror at the end of the waveguide. In this case, I propose that we can use the measured optomechanical damping $\gamma_{om} = \gamma - \gamma_i = 4g_0^2 n_c/\kappa$ to calibrate n_c, which in turn can be used to calibrate the input power P_{in} to the cavity via the equation

$$n_c = \left(\frac{P_{in}}{\hbar\omega_L}\right)\frac{\kappa_e}{\Delta^2 + \frac{\kappa^2}{4}} \tag{A.4}$$

such that

$$P_{in} = \frac{\hbar\omega_L\kappa(\gamma - \gamma_i)(\Delta^2 + \frac{\kappa^2}{4})}{4g_o^2\kappa_e} \tag{A.5}$$

Therefore the fiber coupling efficiency is:

$$\eta_f = \frac{P_{in}}{P_0} = \frac{\hbar\omega_L\kappa(\gamma - \gamma_i)(\Delta^2 + \frac{\kappa^2}{4})}{4g_0^2\kappa_e P_0} \tag{A.6}$$

Bibliography

[1] G. S. MacCabe, H. Ren, J. Luo, J. D. Cohen, H. Zhou, A. Sipahigil, M. Mirhosseini, and O. Painter, "Phononic bandgap nano-acoustic cavity with ultralong phonon lifetime," *arXiv:1901.04129 [cond-mat, physics:quant-ph]*, Jan. 2019. arXiv: 1901.04129.

[2] P. Neumann, R. Kolesov, B. Naydenov, J. Beck, F. Rempp, M. Steiner, V. Jacques, G. Balasubramanian, M. L. Markham, D. J. Twitchen, S. Pezzagna, J. Meijer, J. Twamley, F. Jelezko, and J. Wrachtrup, "Quantum register based on coupled electron spins in a room-temperature solid," *Nature Physics*, vol. 6, pp. 249–253, Apr. 2010.

[3] Y. Kubo, F. R. Ong, P. Bertet, D. Vion, V. Jacques, D. Zheng, A. Dréau, J.-F. Roch, A. Auffeves, F. Jelezko, J. Wrachtrup, M. F. Barthe, P. Bergonzo, and D. Esteve, "Strong Coupling of a Spin Ensemble to a Superconducting Resonator," *Physical Review Letters*, vol. 105, p. 140502, Sept. 2010.

[4] S. D. Bennett, N. Y. Yao, J. Otterbach, P. Zoller, P. Rabl, and M. D. Lukin, "Phonon-Induced Spin-Spin Interactions in Diamond Nanostructures: Application to Spin Squeezing," *Physical Review Letters*, vol. 110, p. 156402, Apr. 2013.

[5] D. Lee, K. W. Lee, J. V. Cady, P. Ovartchaiyapong, and A. C. B. Jayich, "Topical Review: Spins and mechanics in diamond," *Journal of Optics*, vol. 19, p. 033001, Mar. 2017. Number: 3 arXiv: 1609.00418.

[6] D. Rugar, R. Budakian, H. J. Mamin, and B. W. Chui, "Single spin detection by magnetic resonance force microscopy," *Nature*, vol. 430, pp. 329–332, July 2004.

[7] A. D. O'Connell, M. Hofheinz, M. Ansmann, R. C. Bialczak, M. Lenander, E. Lucero, M. Neeley, D. Sank, H. Wang, M. Weides, J. Wenner, J. M. Martinis, and A. N. Cleland, "Quantum ground state and single-phonon control of a mechanical resonator," *Nature*, vol. 464, pp. 697–703, Apr. 2010.

[8] Y. Chu, P. Kharel, T. Yoon, L. Frunzio, P. T. Rakich, and R. J. Schoelkopf, "Creation and control of multi-phonon Fock states in a bulk acoustic-wave resonator," *Nature*, vol. 563, pp. 666–670, Nov. 2018.

[9] B. A. Moores, L. R. Sletten, J. J. Viennot, and K. W. Lehnert, "Cavity Quantum Acoustic Device in the Multimode Strong Coupling Regime," *Physical Review Letters*, vol. 120, p. 227701, May 2018.

[10] R. Manenti, A. F. Kockum, A. Patterson, T. Behrle, J. Rahamim, G. Tancredi, F. Nori, and P. J. Leek, "Circuit quantum acoustodynamics with surface acoustic waves," *Nature Communications*, vol. 8, p. 975, Dec. 2017.

[11] K. J. Satzinger, Y. P. Zhong, H.-S. Chang, G. A. Peairs, A. Bienfait, M.-H. Chou, A. Y. Cleland, C. R. Conner, É. Dumur, J. Grebel, I. Gutierrez, B. H. November, R. G. Povey, S. J. Whiteley, D. D. Awschalom, D. I. Schuster, and A. N. Cleland, "Quantum control of surface acoustic-wave phonons," *Nature*, vol. 563, pp. 661–665, Nov. 2018.

[12] F. Iikawa, A. Hernández-Mínguez, I. Aharonovich, S. Nakhaie, Y.-T. Liou, J. M. J. Lopes, and P. V. Santos, "Acoustically modulated optical emission of hexagonal boron nitride layers," *Applied Physics Letters*, vol. 114, p. 171104, Apr. 2019.

[13] S. G. Carter, A. S. Bracker, G. W. Bryant, M. Kim, C. S. Kim, M. K. Zalalutdinov, M. K. Yakes, C. Czarnocki, J. Casara, M. Scheibner, and D. Gammon, "Spin-Mechanical Coupling of an InAs Quantum Dot Embedded in a Mechanical Resonator," *Physical Review Letters*, vol. 121, p. 246801, Dec. 2018.

[14] S. J. Whiteley, G. Wolfowicz, C. P. Anderson, A. Bourassa, H. Ma, M. Ye, G. Koolstra, K. J. Satzinger, M. V. Holt, F. J. Heremans, A. N. Cleland, D. I. Schuster, G. Galli, and D. D. Awschalom, "Spin–phonon interactions in silicon carbide addressed by Gaussian acoustics," *Nature Physics*, vol. 15, pp. 490–495, May 2019.

[15] J. Bochmann, A. Vainsencher, D. D. Awschalom, and A. N. Cleland, "Nanomechanical coupling between microwave and optical photons," *Nature Physics*, vol. 9, pp. 712–716, Nov. 2013.

[16] K. C. Balram, M. I. Davanço, B. R. Ilic, J.-H. Kyhm, J. D. Song, and K. Srinivasan, "Acousto-Optic Modulation and Optoacoustic Gating in Piezo-Optomechanical Circuits," *Physical Review Applied*, vol. 7, p. 024008, Feb. 2017.

[17] M. J. Burek, J. D. Cohen, S. M. Meenehan, N. El-Sawah, C. Chia, T. Ruelle, S. Meesala, J. Rochman, H. A. Atikian, M. Markham, D. J. Twitchen, M. D. Lukin, O. Painter, and M. Lončar, "Diamond optomechanical crystals," *Optica*, vol. 3, p. 1404, Dec. 2016. Number: 12.

[18] J. V. Cady, O. Michel, K. W. Lee, R. N. Patel, C. J. Sarabalis, A. H. Safavi-Naeini, and A. C. Bleszynski Jayich, "Diamond optomechanical crystals with embedded nitrogen-vacancy centers," *Quantum Science and Technology*, vol. 4, p. 024009, Mar. 2019.

[19] P. K. Shandilya, D. P. Lake, M. J. Mitchell, D. D. Sukachev, and P. E. Barclay, "Optomechanical interface between telecom photons and spin quantum memory," *arXiv:2102.04597 [physics, physics:quant-ph]*, June 2021. arXiv: 2102.04597.

[20] J. Chan, T. P. M. Alegre, A. H. Safavi-Naeini, J. T. Hill, A. Krause, S. Gröblacher, M. Aspelmeyer, and O. Painter, "Laser cooling of a nanomechanical oscillator into its quantum ground state," *Nature*, vol. 478, pp. 89–92, Oct. 2011. Number: 7367 Publisher: Nature Publishing Group.

[21] R. Riedinger, A. Wallucks, I. Marinković, C. Löschnauer, M. Aspelmeyer, S. Hong, and S. Gröblacher, "Remote quantum entanglement between two micromechanical oscillators," *Nature*, vol. 556, pp. 473–477, Apr. 2018.

[22] C. U. Lei, A. J. Weinstein, J. Suh, E. E. Wollman, A. Kronwald, F. Marquardt, A. A. Clerk, and K. C. Schwab, "Quantum Nondemolition Measurement of a Quantum Squeezed State Beyond the 3 dB Limit," *Physical Review Letters*, vol. 117, p. 100801, Aug. 2016.

[23] P. Ovartchaiyapong, L. M. A. Pascal, B. A. Myers, P. Lauria, and A. C. Bleszynski Jayich, "High quality factor single-crystal diamond mechanical resonators," *Applied Physics Letters*, vol. 101, p. 163505, Oct. 2012.

[24] A. Barfuss, J. Teissier, E. Neu, A. Nunnenkamp, and P. Maletinsky, "Strong mechanical driving of a single electron spin," *Nature Physics*, vol. 11, pp. 820–824, Oct. 2015.

[25] B. Khanaliloo, M. Mitchell, A. C. Hryciw, and P. E. Barclay, "High- Q / V Monolithic Diamond Microdisks Fabricated with Quasi-isotropic Etching," *Nano Letters*, vol. 15, pp. 5131–5136, Aug. 2015.

[26] S. Maity, L. Shao, S. Bogdanović, S. Meesala, Y.-I. Sohn, N. Sinclair, B. Pingault, M. Chalupnik, C. Chia, L. Zheng, K. Lai, and M. Lončar, "Coherent acoustic control of a single silicon vacancy spin in diamond," *Nature Communications*, vol. 11, p. 193, Dec. 2020.

[27] D. A. Golter, T. Oo, M. Amezcua, K. A. Stewart, and H. Wang, "Optomechanical Quantum Control of a Nitrogen-Vacancy Center in Diamond," *Physical Review Letters*, vol. 116, p. 143602, Apr. 2016.

[28] E. R. MacQuarrie, T. A. Gosavi, N. R. Jungwirth, S. A. Bhave, and G. D. Fuchs, "Mechanical Spin Control of Nitrogen-Vacancy Centers in Diamond," *Physical Review Letters*, vol. 111, p. 227602, Nov. 2013.

[29] E. R. MacQuarrie, T. A. Gosavi, S. A. Bhave, and G. D. Fuchs, "Continuous dynamical decoupling of a single diamond nitrogen-vacancy center spin with a mechanical resonator," *Physical Review B*, vol. 92, p. 224419, Dec. 2015.

[30] J. Teissier, A. Barfuss, and P. Maletinsky, "Hybrid continuous dynamical decoupling: a photon-phonon doubly dressed spin," *Journal of Optics*, vol. 19, p. 044003, Apr. 2017.

[31] K. V. Kepesidis, S. D. Bennett, S. Portolan, M. D. Lukin, and P. Rabl, "Phonon Cooling and Lasing with Nitrogen-Vacancy Centers in Diamond," *Physical Review B*, vol. 88, p. 064105, Aug. 2013. Number: 6 arXiv: 1306.5915.

[32] E. R. MacQuarrie, M. Otten, S. K. Gray, and G. D. Fuchs, "Cooling a mechanical resonator with nitrogen-vacancy centres using a room temperature excited state spin–strain interaction," *Nature Communications*, vol. 8, p. 14358, Apr. 2017.

[33] M. J. Burek, D. Ramos, P. Patel, I. W. Frank, and M. Lončar, "Nanomechanical resonant structures in single-crystal diamond," *Applied Physics Letters*, vol. 103, p. 131904, Sept. 2013.

[34] P. Ovartchaiyapong, K. W. Lee, B. A. Myers, and A. C. B. Jayich, "Dynamic strain-mediated coupling of a single diamond spin to a mechanical resonator," *Nature Communications*, vol. 5, p. 4429, Dec. 2014.

[35] K. W. Lee, D. Lee, P. Ovartchaiyapong, J. Minguzzi, J. R. Maze, and A. C. Bleszynski Jayich, "Strain Coupling of a Mechanical Resonator to a Single Quantum Emitter in Diamond," *Physical Review Applied*, vol. 6, p. 034005, Sept. 2016.

[36] A. Barfuss, M. Kasperczyk, J. Kölbl, and P. Maletinsky, "Spin-stress and spin-strain coupling in diamond-based hybrid spin oscillator systems," *Physical Review B*, vol. 99, p. 174102, May 2019.

[37] Y. Tao, J. M. Boss, B. A. Moores, and C. L. Degen, "Single-crystal diamond nanomechanical resonators with quality factors exceeding one million," *Nature Communications*, vol. 5, p. 3638, May 2014.

[38] B. A. Myers, A. Das, M. C. Dartiailh, K. Ohno, D. D. Awschalom, and A. C. Bleszynski Jayich, "Probing Surface Noise with Depth-Calibrated Spins in Diamond," *Physical Review Letters*, vol. 113, p. 027602, July 2014.

[39] E. R. MacQuarrie, T. A. Gosavi, A. M. Moehle, N. R. Jungwirth, S. A. Bhave, and G. D. Fuchs, "Coherent control of a nitrogen-vacancy center spin ensemble with a diamond mechanical resonator," *Optica*, vol. 2, p. 233, Mar. 2015.

[40] H. Y. Chen, S. A. Bhave, and G. D. Fuchs, "Acoustically Driving the Single-Quantum Spin Transition of Diamond Nitrogen-Vacancy Centers," *Physical Review Applied*, vol. 13, p. 054068, May 2020.

[41] H. Y. Chen, E. R. MacQuarrie, and G. D. Fuchs, "Orbital State Manipulation of a Diamond Nitrogen-Vacancy Center Using a Mechanical Resonator," *Physical Review Letters*, vol. 120, p. 167401, Apr. 2018.

[42] H. Chen, N. F. Opondo, B. Jiang, E. R. MacQuarrie, R. S. Daveau, S. A. Bhave, and G. D. Fuchs, "Engineering Electron–Phonon Coupling of Quantum Defects to a Semiconfocal Acoustic Resonator," *Nano Letters*, vol. 19, pp. 7021–7027, Oct. 2019.

[43] D. A. Golter, T. Oo, M. Amezcua, I. Lekavicius, K. A. Stewart, and H. Wang, "Coupling a Surface Acoustic Wave to an Electron Spin in Diamond via a Dark State," *Physical Review X*, vol. 6, p. 041060, Dec. 2016.

[44] M. J. A. Schuetz, E. M. Kessler, G. Giedke, L. M. K. Vandersypen, M. D. Lukin, and J. I. Cirac, "Universal Quantum Transducers Based on Surface Acoustic Waves," p. 30, 2015.

[45] M. Mitchell, B. Khanaliloo, D. P. Lake, T. Masuda, J. P. Hadden, and P. E. Barclay, "Single-crystal diamond low-dissipation cavity optomechanics," *Optica*, vol. 3, p. 963, Sept. 2016.

[46] M. Mitchell, D. P. Lake, and P. E. Barclay, "Realizing Q > 300 000 in diamond microdisks for optomechanics via etch optimization," *APL Photonics*, vol. 4, p. 016101, Jan. 2019.

[47] A. H. Safavi-Naeini and O. Painter, "Optomechanical Crystal Devices," in *Cavity Optomechanics* (M. Aspelmeyer, T. J. Kippenberg, and F. Marquardt, eds.), pp. 195–231, Berlin, Heidelberg: Springer Berlin Heidelberg, 2014.

[48] J. D. Cohen, "Fiber-optic integration and efficient detection schemes for optomechanical resonators," p. 134.

[49] A. H. Safavi-Naeini, "Quantum Optomechanics with Silicon Nanostructures," p. 191.

[50] J. Chan, "Laser cooling of an optomechanical crystal resonator to its quantum ground state of motion," p. 140.

[51] R. N. Patel, Z. Wang, W. Jiang, C. J. Sarabalis, J. T. Hill, and A. H. Safavi-Naeini, "Single-Mode Phononic Wire," *Physical Review Letters*, vol. 121, p. 040501, July 2018.

[52] M.-A. Lemonde, S. Meesala, A. Sipahigil, M. J. A. Schuetz, M. D. Lukin, M. Loncar, and P. Rabl, "Phonon Networks with Silicon-Vacancy Centers in Diamond Waveguides," *Physical Review Letters*, vol. 120, p. 213603, May 2018.

[53] M. W. Doherty, N. B. Manson, P. Delaney, F. Jelezko, J. Wrachtrup, and L. C. Hollenberg, "The nitrogen-vacancy colour centre in diamond," *Physics Reports*, vol. 528, pp. 1–45, July 2013.

[54] K. W. Lee, "Coherent dynamics of a hybrid quantum spin-mechanical oscillator system," 2017.

[55] B. A. Myers, "dissertation_090716_bryanmyers."

[56] B. A. Myers, A. Ariyaratne, and A. C. B. Jayich, "Double-Quantum Spin-Relaxation Limits to Coherence of Near-Surface Nitrogen-Vacancy Centers," *Physical Review Letters*, vol. 118, p. 197201, May 2017.

[57] N. Bar-Gill, L. Pham, A. Jarmola, D. Budker, and R. Walsworth, "Solid-state electronic spin coherence time approaching one second," *Nature Communications*, vol. 4, p. 1743, June 2013.

[58] A. Sipahigil, K. D. Jahnke, L. J. Rogers, T. Teraji, J. Isoya, A. S. Zibrov, F. Jelezko, and M. D. Lukin, "Indistinguishable Photons from Separated Silicon-Vacancy Centers in Diamond," *Physical Review Letters*, vol. 113, p. 113602, Sept. 2014.

[59] S. Meesala, Y.-I. Sohn, B. Pingault, L. Shao, H. A. Atikian, J. Holzgrafe, M. Gündoğan, C. Stavrakas, A. Sipahigil, C. Chia, R. Evans, M. J. Burek, M. Zhang, L. Wu, J. L. Pacheco, J. Abraham, E. Bielejec, M. D. Lukin, M. Atatüre, and M. Lončar, "Strain engineering of the silicon-vacancy center in diamond," *Physical Review B*, vol. 97, p. 205444, May 2018. Number: 20.

[60] C. Hepp, T. Müller, V. Waselowski, J. N. Becker, B. Pingault, H. Sternschulte, D. Steinmüller-Nethl, A. Gali, J. R. Maze, M. Atatüre, and C. Becher, "Electronic Structure of the Silicon Vacancy Color Center in Diamond," *Physical Review Letters*, vol. 112, p. 036405, Jan. 2014. Number: 3.

[61] D. D. Sukachev, A. Sipahigil, C. T. Nguyen, M. K. Bhaskar, R. E. Evans, F. Jelezko, and M. D. Lukin, "Silicon-Vacancy Spin Qubit in Diamond: A Quantum Memory Exceeding 10 ms with Single-Shot State Readout," *Physical Review Letters*, vol. 119, p. 223602, Nov. 2017. Number: 22 arXiv: 1708.08852.

[62] J. N. Becker, B. Pingault, D. Groß, M. Gündoğan, N. Kukharchyk, M. Markham, A. Edmonds, M. Atatüre, P. Bushev, and C. Becher, "All-Optical Control of the Silicon-Vacancy Spin in Diamond at Millikelvin Temperatures," *Physical Review Letters*, vol. 120, p. 053603, Jan. 2018.

[63] M. Aspelmeyer, T. J. Kippenberg, and F. Marquardt, "Cavity optomechanics," *Reviews of Modern Physics*, vol. 86, pp. 1391–1452, Dec. 2014. Number: 4 Publisher: American Physical Society.

[64] D. Walls and G. J. Milburn, "Input–Output Formulation of Optical Cavities," in *Quantum Optics* (D. Walls and G. J. Milburn, eds.), pp. 127–141, Berlin, Heidelberg: Springer, 2008.

[65] A. Akhiezer, "On the absorption of sound in solids," *Journal of Physics (Moscow)*, vol. 1, no. 1, 1939.

[66] L. Landau and G. Rumer, "Absorption of sound in solids," *Phys. Z Sowjetunion*, vol. 11, 1937.

[67] R. Lifshitz and M. L. Roukes, "Thermoelastic damping in micro- and nanomechanical systems," *Physical Review B*, vol. 61, pp. 5600–5609, Feb. 2000.

[68] A. Sikora, H. Ftouni, J. Richard, C. Hébert, D. Eon, F. Omnès, and O. Bourgeois, "Highly sensitive thermal conductivity measurements of suspended membranes (SiN and diamond) using a 3w-Volklein method," *Review of Scientific Instruments*, vol. 83, p. 054902, May 2012. Number: 5 arXiv: 1201.4034.

[69] S. G. Johnson, M. Ibanescu, M. A. Skorobogatiy, O. Weisberg, J. D. Joannopoulos, and Y. Fink, "Perturbation theory for Maxwell's equations with shifting material boundaries," *Physical Review E*, vol. 65, p. 066611, June 2002.

[70] A. R. Lang, "The strain-optical constants of diamond: A brief history of measurements," *Diamond and Related Materials*, vol. 18, pp. 1–5, Jan. 2009.

[71] G. Davies and M. F. Hammer, "Optical studies of the 1.945 eV vibronic band in diamond," *Proc. R. Soc. Lond. A*, vol. A., no. 348, pp. 285–289, 1976.

[72] R. N. Patel, T. Schröder, N. Wan, L. Li, S. L. Mouradian, E. H. Chen, and D. R. Englund, "Efficient photon coupling from a diamond nitrogen vacancy center by integration with silica fiber," *Light: Science & Applications*, vol. 5, pp. e16032–e16032, Feb. 2016.

[73] H. A. Atikian, P. Latawiec, M. J. Burek, Y.-I. Sohn, S. Meesala, N. Gravel, A. B. Kouki, and M. Lončar, "Freestanding nanostructures via reactive ion beam angled etching," *APL Photonics*, vol. 2, p. 051301, May 2017.

[74] M. J. Burek, N. P. de Leon, B. J. Shields, B. J. M. Hausmann, Y. Chu, Q. Quan, A. S. Zibrov, H. Park, M. D. Lukin, and M. Lončar, "Free-Standing Mechanical and Photonic Nanostructures in Single-Crystal Diamond," *Nano Letters*, vol. 12, pp. 6084–6089, Dec. 2012.

[75] C. Uzan-Saguy, C. Cytermann, R. Brener, V. Richter, M. Shaanan, and R. Kalish, "Damage threshold for ion-beam induced graphitization of diamond," *Applied Physics Letters*, vol. 67, pp. 1194–1196, Aug. 1995.

[76] J. C. Lee, D. O. Bracher, S. Cui, K. Ohno, C. A. McLellan, X. Zhang, P. Andrich, B. Alemán, K. J. Russell, A. P. Magyar, I. Aharonovich, A. Bleszynski Jayich, D. Awschalom, and E. L. Hu, "Deterministic coupling of delta-doped nitrogen vacancy centers to a nanobeam photonic crystal cavity," *Applied Physics Letters*, vol. 105, p. 261101, Dec. 2014.

[77] C. F. Wang, E. L. Hu, J. Yang, and J. E. Butler, "Fabrication of suspended single crystal diamond devices by electrochemical etch," *Journal of Vacuum Science & Technology B: Microelectronics and Nanometer Structures*, vol. 25, no. 3, p. 730, 2007.

[78] B. A. Fairchild, P. Olivero, S. Rubanov, A. D. Greentree, F. Waldermann, R. A. Taylor, I. Walmsley, J. M. Smith, S. Huntington, B. C. Gibson, D. N. Jamieson, and S. Prawer, "Fabrication of Ultrathin Single-Crystal Diamond Membranes," *Advanced Materials*, vol. 20, pp. 4793–4798, Dec. 2008.

[79] N. R. Parikh, J. D. Hunn, E. McGucken, M. L. Swanson, C. W. White, R. A. Rudder, D. P. Malta, J. B. Posthill, and R. J. Markunas, "Single-crystal diamond plate liftoff achieved by ion implantation and subsequent annealing," *Applied Physics Letters*, vol. 61, pp. 3124–3126, Dec. 1992.

[80] V. S. Drumm, A. D. C. Alves, B. A. Fairchild, K. Ganesan, J. C. McCallum, D. N. Jamieson, S. Prawer, S. Rubanov, R. Kalish, and L. C. Feldman, "Surface damage on diamond membranes fabricated by ion implantation and lift-off," *Applied Physics Letters*, vol. 98, p. 231904, June 2011.

[81] A. P. Magyar, J. C. Lee, A. M. Limarga, I. Aharonovich, F. Rol, D. R. Clarke, M. Huang, and E. L. Hu, "Fabrication of thin, luminescent, single-crystal diamond membranes," *Applied Physics Letters*, vol. 99, p. 081913, Aug. 2011.

[82] A. Stacey, V. S. Drumm, B. A. Fairchild, K. Ganesan, S. Rubanov, R. Kalish, B. C. C. Cowie, S. Prawer, and A. Hoffman, "Improved diamond surfaces following lift-off and plasma treatments as observed by x-ray absorption spectroscopy," *Applied Physics Letters*, vol. 98, p. 181907, May 2011.

[83] M. S. J. Barson, P. Peddibhotla, P. Ovartchaiyapong, K. Ganesan, R. L. Taylor, M. Gebert, Z. Mielens, B. Koslowski, D. A. Simpson, L. P. McGuinness, J. McCallum, S. Prawer, S. Onoda, T. Ohshima, A. C. Bleszynski Jayich, F. Jelezko, N. B. Manson, and M. W. Doherty, "Nanomechanical Sensing Using Spins in Diamond," *Nano Letters*, vol. 17, pp. 1496–1503, Mar. 2017.

[84] S. Gröblacher, J. T. Hill, A. H. Safavi-Naeini, J. Chan, and O. Painter, "Highly efficient coupling from an optical fiber to a nanoscale silicon optomechanical cavity," *Applied Physics Letters*, vol. 103, p. 181104, Oct. 2013.

[85] L. I. Childress, "Coherent manipulation of single quantum systems in the solid state," p. 188.

[86] C. A. McLellan, B. A. Myers, S. Kraemer, K. Ohno, D. D. Awschalom, and A. C. Bleszynski Jayich, "Patterned Formation of Highly Coherent Nitrogen-Vacancy Centers Using a Focused Electron Irradiation Technique," *Nano Letters*, vol. 16, pp. 2450–2454, Apr. 2016.

[87] Y. Chu, N. de Leon, B. Shields, B. Hausmann, R. Evans, E. Togan, M. J. Burek, M. Markham, A. Stacey, A. Zibrov, A. Yacoby, D. Twitchen, M. Loncar, H. Park, P. Maletinsky, and M. Lukin, "Coherent Optical Transitions in Implanted Nitrogen Vacancy Centers," *Nano Letters*, vol. 14, pp. 1982–1986, Apr. 2014.

[88] A. Albrecht, A. Retzker, F. Jelezko, and M. B. Plenio, "Coupling of nitrogen vacancy centres in nanodiamonds by means of phonons," *New Journal of Physics*, vol. 15, p. 083014, Aug. 2013.

[89] M. Borselli, T. J. Johnson, C. P. Michael, M. D. Henry, and O. Painter, "Surface Encapsulation for Low-Loss Silicon Photonics," *Applied Physics Letters*, vol. 91, p. 131117, Sept. 2007. Number: 13 arXiv: 0707.0415.

[90] S. M. Meenehan, J. D. Cohen, G. S. MacCabe, F. Marsili, M. D. Shaw, and O. Painter, "Pulsed Excitation Dynamics of an Optomechanical Crystal Resonator near Its Quantum Ground State of Motion," *Physical Review X*, vol. 5, p. 041002, Oct. 2015. Number: 4.

[91] S. M. Meenehan, "Cavity Optomechanics at Millikelvin Temperatures," p. 148.

[92] H. Ren, M. H. Matheny, G. S. MacCabe, H. Pfeifer, M. Mirhosseini, and O. Painter, "Two-Dimensional Optomechanical Crystal Cavity with High Quantum Cooperativity," p. 21.

[93] A. Kronwald, F. Marquardt, and A. A. Clerk, "Arbitrarily large steady-state bosonic squeezing via dissipation," *Physical Review A*, vol. 88, p. 063833, Dec. 2013.

[94] E. E. Wollman, C. U. Lei, A. J. Weinstein, J. Suh, A. Kronwald, F. Marquardt, A. A. Clerk, and K. C. Schwab, "Quantum squeezing of motion in a mechanical resonator," *Science*, vol. 349, pp. 952–955, Aug. 2015. arXiv: 1507.01662.